Mechanism-based Constitutive Modeling of $L1_2$ Single-crystal Plasticity

by

Yuan Yin

Master of Science in Mechanical Engineering,
Massachusetts Institute of Technology, Cambridge, MA (2003)

Submitted to the Department of Mechanical Engineering
in partial fulfillment of the requirements for the degree of

Doctor of Philosophy in Mechanical Engineering

at the

MASSACHUSETTS INSTITUTE OF TECHNOLOGY

February 2006

Author ....
Department of Mechanical Engineering
November 10, 2005

Certified by ....
David M. Parks
Professor of Mechanical Engineering
Thesis Supervisor

Accepted by ....
Lallit Anand
Chairman, Department Committee on Graduate Students

Mechanism-based Constitutive Modeling of $L1_2$ Single-crystal Plasticity

by

Yuan Yin

Submitted to the Department of Mechanical Engineering
on November 10, 2005, in partial fulfillment of the
requirements for the degree of
Doctor of Philosophy in Mechanical Engineering

Abstract

Ni_3Al, an $L1_2$ structure intermetallic crystal, is the basic composition of the γ' precipitates in nickel-based superalloys and is a major strengthening mechanism contributing to the superalloys' outstanding high-temperature mechanical properties. Many $L1_2$-structure crystals present unusual macroscopic mechanical properties, including the anomalous temperature-dependence of yield strength and strain hardening rate. To date, extensive research has been carried out to reveal the underlying mechanisms. However, none of the resulting models has satisfactorily quantified the macroscopic behavior based on microscopic phenomena. Mechanism-based constitutive modeling and simulation provide an effective method in this respect, assisting in the understanding and development of current existing models, and potentially providing a convenient path for engineering applications. In light of recent theoretical developments and experimental evidence, a single-crystal continuum plasticity model for the $L1_2$-structure compound Ni_3Al is developed. Both the superkink-bypassing mechanism and the self-unlocking mechanism have been modified and combined to describe the unlocking of sessile screw dislocations and the deformation-induced evolution of dislocation "states" in the yield anomaly region. The proposed model has been implemented within a finite-element framework to investigate the mechanical properties observed in constant strain-rate uni-axial tension/compression tests. Results of numerical simulations successfully capture major features of the mechanical behavior of Ni_3Al-based single crystals, including the anomalous temperature-dependence and the strong orientation-dependence of yield strength and hardening rate, the yielding properties of tension-compression asymmetry and the strain-rate insensitivity of yield strength and strain hardening rate. Diffusional processes corresponding to the uni-axial deformation of [001]-orientation at very high temperatures, and the property of yield strength reversibility presented by the Cottrell-Stokes experiments are also discussed.

Thesis Supervisor: David M. Parks
Title: Professor of Mechanical Engineering

Acknowledgments

I begin by thanking my thesis supervisor, Professor David Parks, for his support over the last five years. He gave me the opportunity to work on an interesting and challenging problem and to learn the abilities which will help me well in my profession.

It has been a great pleasure and privilege to share an office with a very interesting group of people who have been great friends as well as good sources of discussion: Adam Mulliken, Cheng Su, Hang Qi, Jin Yi, Mats Danielsson, Mike King, Nicoli Ames, Nuo Sheng, Rajdeep Sharma, Scott Therkelsen, Theodora Tzianetopoulou, Vaibhaw Vishal and Yujie Wei.

Thanks to Mr. Raymond Hardin, who was always very encouraging and helped with all information necessary to make things run smoothly.

Finally, many, many thanks to my family. Special mention must be made of my mom, Shu Liu, who was always there supporting me and encouraging me, even in a very bad health condition herself. My husband, Qin, thanks for your understanding and being so supportive to me.

Contents

List of Figures

List of Tables

Chapter 1

Introduction

1.1 Background

Nickel-based superalloys are of great interest because of their excellent mechanical properties of high-temperature strength and creep resistance. Based on these particular mechanical properties, they are subjected to very severe operating conditions in both commercial and military applications, especially in gas turbine engines. The yield strengths of nickel-based superalloys are also fundamental design parameters in the manufacture of aerospace components.

Due to the complex microstructure of nickel-based superalloys, their outstanding high-temperature strength is derived from a combination of several principal mechanisms. Among them, strengthening by γ' precipitates is one of the most important.

The basic composition of the γ' precipitates is Ni_3Al, an $L1_2$ structure crystal. $L1_2$ is a derivative configuration of the fcc crystal structure (Figure 1-1 (a)), and is typical for compounds with an AB_3 composition. In the unit cell of an $L1_2$ crystal, the minority (A) atoms occupy the corner sites, and the majority (B) atoms occupy the face-center sites (Figure 1-1(b)). As a result, the lattice translation vector in $L1_2$ compounds is $< 110 >$, as opposed to $1/2 < 110 >$ in fcc crystals.

Extensive research has been carried out since the first observation of the anomalous temperature-dependence of hardness in Ni_3Al in 1957 [2] (Figure 1-2(a)). In the early stages, most work focused on yield-related mechanical properties, while in the past

10 years, more and more attention has been placed on strain hardening. Since Ni_3Al is ordered up to its melting temperature, the yield anomaly can not be explained by an order-disorder transition, as in β-brass. The common understanding is that their macroscopic mechanical properties are dominated by the behavior of dislocations, and a considerable number of models and theories have been put forward based on certain observations and various hypotheses. However, due to the extreme complexity of the structures, mechanisms and their kinetics, none of the existing models can satisfactorily explain all of the major mechanical properties of the $L1_2$ crystals. Moreover, most of the existing models are not completely quantitative, and lack verifications based on numerical simulations. Mechanism-based constitutive modeling and simulation can be very useful in this respect, assisting the understanding of current existing models and providing a convenient method for engineering application, (e.g., assisting the development of new alloys and guiding the implementation of existing alloys).

This PhD research focused on developing a single-crystal constitutive model for the $L1_2$ structure crystals. Following a broad literature study, the proposed constitutive model was developed based on recent theoretical developments in dislocation mechanics and experimental evidence, and was implemented into a numerical solver through a user-material interface to a commercially-available FEM package. The simulation results successfully captured the principal mechanical behaviors of $L1_2$ crystals, especially the temperature-dependence, the orientation-dependence and the small strain-rate sensitivity of yield strength and strain hardening rate.

1.2 Description of the Material Studied

1.2.1 Terminology

Certain specific terms are commonly used to describe basic micro-features in the study of $L1_2$ structure compounds, and these features are closely related to the macroscopic mechanical properties. Therefore, in order to assure a good understanding of $L1_2$ structure compounds, it is appropriate to give brief descriptions of these terms first.

1. **Superlattice Dislocations and Antiphase Boundaries (APBs) :** The total dislocation Burgers vector in the $L1_2$ crystal structure is $< 1\bar{1}0 >$, twice the value in fcc materials. Dislocations having such long Burgers vectors are commonly termed superdislocations. Superdislocations often dissociate into two partial dislocations, each having a Burgers vector of $b = \frac{1}{2} < 1\bar{1}0 >$, which are usually termed "superpartials". When the superpartials separate, a planar fault termed an "Antiphase boundary" (APB) is created on their plane of spreading (Figure 1-3). An APB ribbon can exist on both octahedral planes and cube planes, and the average dissociation width is found to be 75 $\mathring{A}$ ($\sim 30b$) [12]. APB energy is found to be lower on cube planes than on octahedral planes, and is composition-dependent.

2. **Complex Stacking Faults (CSF):** The complexity of the dislocations structures in the $L1_2$ ordered intermetallic compounds goes beyond that of the simple splitting into two superpartials. Superpartials generally further dissociate and split into two Shockley partials, bounding a Complex Stacking Fault (CSF) inside (Figure 1-3 (b)). The Shockley partials only dissociate on octahedral planes, and the core extension is found to be very narrow (around $3b$ in Ni_3Al [34]) under the observation with high-resolution electron microscopy (HREM). CSF energy is also found to be very composition-dependent. A detailed summary of the existing measurements of APB energy and the CSF energy has been listed in Table 3 of the review paper by Veyssiere [34].

   The dissociation of $< 110 >$ screws into two superpartials, which further dissociate into Shockley partials, is widely observed and considered to be closely related to the yield anomaly in $L1_2$ single crystals. Theoretically, $\{111\} < 110 >$ screws can dissociate in another mode, involving splitting into two super-lattice Shockley partials, with the Burgers vector of $\frac{1}{3} < 112 >$. It has been suggested that the normal temperature-dependence of some $L1_2$ structure crystals (such as Pt_3Al) is related to this dissociation mode. But there is no direct experimental evidence so far to support this idea [65].

3. **Kear-Wilsdorf Lock :** $\{111\} < 1\bar{1}0 >$ screws in $L1_2$ crystals can cross-slip onto the $\{001\}$ cube planes, driven by a drop of APB energy and the torque forces due to large elastic anisotropy. A non-planar Kear-Wilsdorf lock (K-W lock) [1] configuration is generated if the leading screw superpartials cross-slip onto a cube plane for some distance, cross-slip back onto a parallel octahedral plane, and move forwards until the trailing superpartials meet the cross-slipped cube plane and can not advance on the octahedral plane any more (Figure 1-4(b)). This locked configuration is termed an "incomplete K-W lock" (IKW) if only part of the APB has been transferred onto the cube plane; otherwise, it is a "complete K-W lock" (CKW).

4. **Superkinks:** Due to the cross-slip of screws and the formation of K-W locks, the mobility of screw dislocations is much lower than the mobility of edge-charactered dislocations. Thus, locked screws are observed to be the dominant micro-features of $L1_2$ compounds deformed in the anomalous yield region. These locked screws are generally not straight, but contain many edge-oriented segments. These edge-oriented segments are usually termed "superkinks" (Figure 1-5).

1.2.2 Macro-mechanical Properties of $L1_2$ Single Crystals

The first demonstration of the unusual mechanical behavior of alloys having the $L1_2$ ordered structure was provided by Westbrook [2]. He showed that there was a peak in the hardness vs. temperature plot of Ni_3Al (Figure 1-2(a)). A later study [3] confirmed from tensile tests that the 0.01% offset yield strength of polycrystalline Ni_3Al also increased with increasing temperature, as shown in Figure 1-2(b). Since then, extensive experimental work has been carried out, and many mechanical features about the $L1_2$ structure crystal have been summarized. However, since binary $L1_2$ single crystals are difficult to grow, it should be kept in mind that most of the experimental properties were measured using crystals with different ternary compositions. Here, only the most general mechanical characteristics related to $L1_2$ single crystals are summarized and listed:

1. The yield strength increases with increasing temperature, both in tension and compression, until a peak yield temperature ($T_{p,\sigma}$) is reached [4]. Above the peak temperature, the strength drops off significantly (Figure 1-6). The temperature of peak yield strength ($T_{p,\sigma}$) depends on crystal composition and the loading orientation.

2. The Schmid law is often violated: crystal orientations with the same Schmid factor (e.g., $< 001 >$ and $< 011 >$) have different yield strengths under uniaxial states of stress. Even for the same orientation, yield strength often differs in tension and compression. Orientations close to the [001] corner of the unit crystal triangle show a higher strength in tension than in compression, while for orientations on the other side of the crystal triangle, compression strength is higher than the tensile strength (Figure 1-6).

3. The yield strength anomaly disappears in the micro-strain range (with the offset strain less than 10^{-5}) Figure(1-7) [5].

4. Work hardening rate (WHR) also presents anomalous properties. Generally, WHR represents the slope of the stress-strain curve and is marked as θ or h for polycrystals and single crystals, respectively ($\theta = \frac{d\sigma}{d\epsilon}$, and $h = \frac{d\tau}{d\gamma}$, in which σ, and ϵ represent the uniaxial true stress and plastic strain, and τ and γ represent the resolved shear stress and strain of a slip system). WHR is reported to be very large (up to 40% of the shear modulus) and orientation-dependent (Figure 1-8 (b)). It anomalously increases with temperature up to a peak strain hardening temperature $T_{p,h}$, and $T_{p,h}$ is usually smaller than the peak temperature of yield strength, $T_{p,\sigma}$, as shown in Figure 1-8 (a).

5. The strain-rate dependence of the yield strength is found to be positive but very small below $T_{p,\sigma}$, in both strain-rate jump and constant strain-rate tests (Figure 1-9 (a), (b)). Commonly, the change in the yield strength is less than 1% corresponding to a strain-rate change by a factor of ten [5]. However, above

$T_{p,\sigma}$, a strong positive strain-rate sensitivity is observed [4] (Figure 1-9 (b)). In the anomalous yield region, the strain hardening rate is also found to be rate-insensitive (Figure 1-9 (a)).

6. Yield strength of $L1_2$ single crystals is found to be largely reversible in so-called Cottrell-Stokes type experiments. That is, the yield strength of a sample, which has previously been deformed at a higher temperature, when subsequently further deformed at a lower temperature, is similar to the lower yield strength of a virgin sample deformed at the same lower temperature (Figure 1-10). If the prestraining temperature is lower than the deforming temperature [6], the yield strength of the prestrained sample is much lower than that of a virgin sample deformed at the same high temperature.

1.2.3 Microscopic Observations in $L1_2$ Compounds

Since it is commonly believed that the macro-mechanical behaviors of $L1_2$ structure crystals reflect the underlying dislocation dynamics, many TEM observations have been carried out to reveal the governing micro-mechanisms. We review below the most representative microscopic observations in $L1_2$ compounds, which served as the physical bases for most of the prevailing models.

1. In the anomalous yield range, octahedral slip systems dominate. Above $T_{p,\sigma}$, predominant cube slip comes into control [4]. This is supported by the observation of the change of the dominant slip traces (Figure 1-11) and TEM observations of the dislocation substructures.

2. Most of the dislocations observed in the anomalous region are long $< 101 >$ screws [7, 8] (Figure 1-12), which indicates that screw dislocations are much less mobile than the non-screws, as confirmed later by several *in-situ* deformation experiments [9, 10]. The sessile screw superdislocation segments are mostly locked in the Kear-Wilsdorf configuration.

3. The dominating long screws are not straight but contain many steps (superkinks),

which have been observed *post-mortem* (Figure 1-5). For deformation, at a given temperature, the number distribution of superkinks exhibits an exponential decrease with superkink height, l, $N = N_0 \exp(-l/l_0)$ (Figure 1-13). The "mean" height of superkinks, which is actually l_0, decreases with increasing deformation temperature, from $l_0 \sim 18 - 20$ nm at 300 K to 10-12nm at 673 K in Ni_3Ga, as reported by Couret [11]. At room temperature, a large number of Ni_3Ga superkinks with the height equal to the APB width have also been observed.

4. Jerky movement of screw dislocations was reported in room temperature *in situ* experiments (Figure 1-14). Long screw dislocations on the octahedral planes were observed to stay in one position for a while (several seconds) and then suddenly jump to another position [12]. The jumping distance varies, and sometimes it scales with the APB dissociation width; such a process is usually referred to as an "APB jump".

5. Above the temperature of maximum yield strength, $T_{p,\sigma}$, the dislocation substructure on the cube plane shows both screw and edge dislocations with nearly equal densities (Figure 1-15), implying comparable mobility for screws and edges. Unlike octahedral slip, cube slip is confirmed to be planar, without cross-slips.

1.3 Outline of the Thesis

This PhD research aims to develop a mechanism-based constitutive model for $L1_2$ single crystal plasticity. Background and motivations for the research are given in Chapter 1. Major mechanical properties and microscopic observations are also presented.

Chapter 2 gives a detailed literature study for the most representative models and theories, along with necessary discussions. Based on these pre-existing models, the proposed model is expounded in Chapter 3.

The framework of continuum crystal plasticity is reviewed first in Chapter 4, followed by the implementation of the proposed model.

In Chapter 5, the results of simulations will be reviewed and discussed, and the summary and future inquiry will be proposed in Chapter 6.

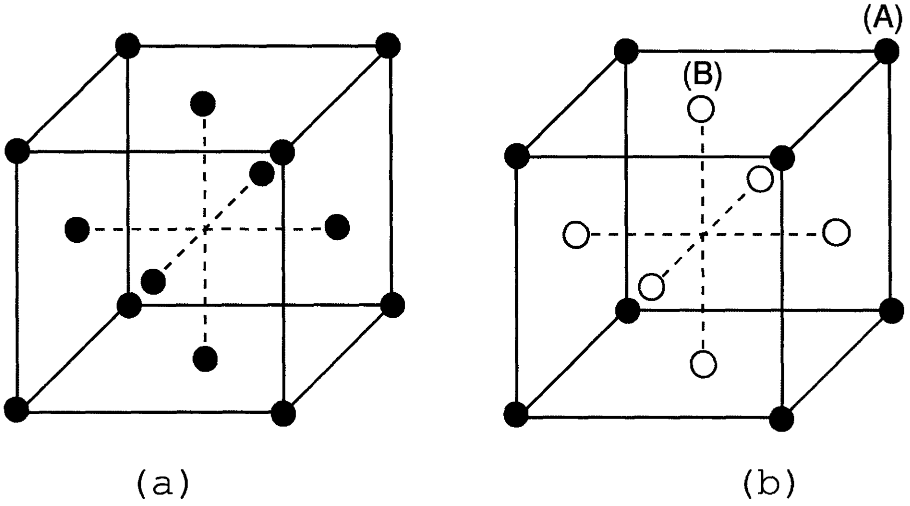

Figure 1-1: (a) The fcc unit cell and (b) the $L1_2$ unit cell of AB_3 compounds, in which minority atoms (A) occupy the corner sites and the majority atoms (B) occupy the face center positions.

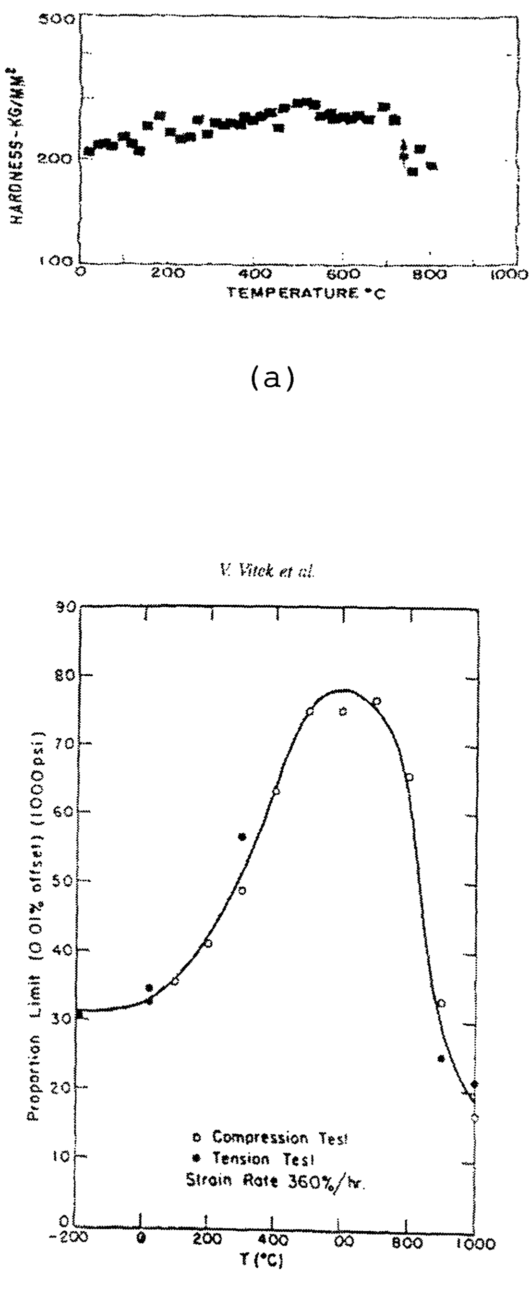

(a)

(b)

Figure 1-2: (a) Temperature-dependence of the hardness of polycrystalline Ni_3Al [2]; (b) Flow stress of polycrystalline Ni_3Al as a function of temperature [3].

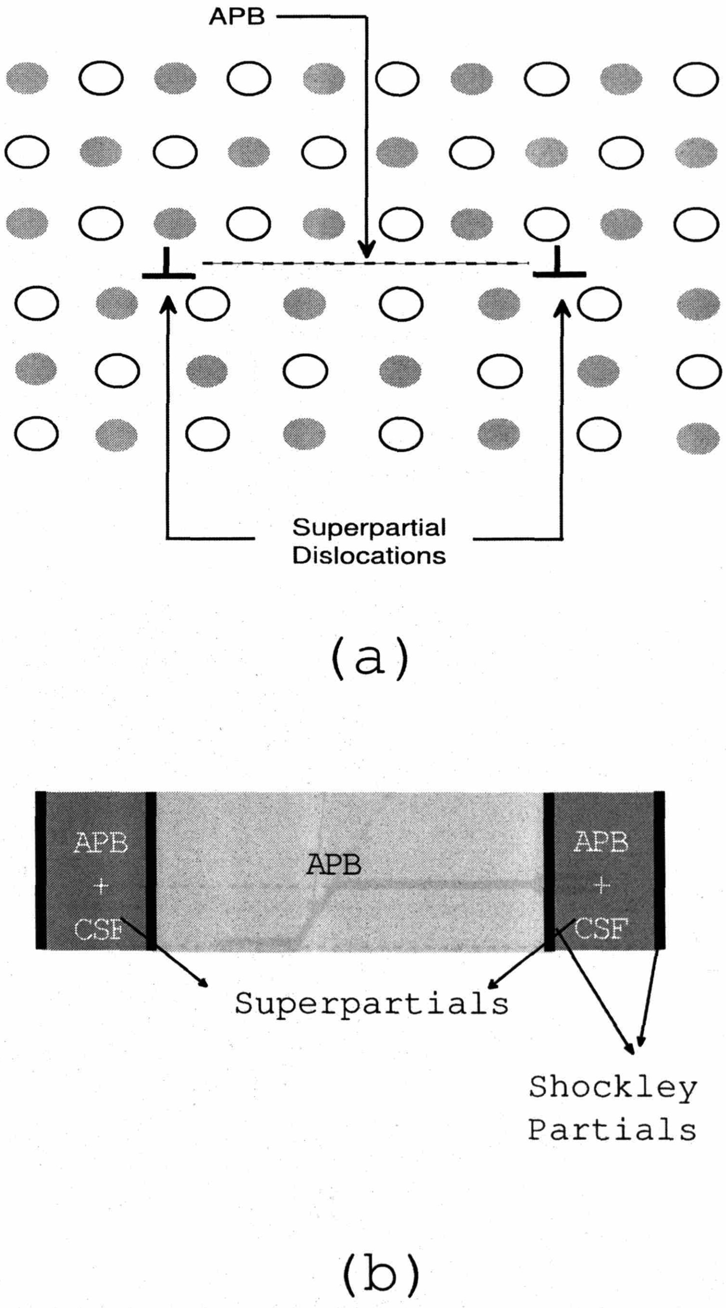

Figure 1-3: (a) Two superpartial dislocations connected by a patch of antiphase boundary (APB) [13]; (b) 2-D illustration of the dissociation of one superdislocation into two superpartials, bounding an APB ribbon, and the further dissociation of superpartials into Shockley partials.

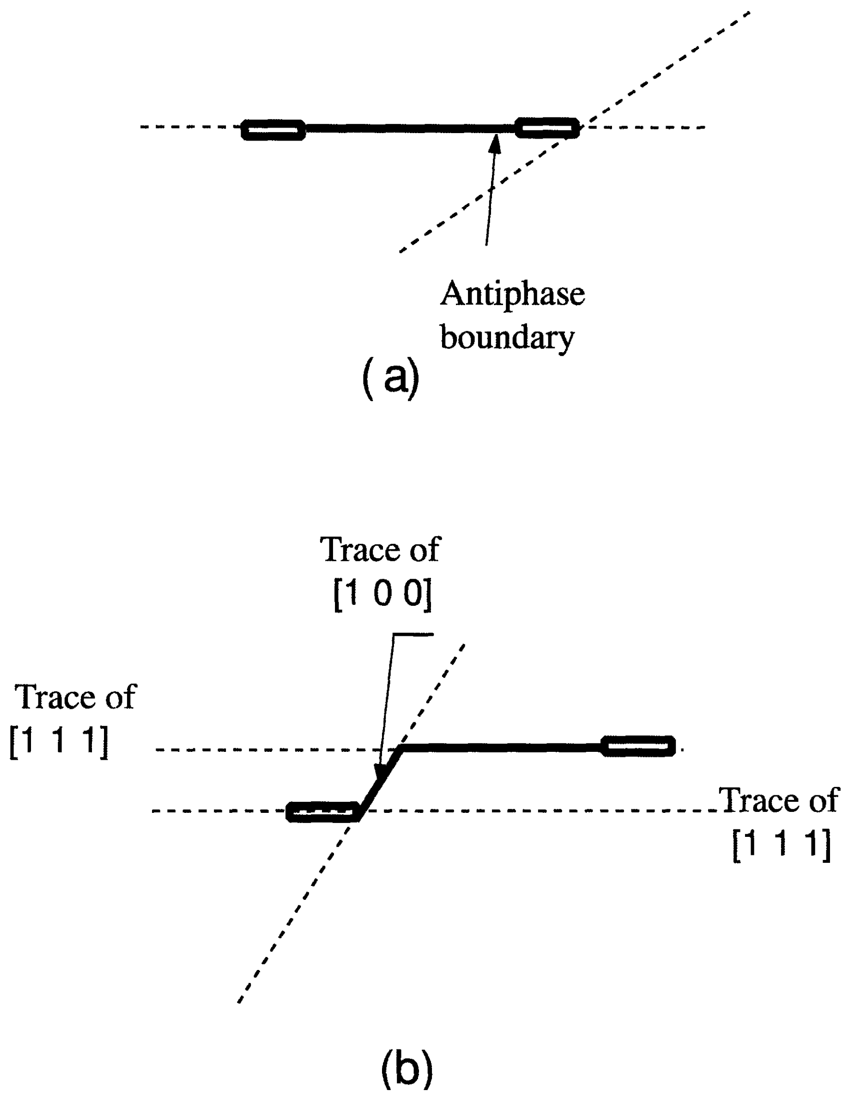

Figure 1-4: 2-D illustration of the configuration of (a) a mobile screw dislocation on an octahedral plane and (b) an incomplete Kear-Wilsdorf (K-W) lock.

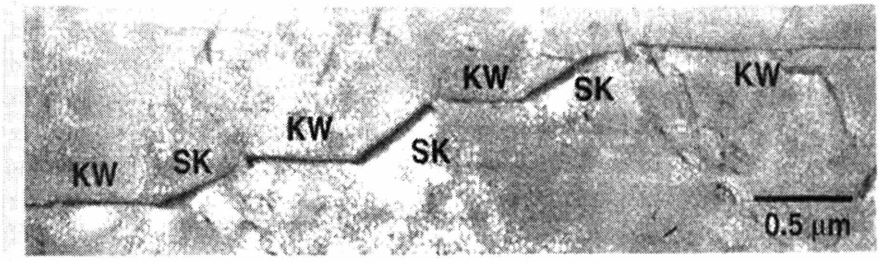

Figure 1-5: TEM image of a typical superdislocation with superkinks (marked as "SK") connecting sessile KW-locked screw segments [14].

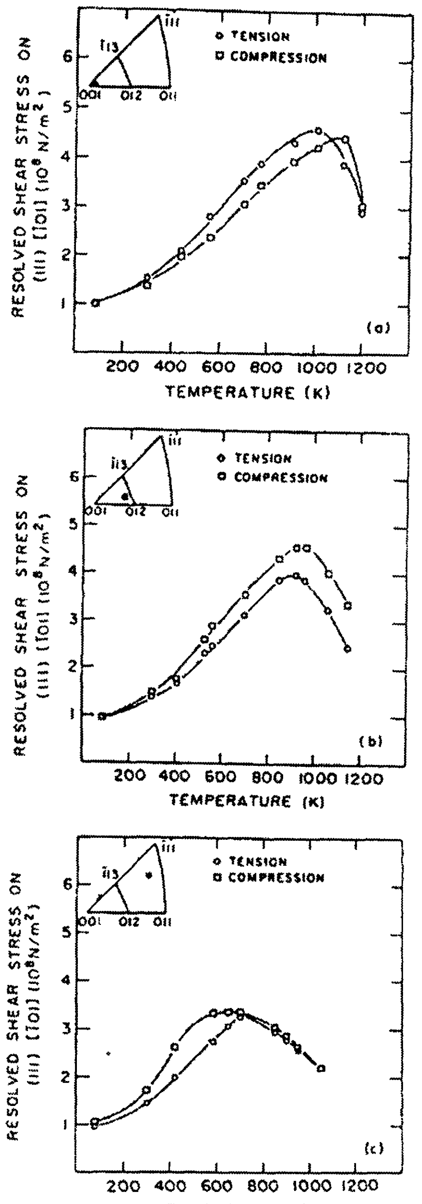

Figure 1-6: Temperature-dependence of the CRSS for (111)[$\bar{1}0\bar{1}$] slip, measured for $Ni_3(Al, Nb)$ in both tension and compression, for three different orientations of the tensile/compressive axis [15].

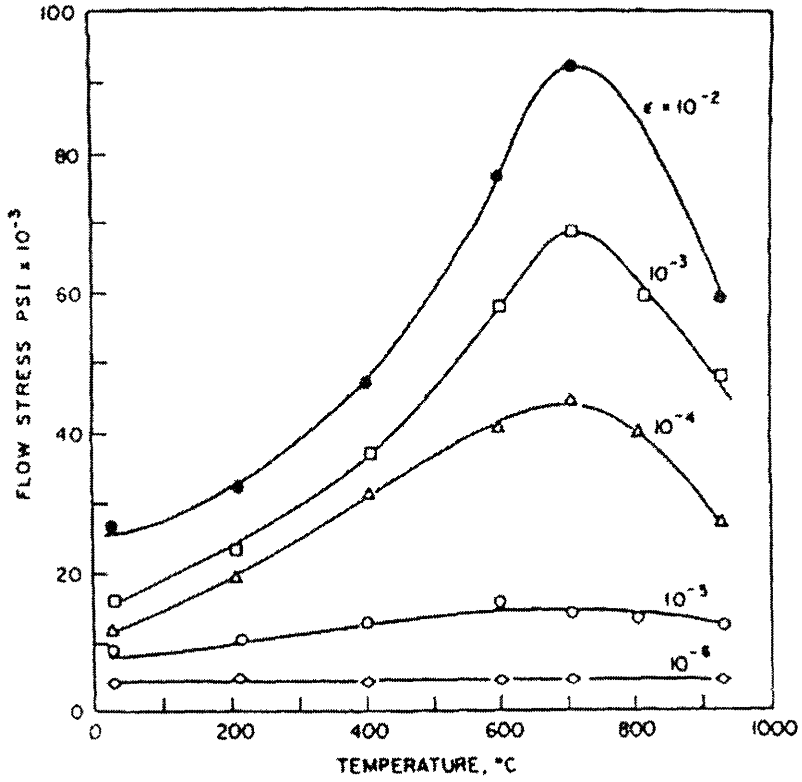

Figure 1-7: Dependence of the flow stress of Ni_3Al on temperature and plastic deformation offset [5].

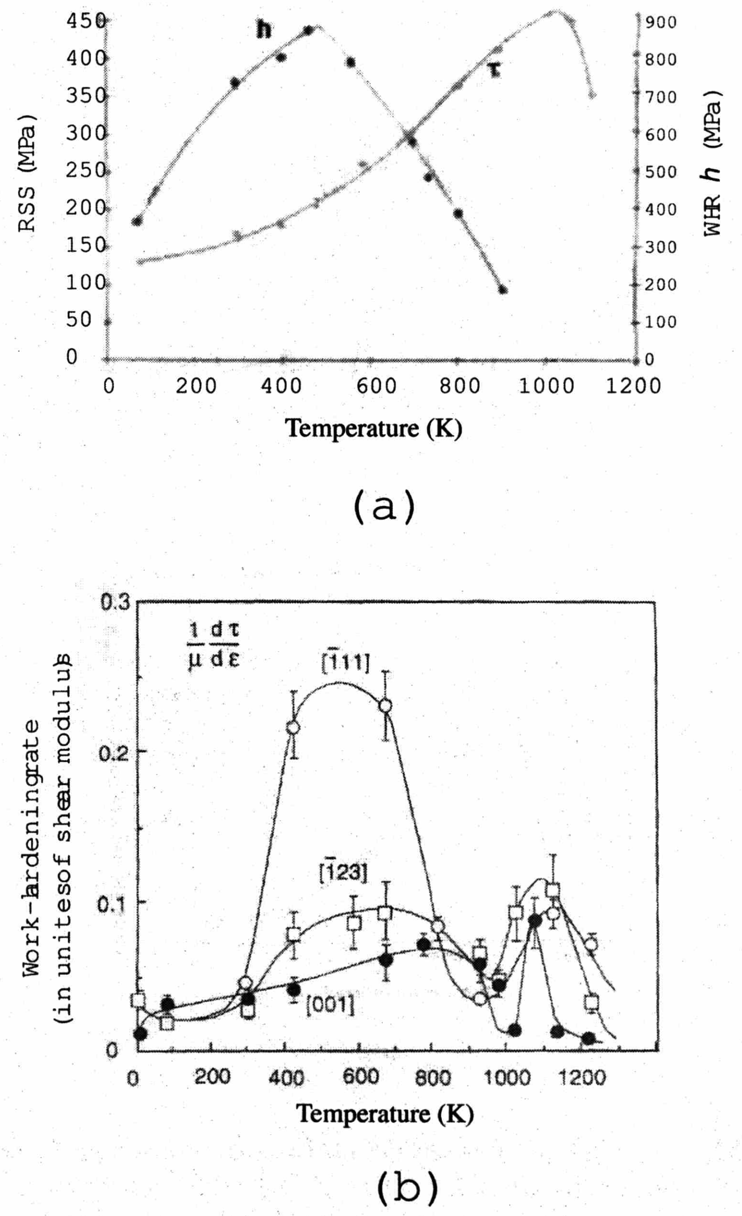

Figure 1-8: (a) Temperature-dependence of yield strength and strain hardening rate in $Ni_3(Al, 1.5\%Hf)$ [16]; (b) Orientation-dependence of strain hardening rate [17].

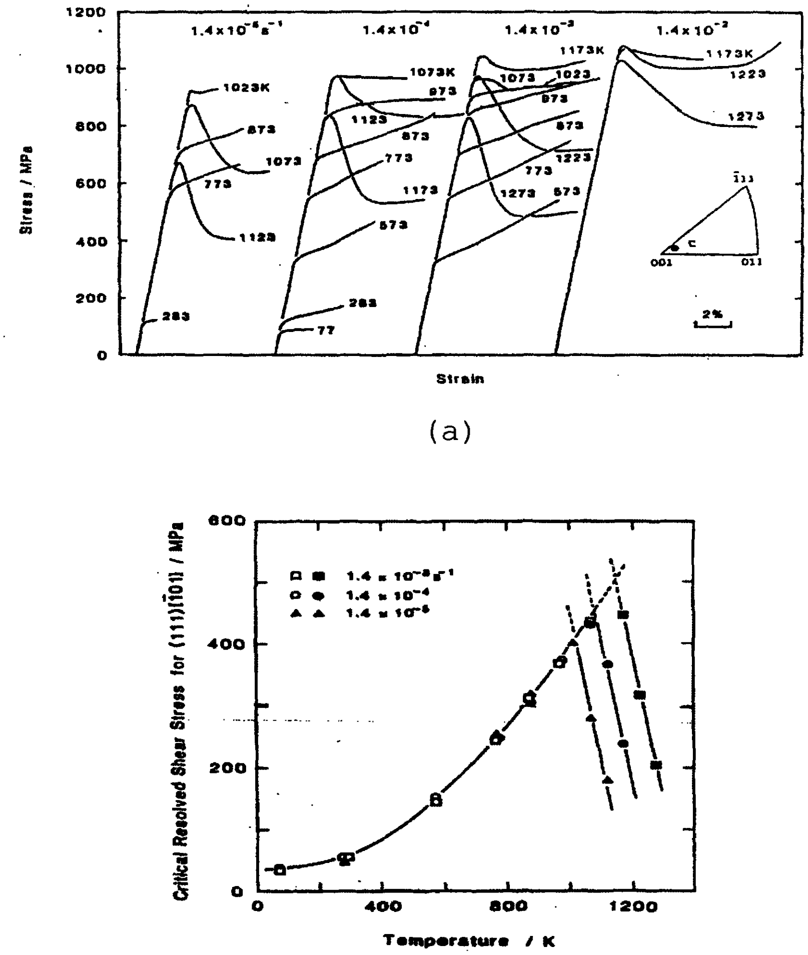

(a)

(b)

Figure 1-9: (a) Compressive stress-strain curves and (b) Relation between the yield strength vs. temperature of $Ni_3(Al, 5at\%Ti)$ for different temperatures and under different applied strain-rates [18]. For temperatures below $T_{p,\sigma}$, the yield strength is nearly strain-rate independent, while above $T_{p,\sigma}$, it is very sensitive to the applied strain-rate; The hardening rate in the yield anomaly region is also rate-independent.

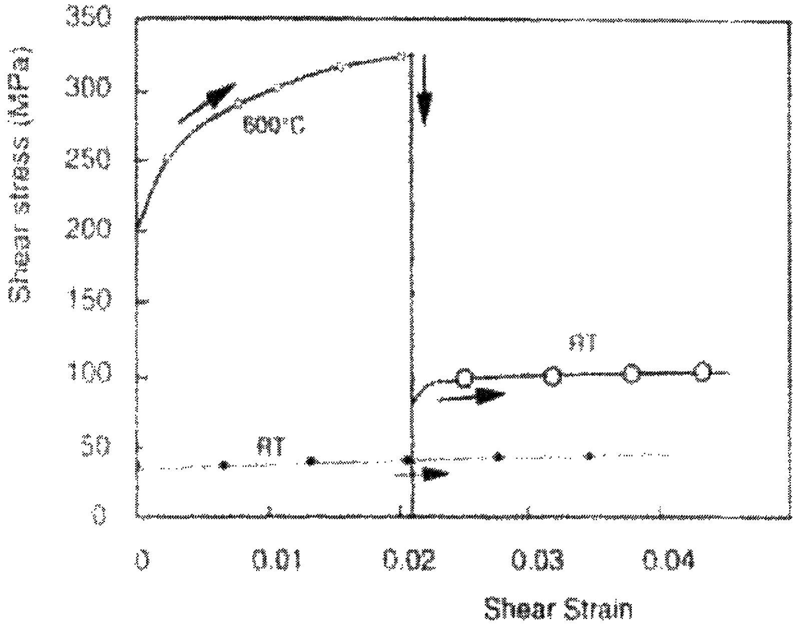

Figure 1-10: Example of a Cottrell-Stokes experiment deformed in compression along $[1\bar{2}3]$, conducted on $Ni_3(Al, 0.25at\%Hf)$, [19].

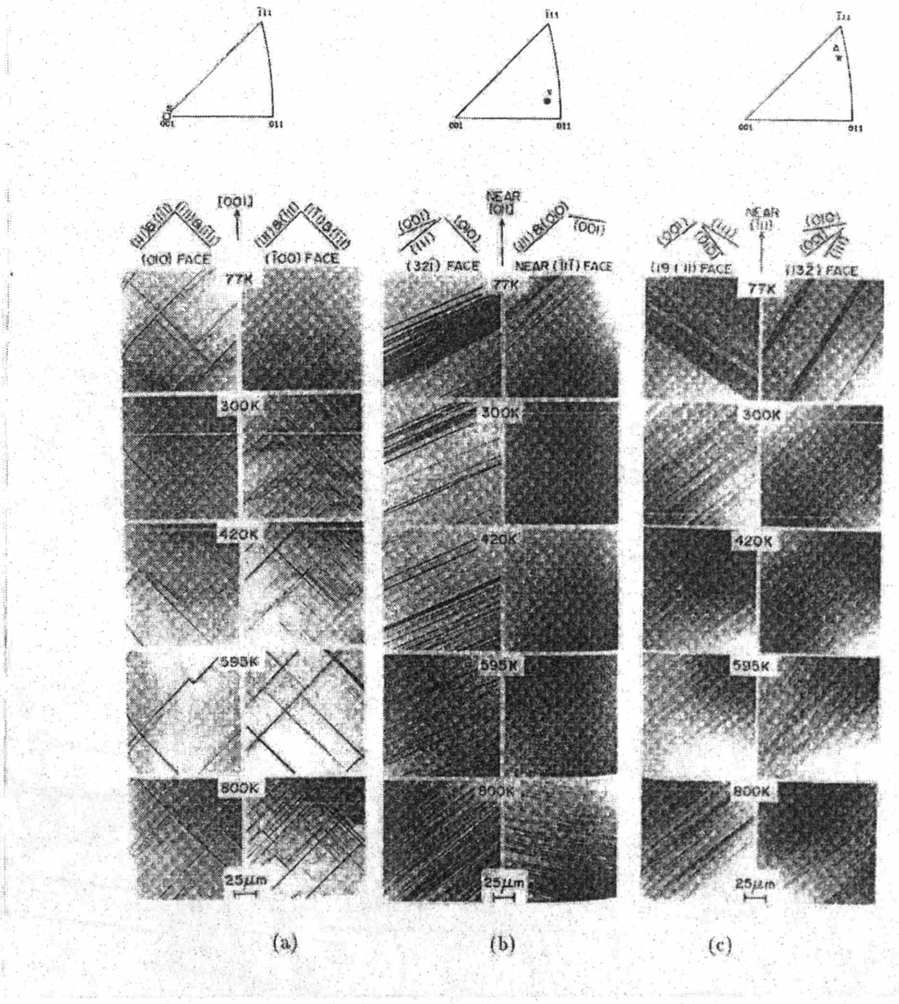

Figure 1-11: Slip traces on two orthogonal faces of (a) $< 001 >$ (b) near-$< 011 >$ and (c) near-$< 111 >$ oriented samples of $Ni_3(Al, Nb)$ at various test temperatures. [20] (For the left half of the center column (case b), the axes (001) and (111) have been incorretly switched. This is why it shows (001) slip at low temperature and (111) slip at high temperature, which is incorrect).

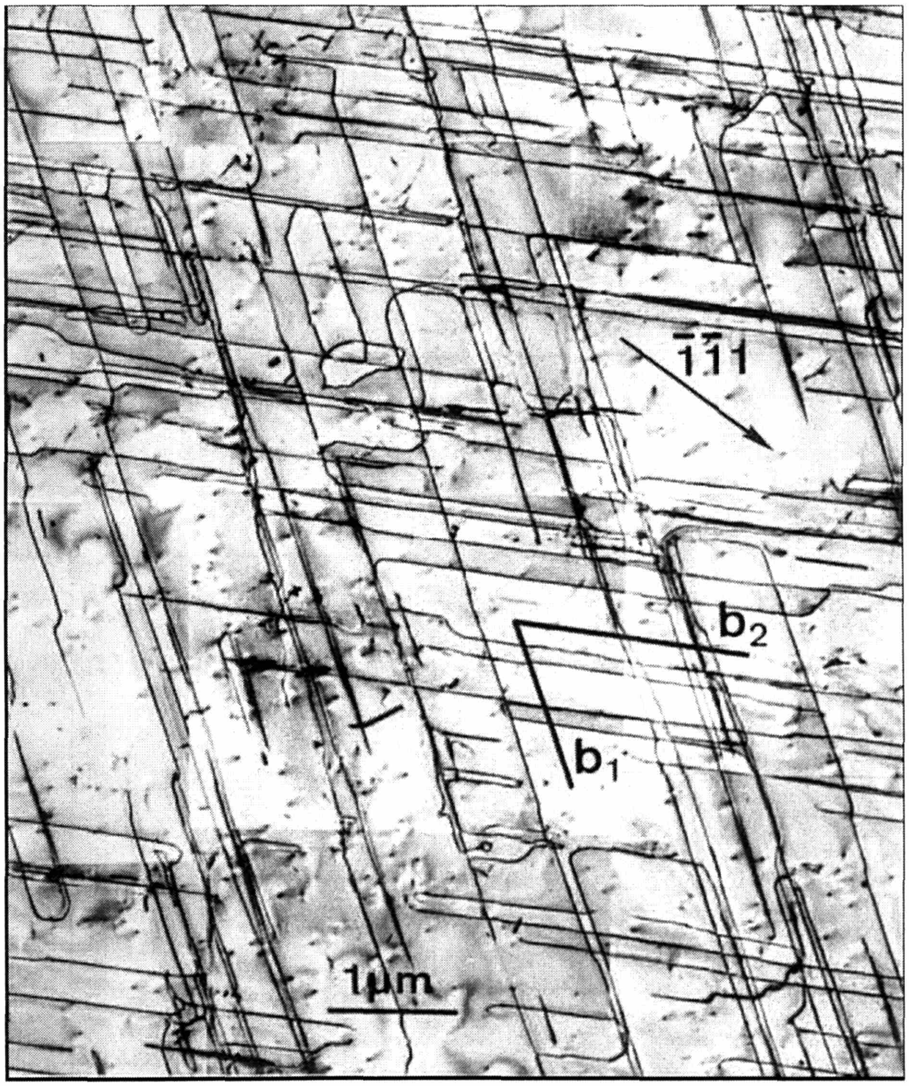

Figure 1-12: Dislocation structure of a Ni_3Al single crystal compressed along [001] at 873K (below $T_{p,\sigma}$ for the [001] orientation). [21]

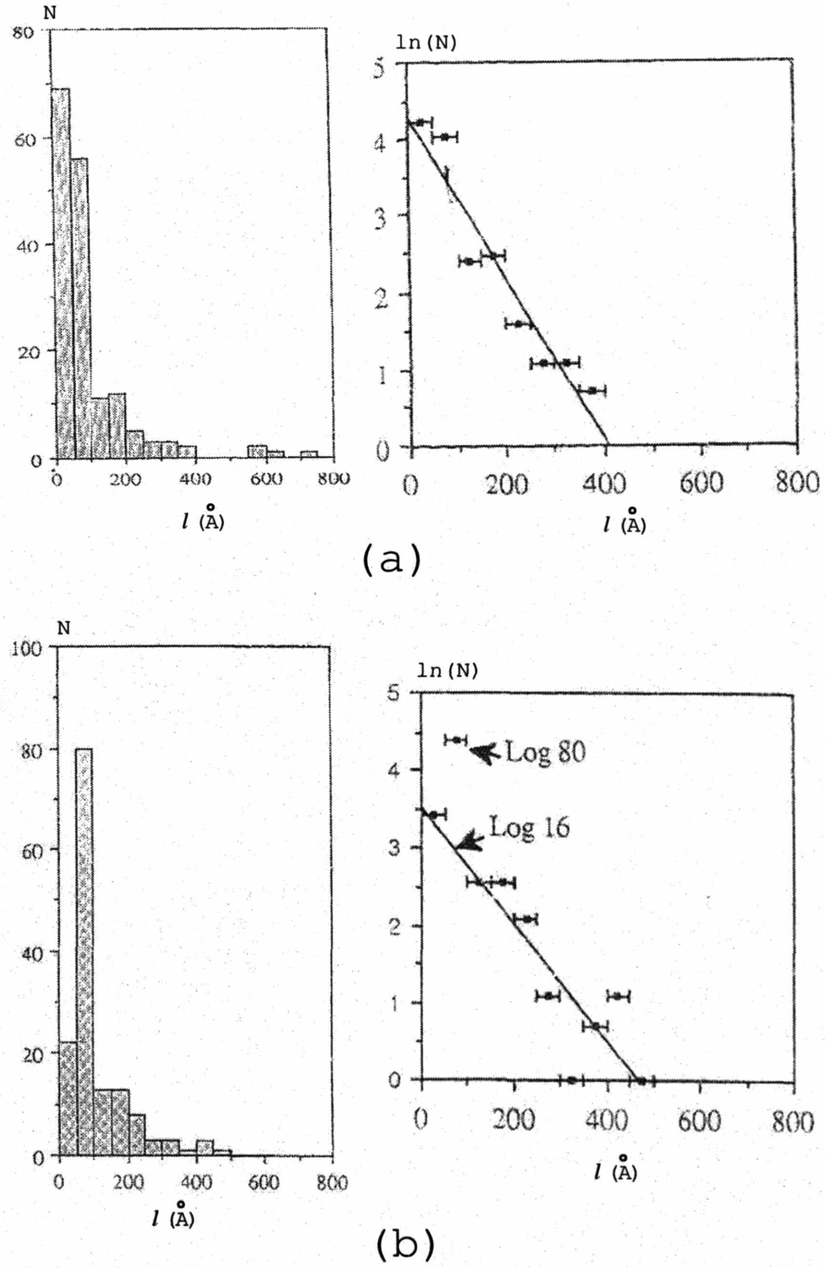

Figure 1-13: Number distribution of superkinks vs. their height in Ni_3Ga : (a) 673 K ; (b) room temperature (RT), 297 K [11].

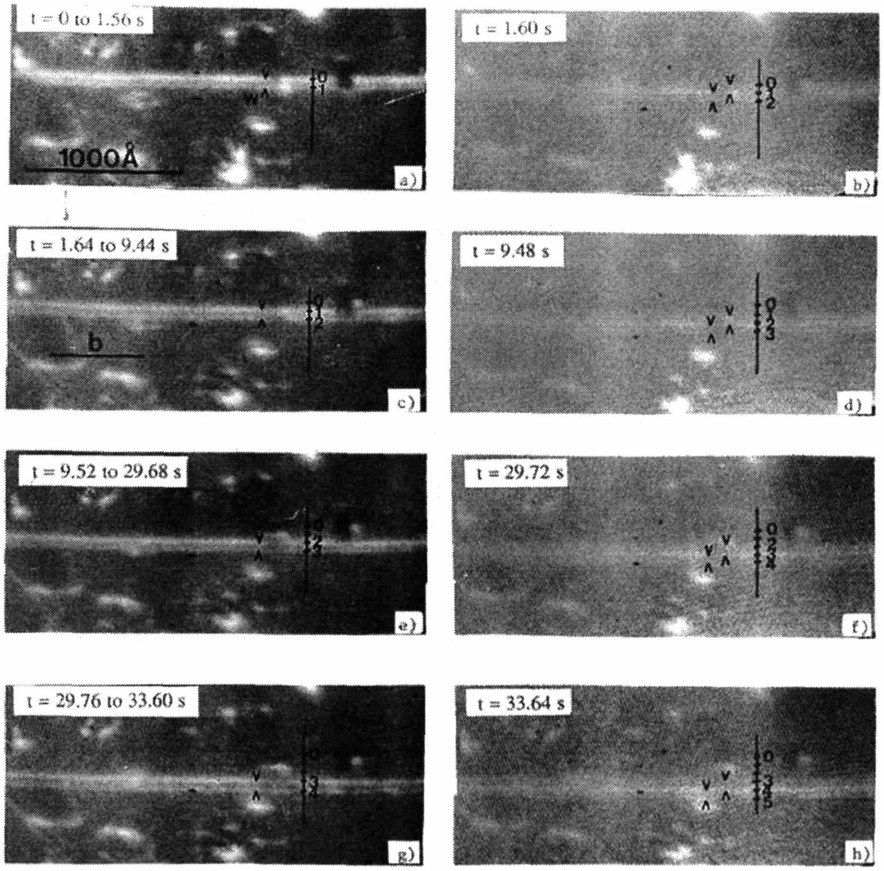

Figure 1-14: *In situ* observation of the jerky movement of screw dislocation in Ni_3Al at room temperature [12]: A screw dislocation is observed as sessile in one position (a) for several seconds and then suddenly jumps (downwards) to another position (b). The sessile/sudden-jump cycle goes on (c)-(h), and the distance between two sessile positions is found to be close to the APB width.

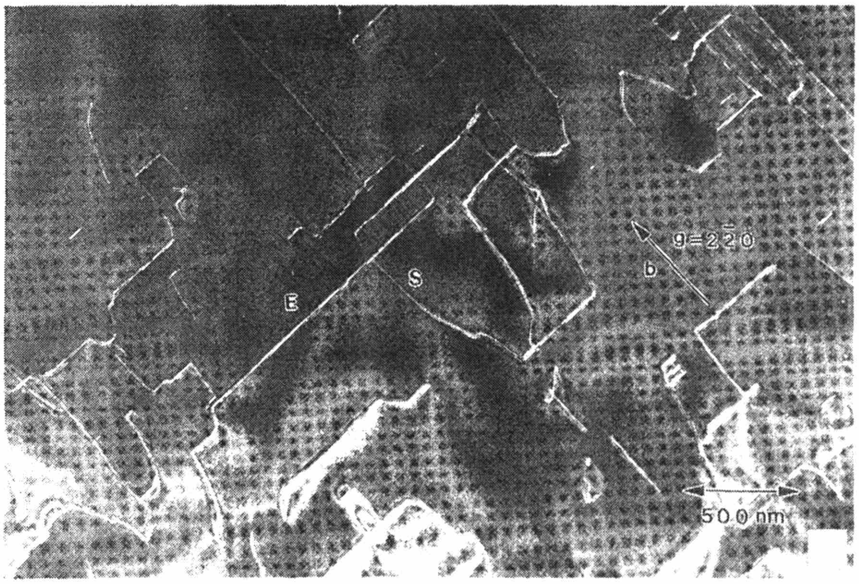

Figure 1-15: A weak beam image showing the distribution of dislocations in the primary $< 101 >$ $\{001\}$ slip in a sample deformed at a temperature above $T_{p,\sigma}$ [22]. Edge and screw dislocation densities in this cube slip system are comparable.

Chapter 2

Review of Existing Models of the Yield Anomaly Region

2.1 Overview

In the preceding chapter, we reviewed the physical background of the $L1_2$ structure crystal in the anomalous yield region, including both macro-mechanical properties and micro-structural observations. They serve as the goal and the physical basis of the current modeling and simulation work, respectively. Since the discovery of the anomalous temperature-dependence of hardness in Ni_3Al in 1957, great efforts have been devoted to research on $L1_2$ compounds. Many models and mechanisms have been put forward based on certain physical observations and various hypotheses. A thorough literature study is thus both a necessary and important part of this Ph.D. work, so that the proposed model and the resulting simulations can be solidly based on reasonable underlying mechanisms.

It is commonly accepted that the change of dominant slipping system from octahedral to cube planes is the reason for the abnormal/normal transition of temperature-dependence of yield strength (at least for uniaxial loading axes other than that close to the [001] orientation). In the anomalous yielding region, one of the most significant microscopic observations is the dominance of the long, straight, and locked screw superdislocations. In this regime, edge dislocations present themselves mainly as the links connecting the cross-slipped screw segments. Thus, most researchers related the yield anomaly to the cross-slip-caused low mobility of $\{111\} < 101 >$ screws, as was first suggested by Flinn [3].

In this chapter, the most representative models for the anomalous octahedral slip will be illustrated, in the three categories of "steady-state models", "dynamic-simulation models" and "hardening models", respectively. Detailed discussions of each model will also be presented.

2.2 Review of Existing Models

2.2.1 The Steady-state Models

"Point-obstacles" models

Early research work in $L1_2$ single crystals mainly focused on the property of yield anomaly, and the initial quantitative models were based on the "point-obstacle" assumption. Cross-slip was considered to be thermally activated and to occur locally, forming equally-spaced pinning-points along the screw dislocation. These point obstacles were assumed to be dissolved athermally, when the adjacent screw segments bowed out to a critical curvature. Meanwhile, by a steady-state assumption, a new pinning point was created for every released one, and the pinning-unpinning cycle went on, as shown in Figure 2-1(a). Under the condition of constant applied strain-rate, the flow strength is expressed as:

$$\sigma = \sigma_0 \exp(-\frac{H_l}{3kT}), \tag{2.1}$$

where H_l is the activation enthalpy for locking, k is the Boltzmann constant and T is the absolute temperature. The yield anomaly is physically explained by postulating that more and more "point-obstacles" are generated with decreased pinning-point spacing at higher temperatures, and a higher level of effective stress is needed to keep dislocations in a steady-state motion.

As the earliest quantitative model to explain the anomalous yield behavior, the "point-obstacle" model does present a positive relation between the flow strength and the temperature. However, the positive temperature-dependence expressed in Eqn 2.1 is very weak. For example, the yield strength of Ni_3Al at 700 K is typically $3 \sim 4$ times its strength at 300K. In order to account for this, the locking enthalpy calculated according to Eqn. 2.1 has to be only around 4×10^{-4} eV, which is unreasonably low.

Besides, since unlocking in "point-obstacle" models is purely mechanical, once the applied stress exceeds the critical level to overcome the obstacles, unlocked screw dislocations would move with Newtonian viscous velocity, $V^\alpha = \tau^\alpha b/B$, which linearly depends on the resolved shear stress τ^α. Thus, the predicted yield strength is very strain-rate dependent:

$$\dot{\gamma}^\alpha = \rho^\alpha b V^\alpha = \frac{\rho^\alpha \tau^\alpha b^2}{B}. \tag{2.2}$$

Hirsch [23] also criticized this locking as rate-controlling dislocation dynamics by pointing out that if $B \sim 5 \times 10^{-5}$ N$m^{-2}s$, and a representative shear stress was $\tau^\alpha \sim 200MPa$, for an applied strain-rate of $10^{-4}s^{-1}$, the mobile dislocation density was unreasonably low, $\rho^\alpha \sim 0.04cm^{-2}$. This means that the average dislocation velocity determined by the locking as rate-controlling mechanism is simply too high to be true.

Most of all, with the improvement of experimental techniques, a number of TEM pictures published subsequently clearly illustrated that the screws were locked in long, straight segments, but not by "point-obstacles". Thus the basic assumption for these models is found to be questionable.

Though "point-obstacle" models are currently considered as mostly of historical significance in explaining the yield anomaly phenomena, the contributions of some of these models in understanding the details of cross-slip process are still studied and referred to in recent research.

Based on different assumptions for the local cross-slip process, different "point-obstacle" models have developed various expressions for the locking activation enthalpy H_l. Takeuchi and Kuramoto [24] described that the locking (cross-slipping) process was aided only by the resolved shear stress (RSS) on the cube cross-slip plane, τ_{cb}. Hence, H_l is given as:

$$H_l = H_{l0} - V_c|\tau_{cb}|, \tag{2.3}$$

where H_{l0} is considered a constant and V_c is the stress-independent activation volume. The absolute value, $|\tau_{cb}|$, reflects the possibility of cross-slip in either direction on the cube plane. The introduction of a τ_{cb} term does predict a breakdown in the Schmid law, but the predicted crystallographic orientation-dependence of uniaxial yield strength does not agree well with experimental results. Besides, the property of tension-compression asymmetry, which has been seen experimentally [4], is not exhibited in the locking enthalpy given by Eqn. 2.3.

Later, Paidar, Pope and Vitek (PPV) [25] revised Takeuchi and Kuramoto's model by specifying the locked configuration and modifying the cross-slipping procedure based on the cross-slipping theory established by Friedel and Escaig [26, 27] for fcc materials. In Escaig's model, cross-slip was initiated with the constriction of the stacking fault on an octahedral plane between the Shockley partials as shown in Figure 2-2 (a), followed by cross-slip onto an intersecting octahedral plane. Since the superpartials in $L1_2$ crystals have the same Burgers vector as the dislocations in fcc crystals, and also dissociate into Shockley partials, PPV proposed a similar constriction-initiated cross-slip procedure, as shown in Figure 2-2 (b). The constricted leading superpartials are assumed to cross-slip onto a cube plane, and then to expand on a cross-slipping octahedral plane, pinning the total dislocation in a non-planar locked configuration. The detailed locking (cross-slipping) process was illustrated in three steps: (i) Constriction of the glissile core of the leading screw superpartials on the (111) plane, (ii) movement of the constricted superpartials along the (010) plane by a distance of $b/2$, and (iii) further splitting of the cross-slipped superpartials onto the cross-slip $(1\bar{1}1)$ plane. Core transformations of the superpartials (the first and the third steps), rather than the cross-slipping on the cube plane (the second step), are considered as the essential parts of the locking process. PPV noted that even though the superpartials are screw-orientated, the dissociated Shockley partials have edge components. Thus, the non-Schmid stress components τ_{pe} and τ_{se} (on the original and cross-slipping octahedral planes perpendicular to the Burgers vector of superpartials, as shown in Figure 2-3) are involved in the cross-slip process. According to the sign of the applied stress, these non-Schmid stress components (τ_{pe} and τ_{se}) either constrict or expand the core of the superpartials, which in turn assists or inhibits the cross-slip process, respectively. The locking activation enthalpy was decomposed into two parts, assumed independent of each other, corresponding to the constriction and the cross-slip process, respectively:

$$H_l = W_c + H_{CS}. \tag{2.4}$$

The constriction part W_c is a modified version of the constriction energy given by Escaig. The cross-slip part H_{CS} includes the self-energy and interaction energy of two cross-slip-generated jogs on the cube plane, the energy gained by transferring part of the APB ribbon from the octahedral plane to the cube plane, and the work done by τ_{cb}. The expression for H_l as a summation of W_c and H_{CS} is somewhat complicated, but under the assumption that the magnitude of the work done by τ_{cb} is much less than the energy gained by cross-slip, H_l can be simplified into a linear form:

$$H_l = H_{l0} - V_0(\tau_{pe} - \kappa\tau_{se}) - V_c|\tau_{cb}|, \tag{2.5}$$

where V_0 and V_c are the corresponding activation volumes, and they are derived as $V_c = \frac{b^4}{8}\sqrt{\frac{\pi\mu}{\Delta E}}$ and $V_0 = \frac{b^3\lambda}{2\pi}$. Here, μ is the shear modulus, λ a dimensionless parameter, and ΔE is the energy gained per unit length by cross-slip. The magnitude of ΔE is estimated to be $10^{-12}Jm^{-1}$ by applying the APB energy ratio of octahedral plane to cube plane as $\gamma_o/\gamma_c = 1.4$ (a typical value in Ni_3Al) and the cross-slipped distance $w = b/2$ (the assumed cross-slip distance on cube plane). Thus the value of V_c is around $5b^3$. The factor λ in the expression of V_0 is considered to be dependent on the value of APB energy on the octahedral plane. The magnitude of λ was not explicitly specified in the PPV model, but since the constriction was assumed as the essential part in the cross-slip process, the value of λ should make the activation volume V_0

larger than V_c. (Qin and Bassani [67] analyzed the effects of different values of V_0, V_c and κ on the orientation-dependence and tension-compression asymmetry of yield strength, and similar parameter sensitivity studies and simulations are available in the author's Master's thesis [68]).

The simulation results of the PPV model were compared with the experimental work of Umakoshi, *et al.* [4] and the work of Ezz, *et al.* [28] on single-crystal Ni_3Al doped with Nb. The predicted results successfully matched the experimental data in the properties of orientation-dependence and, especially, tension-compression asymmetry of yield strength. For this reason, the PPV-type locking mechanism was accepted and implemented in many later quantitative models.

On the other hand, the PPV-type cross-slip process was also questioned by some researchers. First, the PPV model assumed a non-planar locked configuration with the leading superpartials lying on the cross-slip octahedral plane $(1\bar{1}1)$. Based on anisotropic elastic analysis, Schoeck [29, 30] pointed out that the splitting of the superpartial core on the $(1\bar{1}1)$ plane was not energetically favorable. Schoeck's point was supported by the atomistic simulation results of Parthasarathy and Dimiduk[31]. Therefore, the τ_{se} term may disappear from Eqn. 2.5. Secondly, the separation between the Shockley partials was reported to be very small ($\sim b$). It can not be resolved in screw dislocations and can only barely be resolved by TEM weak-beam techniques in edge dislocations. Thus, some researchers argued that it was improper to use elastic theory in deriving the locking enthalpy, as in the PPV model. Besides, the locking activation enthalpy was derived under certain assumptions such as: τ_{pe} and $\tau_{se} \ll \gamma_{CSF}/b$ and the cross-slipped distance $w = b/2$; and was simplified into the linear form (Eqn. 2.5) with the assumption of $\tau_{cb}b^2 \ll \Delta E$. γ_{CSF} was reported to be in the range of $200 \sim 350mJ/m^{-2}$, so the magnitude of γ_{CSF}/b is around $1GPa$. So the first assumption is plausible. The second assumption is under question, because both IKWs and CKWs have been observed, and the cube plane APB width of IKWs can be much longer than $b/2$ [32]. But we need to keep in mind that in the PPV model, w represents the initial cross-slipped distance on a cube plane, while the observed cross-slipped distance may be the result of the evolution of K-W locks under applied stress.

The third assumption also needs further consideration. If we assume $\tau_{cb} \sim 100MPa$, a reasonable value for uniaxial loading orientations other than that very close to [001], the magnitude of $b^2\tau_{cb} \sim 10^{-12}Jm^{-1}$, which is similar to the value of ΔE. Thus, for these orientations, H_l can not be simplified to the linear expression form Eqn. 2.5.

Discussions about the cross-slip mechanism and the properties of orientation-dependence and tension-compression asymmetry of yield strength are still going on. Many experiments reveal that the non-Schmid properties of $L1_2$ single crystal are greatly composition-dependent, and are even claimed to disappear in pure Ni_3Al single crystals [33]. In a review article, Veyssiere and Saada argued that "It is fair to say that the actual orientation-dependence appears in fact to be more complicated than a simple theoretical analysis could predict, unless of course this theory is appropriately parametrized." [34].

Superkink Unlocking Models

As we have summarized, the "Point-obstacle" rationalization of the yield anomaly is in conflict with the observation of long, locked K-W form screw segments. To overcome the above limitations of pinning-point models, more physically-based models have been put forward. These models have proposed new unlocking mechanisms corresponding to the K-W locks, and the unlocking process is considered to be rate-controlling part of the steady-state movement of screw dislocations. One of them is the superkink (also termed as macro-kink) unlocking mechanism.

Superkinks were spotted in very early TEM studies, but it was Sun and Hazzledine [35] who first proposed and emphasized that locked screws could be unlocked by the shuttling of the edge-orientated superkinks. After that, many superkink models have been put forward [14, 36, 37].

Sun [36] studied the expansion of superkinks as they glided along the screw dislocation, and concluded that if the superkink height was larger than a critical value l_c, the superkink would bow out and generate new superkinks. Otherwise, the superkink just glided out to the end of the screw. Thus, in order to sustain a continued deformation, the average dislocation height $\bar{l}$ must be no shorter than l_c. The yield strength is deduced from the condition $\bar{l} = l_c$, and it is found to be inversely proportional to $\bar{l}$.

The superkink unlocking mechanism was also adopted in Louchet's [37] extended locking/ unzipping (ELU) model. The basic idea of this model is: a screw dislocation is assumed mobile if the longest superkink on it is longer than a critical value l_e, which depends on the jog resistance at the ends of superkinks under a given applied stress. The distribution of screws $(P_{scr}(l))$ is then derived over the total screw dislocations as a function of the height of the longest superkinks on it, based on an assumed distribution of superkinks $P_{sk} = P_0 \exp(-l/l_0)$. Both $P_{scr}(l)$ and $P_{sk}(l)$ are schematically plotted in Figure 2-4. Meanwhile, sufficiently long superkinks $(l > l_m)$ may bow out and generate new sessile screw segments and new mobile superkinks. Both l_e and l_m are derived to be inversely proportional to the applied stress. Under the condition of constant applied strain-rate, the yield strength is viewed as the stress magnitude that balances the multiplication rate and the exhaustion rate of the mobile screw dislocations. The multiplication rate is considered to be proportional to the number of superkinks that are longer than l_m, which is illustrated as the shaded area under P_{sk} for $l > l_m$. The exhaustion rate is considered to be proportional to the number of screws on which even the longest superkink is shorter than l_e, as illustrated by the shaded area under P_{scr} for $l < l_e$. With the assumption that the average superkink height decreases with increasing temperature, both P_{scr} and P_{sk} drift to the left (where the value of l is smaller) in Figure 2-4. Thus, the area representing exhaustion rate increases, while the area related to multiplication decreases. Therefore, to rebalance the exhaustion and the multiplication rates, both l_e and l_m need to decrease, which in turn yields an increase of flow strength (Figure 2-4).

Despite the different formats of illustration, the above superkink models are similar to each other in the following ways:

1. Plastic strain is assumed to be produced by the shuttling of superkinks along the previously locked screw segments, in the octahedral planes.

2. Resistance forces at the end of the superkink (either the pinning strength at the kink junctions or the force due to imbalance of the line tension at the two

superkink ends) are independent of the superkink height.

3. Yield strength is derived based on an assumed pre-existing distribution of superkinks or a characteristic length of superkink (e.g. $\bar{l}$). The shorter the superkinks, the higher the yield strength. This is consistent with the study of Dimiduk [38], which found that the height of the superkinks varied as the inverse of the strength of the alloys.

4. Yield anomaly is achieved via an assumed decrease in superkink's height with increasing temperature, due to the temperature-enhanced locking frequency. This assumption has been experimentally confirmed by Couret, *et al.* [11].

Both Sun and Louchet's models are incomplete quantitative models. The temperature-dependence of superkink's height, which is the essential part of modeling the yield anomaly, is explicitly assumed, but not defined. As for the strain-rate insensitivity, both models claimed a pure mechanical (athermal) unlocking mechanism; thus the critical unlocking stress (yield strength) was determined by the resistance forces and the superkink height, but not by the applied strain-rate. However, this proposition needs further consideration. If the critical strength hardly depends on the applied strain-rate, neither does the mobile dislocation density, because both l_c and l_e are inversely related to the applied stress. Thus, according to Orowan's relation:

$$\dot{\gamma}^{\alpha} = \rho_m^{\alpha} b \bar{V}^{\alpha}, \tag{2.6}$$

the gliding velocity of superkinks must be very sensitive to the applied strain-rate. However, based on the assumed Newtonian viscous velocity, it is not clear, under similar stress levels, why the dislocation velocity should entirely vary so much. Therefore, this explanation for strain-rate insensitivity may not be self-consistent.

Usually, the screw dislocations have very complicated non-planar configurations, with adjacent locked segments and the connecting superkinks lying in different octahedral planes. Most of the superkink unlocking models simplified the problem by assuming a two-dimensional planar configuration, without providing details of the unlocking process. That is why Hirsch's [23] superkink model, which presented very detailed mechanistic descriptions of the formation and evolution of the K-W locks and a full illustration of the superkink unlocking mechanism, is widely referred to and deemed as the most successful superkink unlocking model.

Hirsch assumed that locking originated locally first by the cross-slipping of the leading superpartial, and the resulting jogs on the cube plane generated during the cross-slip would readily sweep along the dislocation, until an edge dipole has been formed (Figure 2-5 (b)), so a long cross-slipped screw segment (K-W locks) would be formed. The unlocking process is the essential part, and Hirsch's unlocking mechanism is schematically illustrated in Figure 2-5. It was assumed to start with a thermally-activated cross-slip of the leading superpartials (L) at the end of the K-W lock segment, and a small segment of cross-slipped leading superpartials annihilates with itself (L and L'), as shown in Figure 2-5 (c)-(d). After the cross-slip and the annihilation, the jog on the leading superpartials is mobile and the superkinks can then start the unzipping process to the left, as shown in Figure 2-5 (e)-(g). The driving force for unzipping is derived from a simplified 2-D model, without consideration of the resistance force on the jogs in the cube plane. As schematically illustrated in Figure 2-6 (a), the movement of superkinks is driven by the decrease of energy, ΔE, and inhibited by the line tension forces, T_{line}. As the superkink passes along the locked screw segment, an APB tube is formed as shown in Figure (2-5 (g)), which is also TEM-observed (Figure 2-6 (b)). Even though the detailed mechanism of forming such an APB tube is still under research (Hirsch and Veyssiere have published several papers, recently, debating the formation of APB tubes [39, 40, 41]), these observed APB tubes clearly present the trace of superkinks and strongly support the superkink unlocking mechanism. Besides, micro-structures such as long cross-slipped screw segments, superkinks and edge dipoles are also observed *post-mortem*, supporting the essential idea of Hirsch's superkink unlocking mechanism.

Despite the extremely sophisticated geometry and mechanisms proposed to describe the unlocking process, Hirsch's superkink unlocking mechanism was eventually simplified into a "steady-state" movement of one screw segment (Figure 2-1 (b)).

Since unlocking is assumed rate-controlling, and in each locking-unlocking cycle, the screw segment advances by a distance of $2l$ (l is the height of the superkink), the average velocity of the screw dislocation is given as $v = 2l/t_u$. Here t_u is the time needed for each unlocking procedure, which is the inverse of the unlocking frequency f_u. Therefore, the average velocity is finally derived as:

$$v = \frac{2l}{t_u} = 2lf_u = 2l\nu_0 \exp(-\frac{H_u}{kT}), \tag{2.7}$$

where H_u is the unlocking enthalpy, and ν_0 is the Debye frequency.

On the other hand, whenever a screw segment is free, it moves a distance of l with free-flight velocity, v_f, until it gets locked again. Thus $v_f = l/t_l$, where t_l is the time needed for the locking procedure, and is the inverse of the locking frequency f_l:

$$v_f = \frac{l}{t_l} = lf_l = l\nu_0 \exp(-\frac{H_l}{kT}), \tag{2.8}$$

where H_l is the locking enthalpy.

Combining Eqns. 2.7 and 2.8, we get:

$$v = 2v_f \exp(-\frac{H_u - H_l}{kT}). \tag{2.9}$$

The activation enthalpy for unlocking, H_u, is derived as:

$$H_u = H_{u0} - V(l)(\tau - \tau_a), \tag{2.10}$$

where H_{u0} is the activation enthalpy for the cross-slip of the leading superpartials illustrated in Figure 2-5(d), $V(l)$ is the activation volume, which is proportional to the kink height l, and $\tau_a = p\mu b/l$ is the resistance strength to the bypassing of the superkinks, derived from the simplified 2-D configuration given by Figure 2-6(a). Here p is a non-dimensional geometrical parameter, and μ is the shear modulus. Since τ_a

is inversely dependent on l, Eqn. 2.10 can be rewritten as:

$$H_u = H_{u0}^* - V\tau; \text{ where } H_{u0}^* = H_{u0} + V\tau_a. \tag{2.11}$$

Explanation of the yield strength anomaly still depends on an assumed decrease of superkink height with increasing temperature, the mechanisms of which were not quantitatively derived in the model. For the property of strain-rate insensitivity, some review papers have asserted that it was achieved due to the large athermal stress component (τ_a) involved in Hirsch's model. But actually, it is the large magnitude of the activation volume ($l \sim 100b \Rightarrow V \sim 100b^3$) that makes the average velocity very sensitive to the change of the applied stress. Thus, according to Orowan's relation (Eqn. 2.6), a very small increase in stress can increase the average velocity dramatically, which can balance large change in the applied strain-rate. Therefore, a small strain-rate sensitivity of yield strength is expected.

Hirsch directly adopted the PPV version of locking enthalpy H_l in Eqn. 2.9 in order to capture the prediction for all the non-Schmid effects, even though the locked configuration of screws in Hirsch's model differs greatly from that assumed in the PPV model. However, details of locking procedure were not the focus of Hirsch's model.

Self-unlocking Mechanism

Another approach to unlock the K-W segments is the self-unlocking model proposed by Caillard and Paidar [42]. This model is based on *in situ* TEM observations of the movement of screw dislocations (shown in Figure 1-14) at room temperature.

The jerky movement of one screw is simplified into a 2-D model, shown in Figure 2-7, in projection along the screw direction. The leading superpartials cross-slip to the cube plane first, glide for a distance w, then back-cross-slip onto an adjacent primary octahedral plane (Figure 2-7 (a)). This configuration is then mobile until the trailing superpartials encounter the cube plane on which the leading superpartials initially cross-slipped (Figure 2-7 (b)). Unlocking is assumed to be caused by the cross-slipping of the trailing superpartial onto this cube plane, resulting momentarily in a glissile configuration. Meanwhile, the leading superpartial has the chance to cross-slip again, and the cycle continues. The free glide on octahedral planes was assumed to be much faster than that on the cube plane, due to the comparably much smaller frictional forces. Therefore, the kinetics of locking and unlocking closely depend on the average velocities of leading and trailing superpartials on the cube planes, under their corresponding driving stresses.

Stress analysis was carried out for both leading and trailing superpartials according to linear elasticity, without considering the core structure of the Shockley partials. The driving components on the cube plane for both leading and trailing superpartials (τ_{cs}^{t} and τ_{cs}^{l}) have been derived, and a critical stress $\tau_{critical}$ was defined as the applied octahedral system stress under which $\tau_{cs}^{t} = \tau_{cs}^{l}$. Based on different applied stress levels, τ, three hypothetical conditions were proposed:

1. If $\tau > \tau_{critical}$, the cube-slip driving force on the trailing partial will exceed that of the leading one, $\tau_{cs}^{t} > \tau_{cs}^{l}$. Therefore, the trailing superpartials are supposed to move faster on the cube plane than the leading superpartials. Thus, the total APB width on the cube plane is assumed to eventually decrease, which in turn makes τ_{cs}^{t} even larger than τ_{cs}^{l}, and the unlocking process becomes more rapid. This results in a transformation into the planar mobile configuration as illustrated in Figure 2-7 (c).

2. If $\tau = \tau_{critical}$, in which case $\tau_{cs}^{t} = \tau_{cs}^{l}$, the two superpartials are assumed to move and cross-slip at the same rate, with resulting octahedral advance limited to the "APB jump" (Figure 2-7 (d)).

3. If $\tau < \tau_{critical}$, in which case $\tau_{cs}^{t} < \tau_{cs}^{l}$, the leading superpartial is assumed to move faster than the trailing one onto the cube plane, so that, after a few episodes of motion, w increases progressively (Figure 2-7 (e)). With the increasing of w, the driving force on the trailing superpartials becomes even smaller, and their movement on the cube plane becomes even slower. When τ_{cs}^{t} is reduced

to a value lower than the resistance on the cube plane, the screw dislocation is fully locked.

The three hypothetical conditions discussed above are based on purely mechanical analysis, and the evolution of the cross-slipped distance w is assumed to be determined by the relative cube-slip velocity of the two superpartials. Based on this analysis, the former two conditions are related with continuing deformation, while the later one ends up in a fully-locked configuration. Therefore, to sustain a continued deformation by this mechanism, the applied stress should be no smaller than $\tau_{critical}$, which is considered to be the flow strength. $\tau_{critical}$ was derived as a function of the cross-slipped distance w and material variables including fault energies and the elastic anisotropy factor. The magnitude of $\tau_{critical}$ increases monotonically with increasing values of w. Thus, the flow strength anomaly is explained by assuming that since the locking procedure is thermally activated, w should increase with increasing temperature.

Similar to the superkink models, the key parameter determining the temperature-dependence of yield strength, w (l in superkink model), was not specifically derived and left as an adjustable parameter. Thus, the self-unlocking mechanism is not a true quantitative model, either. According to the self-unlocking mechanism, the minimum value of the critical stress (with $w = b/2$) for Ni_3Al (using $\gamma_c = 0.144Jm^{-2}$ and $\gamma_o = 0.18Jm^{-2}$) is calculated to be $\sim 185MPa$. However, in the low-temperature part of the yield anomalous region, the resolved shear stress (for Ni_3Al) is less than this minimum value, which means the self-unlocking mechanism can not be applied as an exclusive explanation. Especially, for uniaxial stress in the $[\bar{1}11]$ orientation, with maximum Schmid factor equal to 0.27 on the octahedral planes, even for the case of peak uniaxial yield strength (around 700MPa at 700K), the resolved strength is still barely equal to this minimum value required to activate the self-unlocking mechanism. If we consider that at such an elevated temperature, w should be larger than $b/2$, then $\tau_{critical}$ is also increased, so the self-unlocking mechanism is unlikely to be activated.

2.2.2 Dynamic simulations

All steady-state models focus on essential features of yielding (e.g., temperature-dependence, non-Schmid effects, and the strain-rate sensitivity) without addressing the hardening properties. The predicted isothermal stress-strain curves are thus "flat" after the yield point. In order to overcome this severe limitation of steady-state models, the approach of dynamic simulation has emerged as required. Some research groups, aided by the rapid development of computer calculation capabilities, have tried to study macro-behaviors via the simulation of the dynamical evolution of micro-structures. Despite the fact that results of these dynamical simulations are usually qualitative, they help in the understanding of strength (or hardening) anomaly related mechanisms, and thus provide guidelines for further study.

The representative dynamics studies were carried out by Mills and Chrzan [43] and Veyssiere and Saada's group [44, 45]. The framework of such dynamical simulations is:

1. Define simulation elements to describe dislocations;
2. Choose and apply kinetic laws to the elements;
3. Choose and apply the pinning (locking) law and the unpinning (unlocking) law to the elements;
4. Calculate the evolution of the system, under specified loading conditions.

In Mills and Chrzan's [43] 2-D dislocation dynamics simulation, each dislocation was divided into several segments. A probability of pinning, p, was calculated as the product of a geometrical part, p_g, and a thermal part, p_t, and was assigned to the end points of each segment. The geometrical probability was highest for the screw-orientation, and the thermal probability was taken from the PPV model. The unpinning process was purely mechanical. A pinned point was dissolved when the adjacent free segment tangent bowed under stress to a critical angle ($\theta_c = 30°$ in the simulation) with respect to its pinned neighbor. When a segment was unpinned and free, its velocity was linearly related to the applied effective stress. Two types of qualitative simulations were conducted under constant applied stress conditions: one focused on the movement of a complete dislocation loop, while the other treated a finite-length dislocation segment of near-screw orientation. The major simulation results and conclusions are:

1. Near-screw parts of the dislocation loop are highly-pinned. The propagation of screws is governed by the lateral motion of superkinks, and the mobility of a superkink is related to its height.
2. Statistical study shows that the superkink number distribution is exponentially related to the inverse of superkink height, and the average value of superkink height is found to decrease with increasing temperature, consistent with experimental observations [11].
3. Exhaustion of the mobile screw density is the proposed mechanism for both the yield anomaly and the work hardening.
4. The strain-rate independence of yield strength is due to a great change in mobile dislocation density corresponding to the change in applied strain-rate.

The first property is easy to understand since a high locking probability was assigned to screw (or near screw) segments.

The exponential form distribution of superkink can be understood in the following way: when a screw segment moves within an octahedral plane, it can be locked with the assigned probability of $p = p_g \times p_t$ at each step, and a superkink of height $l = n\Delta l$ implies that the adjacent screw segment has not become pinned until it has advanced n-steps (Δl is the advance distance for each step, projected onto the octahedral plane). Thus, the probability of having a superkink of height, l, is $P(l) = p(1-p)^{n-1}$, which can also be rewritten into an exponential form as $P(l) = P_0 e^{-l/l_0}$, with $l_0 = -\Delta l / ln(1-p)$. (This idea has been modified and implemented in the proposed model to obtain an initial superkink distribution; details will be given in Chapter 3). Since $p = p_t \times p_g$, in which the thermal part p_t increases with increasing temperature, the average superkink height should decrease with increasing temperature, as observed.

Mills and Chrzan's simulations were carried out under constant applied stress (creep) condition. As mentioned previously, unlocking was assumed to happen when a critical angle θ_c is reached. Based on this critical angle θ_c, the line tension force and the applied stress τ_{app}, a critical superkink height l_c has been derived as $l_c = \frac{2\mu b}{\tau_{app}} \sin(\theta_c)$. Exhaustion of screw dislocations was observed when the superkinks on them all become too short (shorter than l_c) to move at that level of stress. Thus, the hardening mechanism was proposed as follows: in a constant applied strain-rate condition, applied stress must continuously increase as l_c drops in order to balance the exhaustion of mobile dislocations.

The small strain-rate dependence of yield strength was also roughly mentioned in the model, and was proposed to be due to the change of mobile dislocation density. They argued that, since the superkink distribution was in an exponential form, a small change in l_c, corresponding to the small change of stress level, would cause a large difference in the mobile dislocation density. But if we examine this assumption more carefully, we will find that to make the above statement valid, the exponential curve has to be very steep (or in other words, l_0 has to be extremely small). For example, if we want to keep the yield difference under 1% with a 10-times strain-rate jump, as generally observed in the experiments, l_0 has to be of the order of b or even less, which is inconsistent with both the Mills and Chrzan's simulation results, and the experimental observation by Couret [11].

Following Mills and Chrzan's idea, 2-D dynamical simulation was also carried out by the research group of Veyssiere, *et al.* [44, 45]. Screws were assumed to be locked in K-W configuration. Both superkink unlocking and the self-unlocking mechanisms were taken into consideration. The simulation was carried out in the condition of constant applied strain-rate. For each unlocked segment, the velocity is given as:

$$V(t) = \frac{\tau(t) b}{B}, \tag{2.12}$$

where $\tau(t)$ is the effective stress at time t, and B is a constant resistance. On substitution of the above equation into the Orowan equation, we can obtain the plastic strain-rate at each time step. Since the applied strain-rate is constant, the applied stress is modified at each step by:

$$\delta\tau_{app}(t) = C(\dot{\gamma}_{app} - \dot{\gamma}_{plastic})\delta t, \tag{2.13}$$

where C represents the relevant elastic modulus. Thus, the stress-strain relation is obtained. Simulations were carried out within the temperature range between 200 to 600K, and various sets of parameters were applied at each temperature to understand their influence on the overall stress-strain curve. The main results are listed as follows:

1. Two different temperature regions may be distinguished according to the dislocation dynamics. At low temperatures (200-400K), bypass of the superkinks is the dominant way to unlock K-W locks. Since the drag force on the ends of the a kink are considered as constant, the mobility of kinks is directly related to its length, and the motion of largest kinks provides most of the strain. At higher temperature, when only a limited number of superkinks are long enough to overcome the K-W locks, the direct unlocking mechanism of the incomplete K-W locks begins to dominate.
2. As for the strength anomaly, the authors point out that the simulation will present an anomalous yield behavior only if the K-W locks are strong enough, either when the jog mobility is restricted or the incomplete K-W locks are not so easily overcome.
3. Since the mobility of superkinks is closely related with their heights, superkink coalescence is essential in determining the dynamical evolution of the microstructure.

Veyssiere's simulation may be the first to combine the two unlocking mechanisms together. Two critical stresses were introduced: one is for the activation of superkinks from the resistance of the jogs at the ends of each superkink; the other one is the critical stress to activate the self-unlocking mechanism, which is determined by the temperature-dependent cross-slipped APB width. The conclusion that these two critical stresses are important in simulating the yield anomaly actually verifies that the increase in cross-slip frequency with increasing temperature itself is not enough for the expected yield anomaly (as we discussed above for the "point obstacle" models), and another temperature-dependent parameter (l or/and w) has to be included.

Superkink coalescence was observed in the dynamic simulation and was considered to be very important for superkink-unlocking mechanism. In the 2-D simulation, the coalescence of two superkinks is simplified by combining the encountering two superkinks into a new one having the height of either the sum or the difference of the original two. The real case is much more complicated than the 2-D simulation, because these superkinks may not be in the same octahedral plane. Even if we assume a 2-D planar configuration, considering the numerous different possibilities for the encounter of two superkinks (different height, different sign), it may still be too complicated to simplify and model. Thus, we neglect the superkink coalescence in the proposed superkink unlocking mechanism.

2.2.3 Hardening models

Cuitiño and Ortiz [46] tried to account for strain hardening in $L1_2$ crystals by invoking a forest-type hardening mechanism. They claimed that the yield anomaly was actually the manifestation of hardening, since the anomalous yielding only happened when a small, but finite offset strain is considered (Figure 1-7). Explicit expressions for the hardening rate of both the cube and the octahedral slip systems were developed, with both systems having the form

$$\dot{\gamma}^{\alpha} = \begin{cases} \dot{\gamma}_0^{\alpha}[(\frac{\tau^{\alpha}}{g^{\alpha}})^{1/m} - 1] & \text{if } \tau^{\alpha} > g^{\alpha}; \\ 0 & \text{otherwise.} \end{cases}$$

Here m is the strain-rate sensitivity exponent, $\dot{\gamma}_0^{\alpha}$ is a reference shear strain-rate, τ^{α} is the resolved shear stress, and g^{α} is the resistance.

The evolution equation proposed for g^{α} was taken to be a function of an assumed point obstacle density. For the cube slip systems, the change of g^{α} (due to the change in the point obstacle density), was considered to be influenced only by forest dislocation multiplication, which was assumed to be linearly related to the dislocation density of other piercing slip systems. For the octahedral systems, local cross-slip-caused pinning was also taken into consideration in the expression for g^{α}. The cross-slip mechanism of the PPV model was implemented, and the pinning obstacle density was determined by the temperature-dependent cross-slip frequency. The simulation results demonstrated anomalous yield strength and hardening rate, due to the increase of g^{α} by the accelerated cross-slip at enhanced temperatures.

However, since the hardening and yielding were rooted in the same mechanism, the predicted temperatures of maximum strength and of maximum hardening rate were the same. The difference in peak temperatures for hardening and yielding in Cuitiño and Ortiz's paper was due to the measurement of different plastic strain offsets, as shown in Figure 2-8. Moreover, the basic assumptions of point-obstacle locking are inconsistent with the TEM observations, and it is also argued that observed hardening rates as large as $\mu/10$, where μ is the shear modulus, can not be interpreted by forest hardening (with a typical hardening rate of $\mu/100$ for multi-slip and $\mu/1000$ for single-slip in fcc material).

In recent years, the research group of Martin, *et al.* has been very active in studying the deformation mechanisms of $L1_2$ crystals. They found that the work hardening rate (h) and the exhaustion rate of mobile dislocation density ($\Delta\rho_m/\rho_{m0}$), measured at the same plastic strain by a series of repeated transient creep/relaxation tests, exhibit very similar trends if plotted vs. applied stress or vs. temperature (Figure 2-9) [47]. Therefore, they assert that hardening is due to the exhaustion of the mobile dislocation density, because h and $\frac{\Delta\rho_m}{\rho_{mo}}$ share similar temperature dependence, including the exact same peak temperature. In particular, they propose an explanation as to why the temperature of the maximum hardening rate is always lower than that of the maximum yield strength by combining their idea (exhaustion of mobile dislocation density) with the self-unlocking mechanism proposed by Caillard. The idea is illustrated schematically in Figure 2-10. Since the cross-slip-based locking is a thermally activated process, at higher temperatures, screws are locked more frequently, and the exhaustion rate of mobile screw dislocations is thus higher. That is why the initial slopes of the stress-(plastic) strain curves Figure 2-10 (a) increase with increasing temperature. As the applied stress reaches a critical value, K-W locks (starting from the weakest ones with the shortest cross-slipped width on the cube plane) begin to be self-unlocked and contribute positively to the mobile dislocation density, leading to a decrease of the slope (the hardening rate). Thus, as shown in Figure 2-10 (b) and (c), there is a peak for the hardening rate curve in the temperature range where the (offset) yield strength is still monotonically increasing. Martin, *et al.*, further supported their idea by pointing out that the resolved shear stress at the temperature corresponding to the maximum hardening rate varies with octahedral plane APB energy γ_o, in a way very close to the estimated critical unlocking stress (corresponding to the weakest K-W locks) calculated according to the Caillard model (Figure 2-11).

Martin, *et al.*, also carried out several experimental works on the composition-dependence of dilutely-alloyed Ni_3Al, and tried to determine the influence of fault energies on the mechanical properties. They (Viguier and co-workers [48]) found that materials with higher complex stacking fault energy, γ_{CSF}, show higher yield strengths and lower temperatures of peak yield strength, $T_{p,\sigma}$, as shown in Figure 2-12. The former phenomenon is explained as: with all others factors (e.g., temperature and stress state) equal, the cores of leading superpartials in a compound with higher values of γ_{CSF} are intrinsically more constricted, leading at any magnitude of applied stress to a higher frequency of cross-slip and mobile dislocation exhaustion rate. The latter one is because, on one hand, due to the reason we just analyzed, at the same temperature, the yield strength of crystals with a higher value of γ_{CSF} is higher, and so is the resolved shear stress component on the cube planes. On the other hand, the higher the γ_{CSF}, the closer the Shockley partials. And a closer core is assumed to lead to a correspondingly lower friction force on the cube plane. Thus, cube systems in the compounds with higher γ_{CSF} are easier to be activated at relatively low temperatures.

Martin, *et al.*, proposed a quantitative model to explain the hardening in the $L1_2$ compounds and performed extensive experimental work to support their model. There remain several issues which need more careful consideration:

1. First of all, the exhaustion rate of the mobile dislocation density plotted in Figure 2-10, which is the strongest proof for the whole model, was derived from experimental data of a series of transient relaxation/creep tests, under a number of assumptions.

2. Secondly, even assuming that the mobile dislocation exhaustion data of $\frac{\Delta\rho_m}{\rho_{mo}}$ was correctly obtained from the transient tests, it is not clear why the same dislocation exhaustion processes occur in constant strain-rate tension/compression simulations.

2.3 General conclusions

We have summarized the most representative models in this chapter with discussions. It seems that though considerable amounts of experimental and theoretical effort have been devoted to the study of $L1_2$ crystal for decades, some of the underlying mechanisms that dominate the overall mechanical properties and behaviors still remain unclear, and none of the existing models can provide a quantitative and comprehensive description of this problem.

It is commonly understood now that the anomalous behaviors of $L1_2$ crystals are dominated by the non-planar movement of screw dislocations on the octahedral planes. Some physically-oriented models have been put forward, based on different assumed mechanisms of the formation and the unlocking of K-W locks. However, most of them are steady-state models, focusing on the anomalous temperature-dependence of yield strength. Generally, these models present quantitative expressions for the yield strength, however the anomalous temperature-dependence of the yield strength has to be established through certain assumptions on temperature-dependence of some internal variables (e.g., the superkink height and the cross-slipped distance on the cube plane), which are not explicitly provided. Similarly, no quantitative mechanism-based hardening models have been proposed. Furthermore, the complexity of this problem is much more than just anomalous temperature-dependence of yield strength and strain hardening rate. Great challenges exist in fully understanding and systematically explaining other mechanical properties, including the orientation-dependence and the small strain-rate dependence of yielding and hardening, the tension-compression asymmetry of yield strength, the reversibility of yield strength, the fault energy effects and the difference in the temperatures corresponding to peak yield strength and peak hardening rate.

In the next chapter, we propose a single-crystal constitutive model, based on the current understanding of the underlying micro-mechanisms in $L1_2$ compounds. Strain hardening mechanisms are also presented, derived from the evolution of the same internal variables that dominate the yield properties. The initial state and the evolution of these internal variables are quantitatively illustrated, and systematical simulations have been carried out. The simulation results (e.g. the predicted stress-strain relations, the evolution of critical initial variables and parameter sensitivity studies) provide a great deal of information to examine and understand the proposed model as well as the underlying mechanisms.

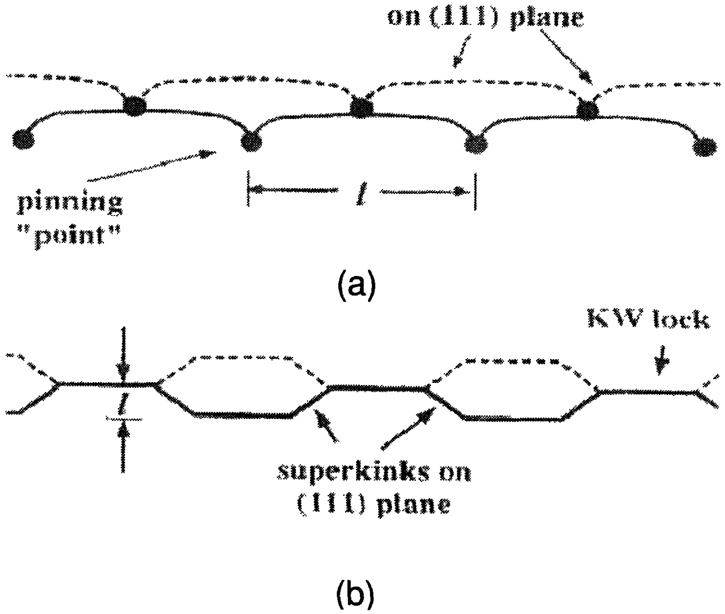

Figure 2-1: Schematic illustration of the successive positions for a dislocation on the (111) plane by (a) bowing between pinning points and (b) by the lateral motion of superkinks [14].

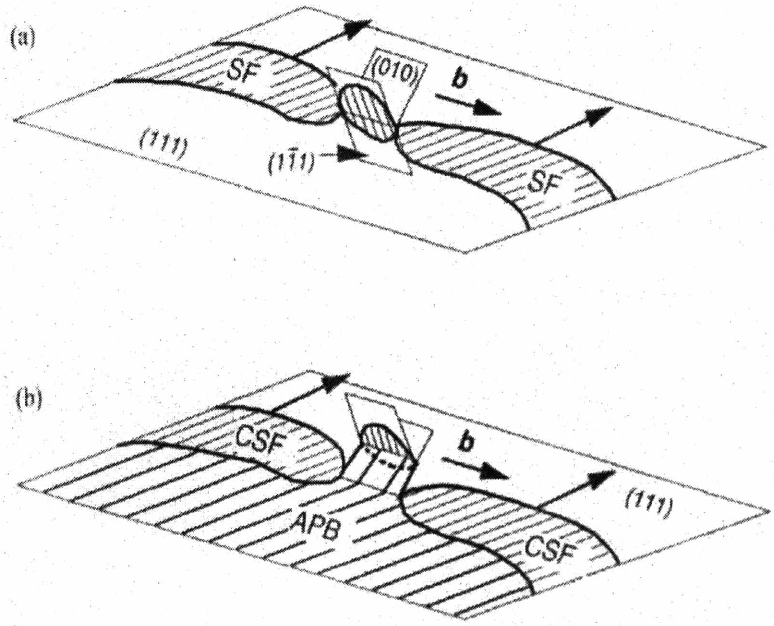

Figure 2-2: Cross-slip processes of screw dislocations: (a) The Friedel-Escaig mechanism in fcc crystals; (b) PPV model in $L1_2$ crystal [34].

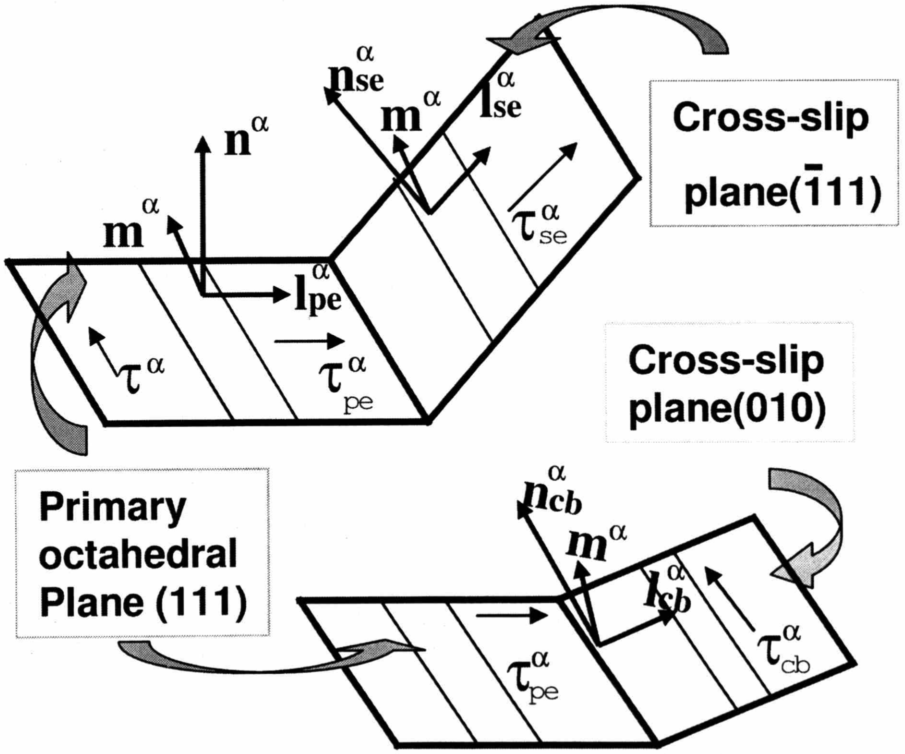

Figure 2-3: Schematic illustration of the non-Schmid stress components, including cross-slip cube and octahedral planes intersecting a primary octahedral plane.

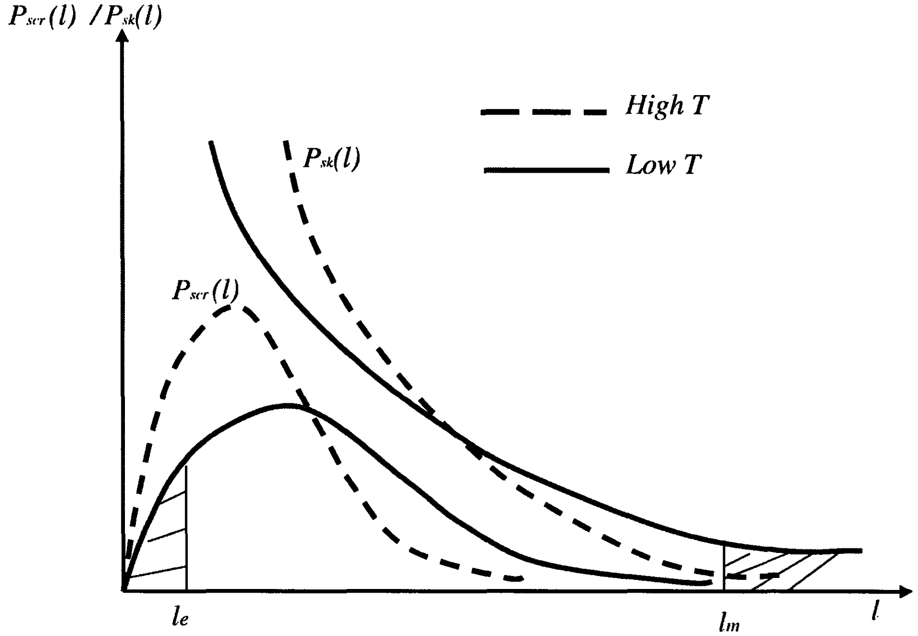

Figure 2-4: Illustration of the ELU model. As the temperature increases, both distributions (P_{scr} and P_{sk}) shift to the left. To rebalance the multiplication rate and the exhaustion rate, which are proportional to the two shaded areas, respectively, both l_e and l_m need to decrease. Since l_e and l_m are found to be inversely related with the applied stress, an anomalous temperature-dependence of yield strength is expected.

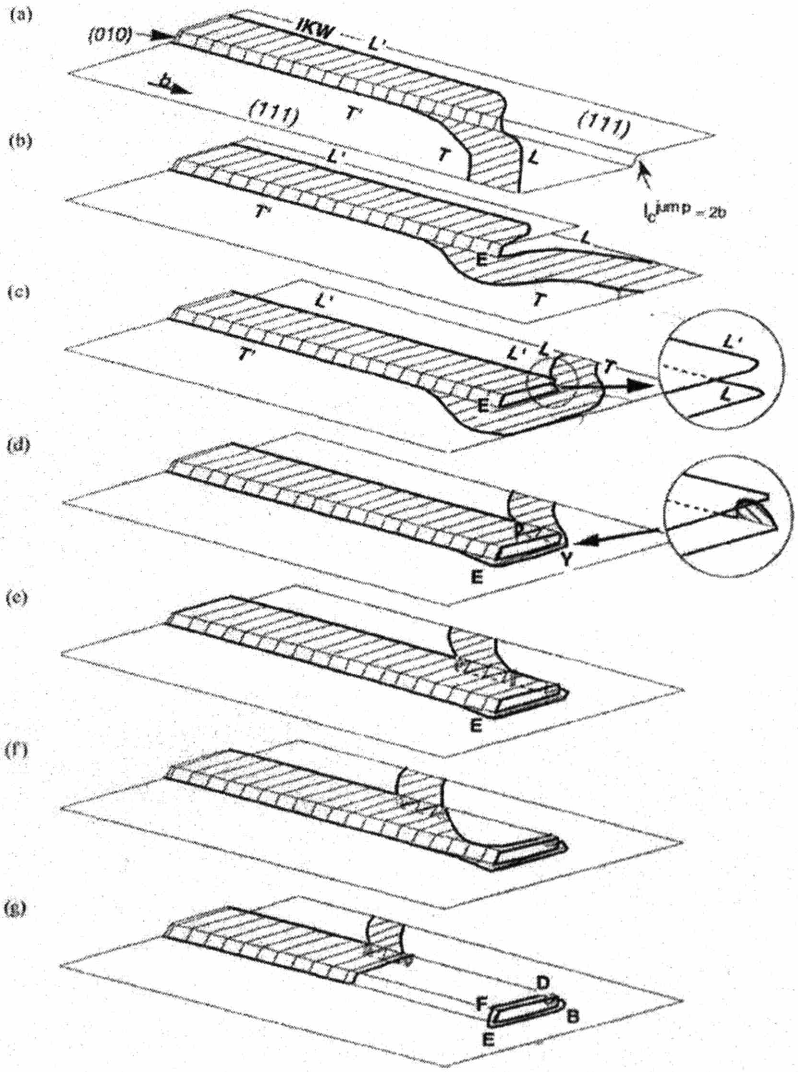

Figure 2-5: 3-D illustration of Hirsch superkink bypassing mechanism [34]. (a) the incomplete K-W lock configuration; (b)-(c) formation of edge dipoles at the ends of the locked screw segments; (d) a thermally activated cross-slip step brings the superkink to the upper (111) plane; (e)-(g) the IKW is unlocked by the bypassing of superkink and the formation of an APB tube.

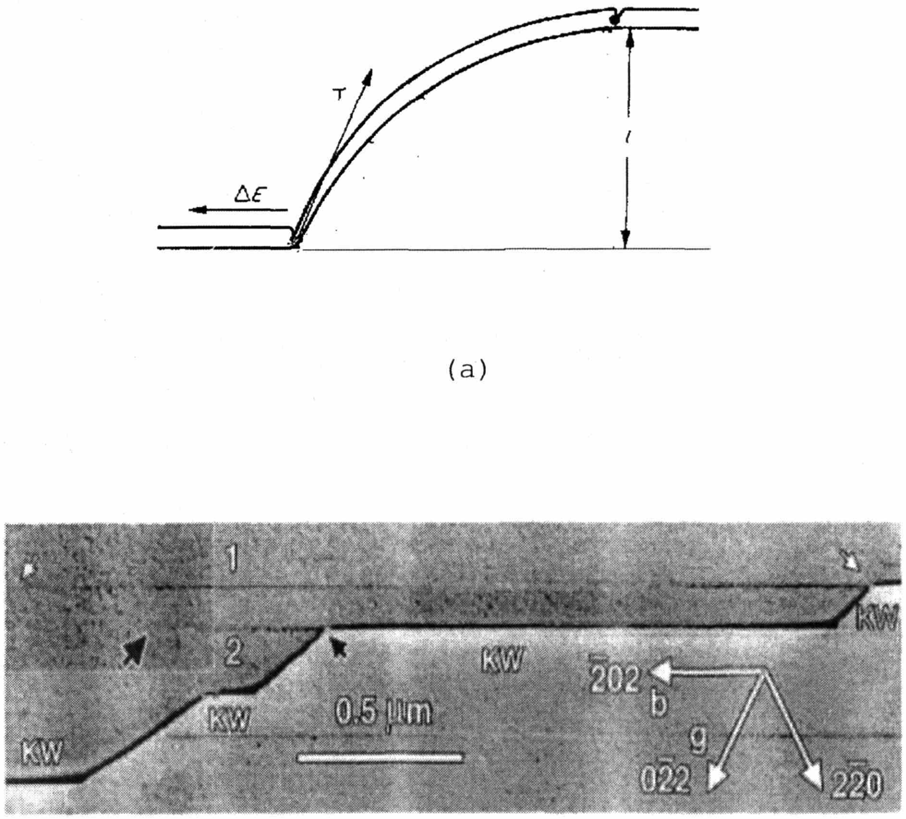

(a)

(b)

Figure 2-6: (a) 2-D illustration of a superkink moving left along the locked screw segment; (b) TEM observation of K-W locks and superkinks on an octahedral plane. APB tubes are attached at the end of the superkinks [41].

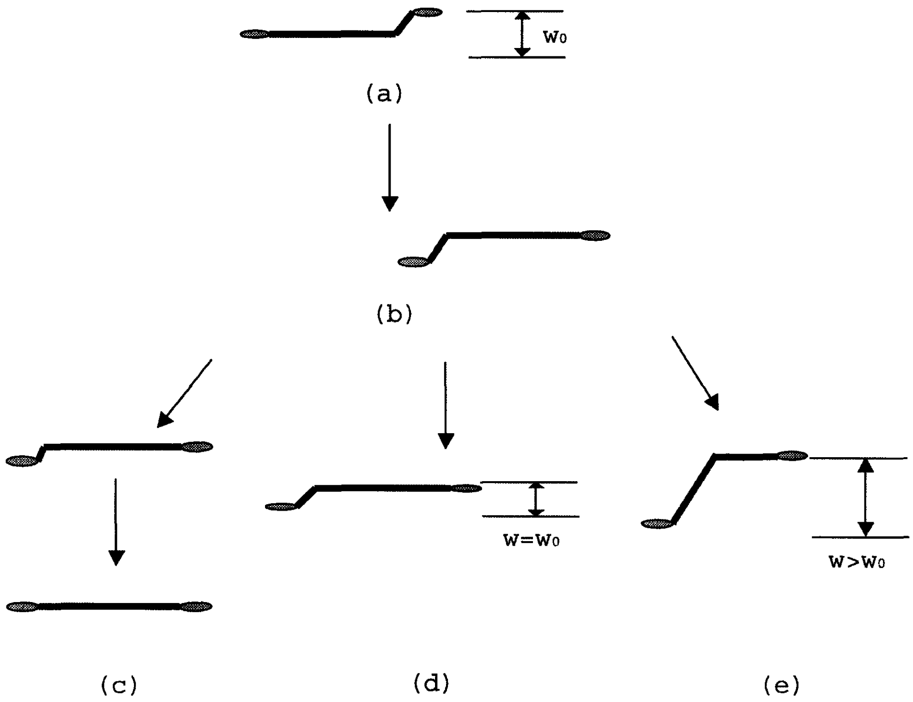

Figure 2-7: Schematic illustration of the three different cases in the evolution of IKW locks: (a) the mobile configuration after the cross-slip (by a distance of w_0) of the leading superpartial; (b) the successive locked configuration when the trailing superpartial meets the cross-slipped cube plane; (c-e) depict asymptotic states for the segment after a sufficient number of unlock/glide/re-cross-slip events [42], depending on magnitude of applied octahedral shear stress.

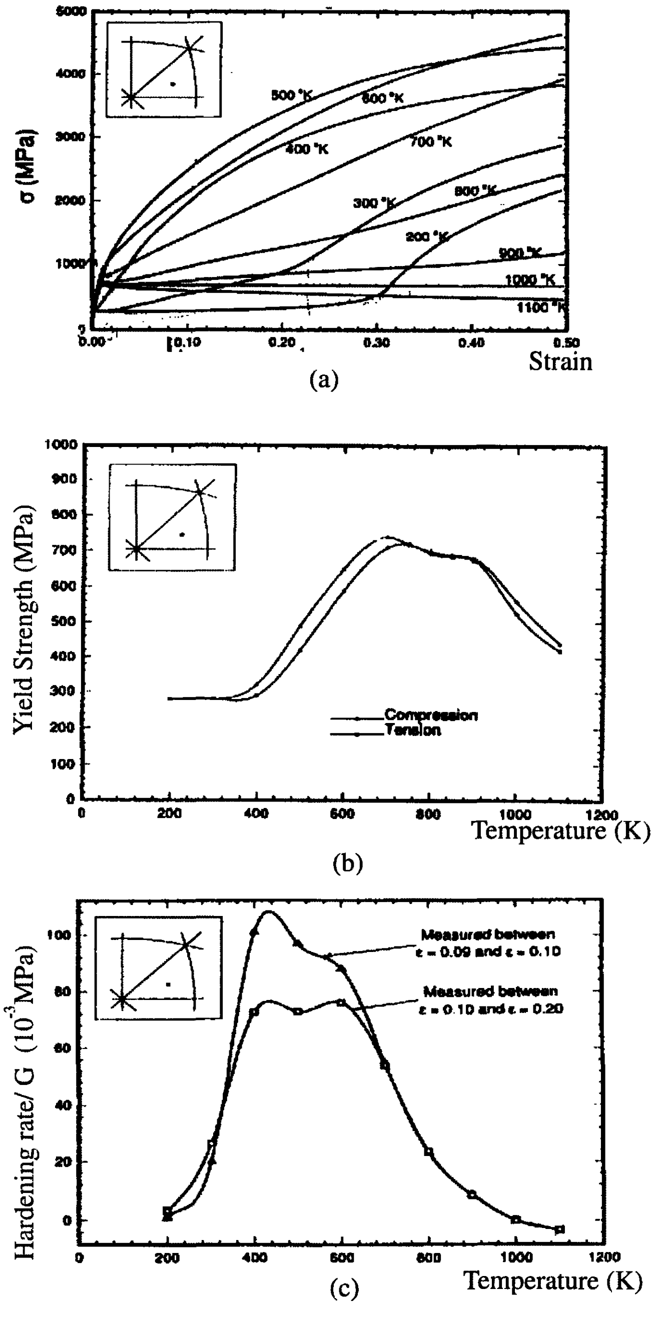

Figure 2-8: Simulation results [46]: (a) Stress-strain curves for different temperatures; (b) Temperature-dependence of yield strength at 0.2% offset strain in both tension and compression; (c) Temperature-dependence of hardening rate of two different strain regions.

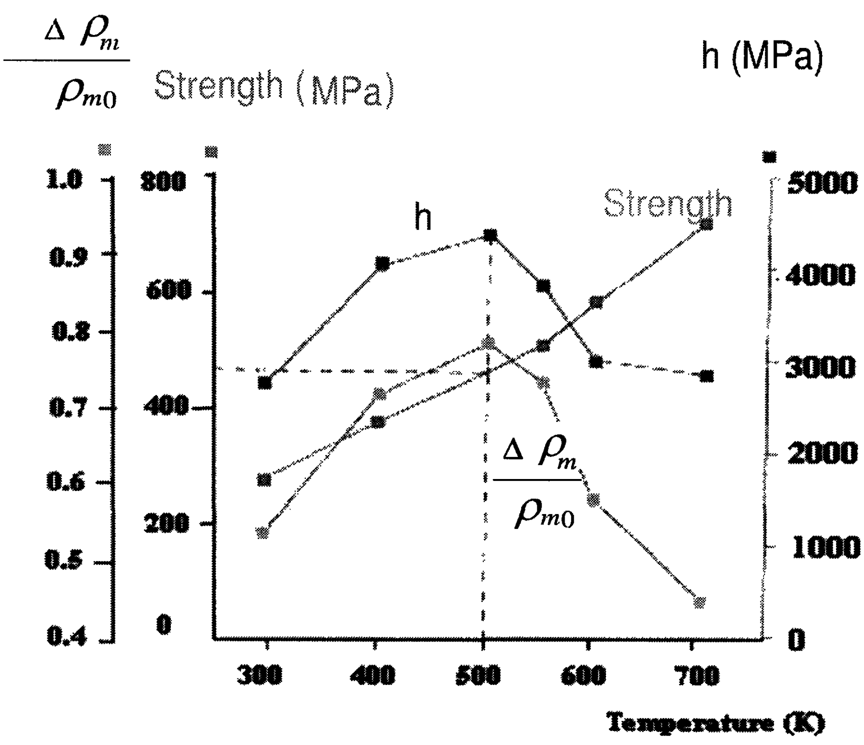

Figure 2-9: The exhaustion rate of mobile dislocation density and the work hardening rate vary in a similar way with temperature. Temperature of peak hardening coincides with that of peak exhaustion of mobile dislocation density [47].

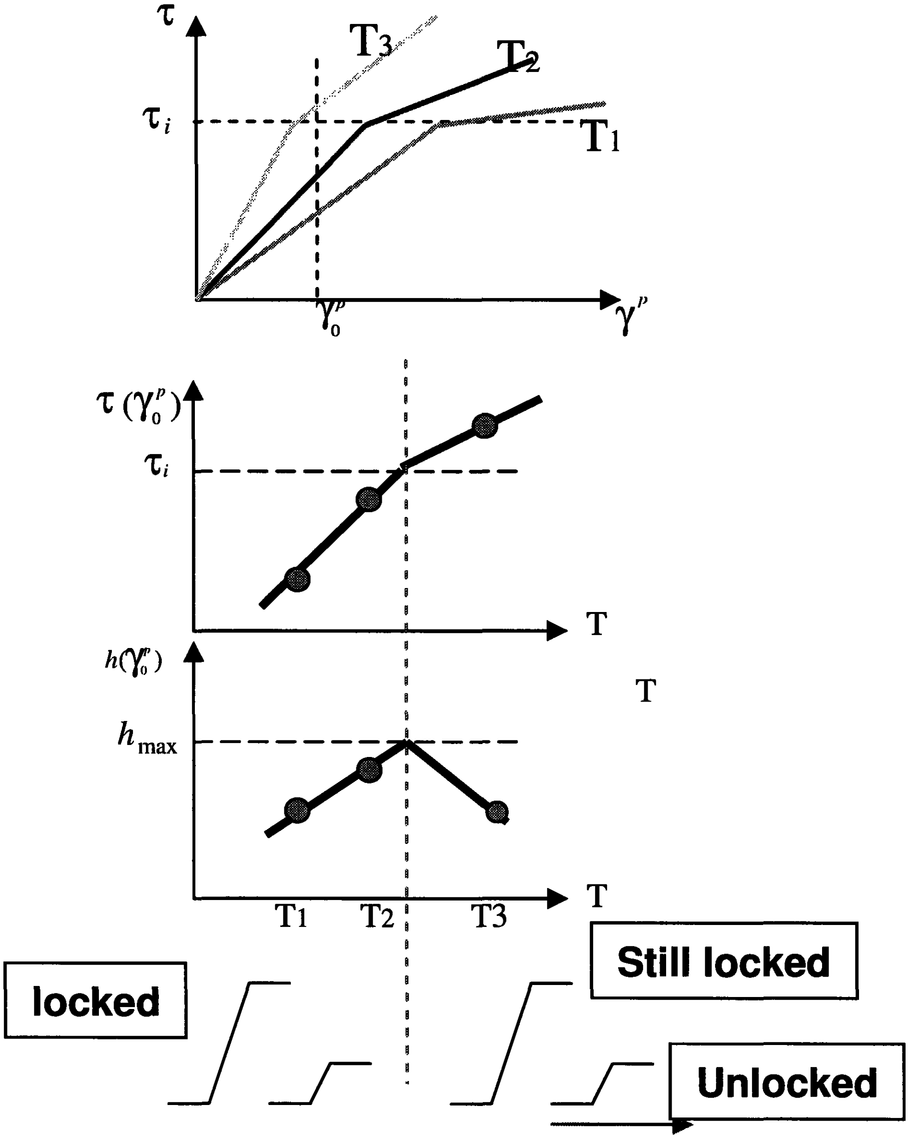

Figure 2-10: Schematic illustration rationalizing the existence of a peak temperature of work-hardening rate in the yield anomaly region: (a) Stress-(plastic) strain curves at three temperatures, with two hardening stages; (b) Stress at given plastic strain increases monotonically with increasing temperature. (c) In the same temperature range, the work-hardening slope presents a temperature peak [47].

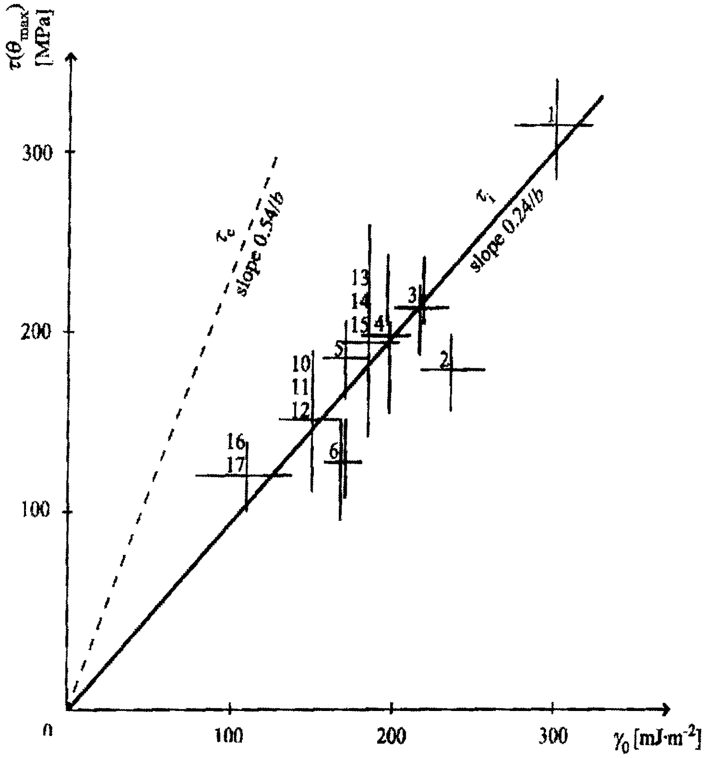

Figure 2-11: Resolved shear stress corresponding to the maximum in work-hardening in a range of alloy compositions, plotted as a function of APB energy on (111) [47]. The solid line along which the data points cluster corresponds to the dependence of critical self-unlocking stress on γ_0.

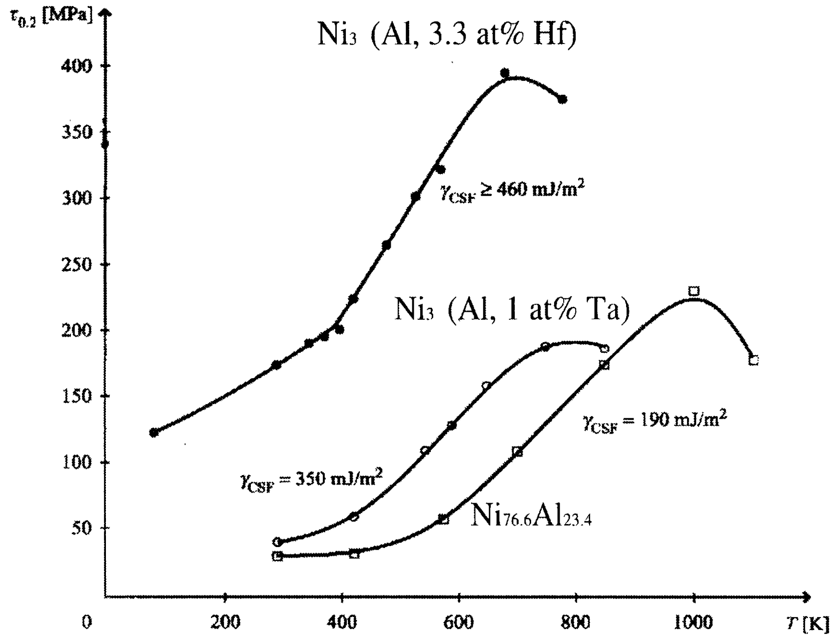

Figure 2-12: Illustration of the γ_{CSF}-dependence of yield strength [46]. Crystals with larger γ_{CSF} show a higher yield strength and lower $T_{p,\sigma}$.

Chapter 3

Mechanism-based modeling of single-crystal $L1_2$ intermetallic compounds

3.1 Framework of the Single-crystal Plasticity Model

As summarized in Chapter 2, much work has been done to reveal the underlying mechanisms that dominate the mechanical behaviors of $L1_2$ single crystals, especially the mechanisms governing the anomalous yield and hardening properties. For orientations other than those close to [001], it is well understood that the change of the temperature-dependence of uniaxial yield strength from 'abnormal' to 'normal' is due to the change of dominant slip-systems from octahedral planes to the cube planes. Therefore, in the proposed model, both octahedral and cube slip-systems are included.

The only active slip direction in the $L1_2$-order single crystal is the close-packed $< 101 >$ orientation, except at very high temperatures (substantial numbers of $< 100 >$ dislocations were found in $Ni_3(Al, Ti)$ deformed at 1200 K [49]). In the anomalous yield region, plastic deformation is mainly contributed by the slow and jerky movement of long screw dislocations on the octahedral planes. Thus, a total of twelve distinct ($\{111\} < 110 >$) slip-systems have been chosen as potentially activated slip-systems.

The jerky movement of screws in the anomalous yield regime is considered as a sequence of successive locking-unlocking processes. Locking is due to thermally activated cross-slip from octahedral planes to cube planes, which is driven by both the reduction of APB energy and the torque forces introduced by elastic anisotropy.

For the unlocking part, as we have discussed in the last chapter, both the superkink unlocking and the self-unlocking mechanisms are very physically-oriented and supported by many experimental observations. Besides, the change of the temperature-dependence of the strain hardening rate in the anomalous yielding region suggests that there is more than one underlying unlocking mechanism. Therefore, in the proposed model, both the superkink unlocking and the self-unlocking mechanisms have been modified and implemented.

In the low-temperature part of the yield anomaly region, screws are considered to be unlocked by the bypassing of the longest superkinks on them. The self-unlocking mechanism does not contribute to the total plastic strain because the resolved shear stress is lower than the critical value corresponding to self-unlocking of the weakest incomplete K-W locks. Hardening in this regime is due to the decrease of the longest superkink height with continuing plastic deformation, and the hardening rate increases monotonically with increasing temperature. In the high-temperature part of the yield anomaly region, the stress level has been raised high enough to activate the self-unlocking mechanism. With increasing temperature, more and more screws which can not be unlocked by the superkink mechanism, due to the lack of sufficiently long superkinks, can now be self-unlocked. Thus a negative temperature-dependence of hardening rate is expected, even though offset yield strength continues to increase with temperature. In the proposed model, superkink unlocking and self-unlocking are introduced as two relatively independent mechanisms; detailed discussions will be presented in Chapter 5.

Above the temperature of peak yield strength, $T_{p,\sigma}$, where cube slip dominates, the screw and edge dislocation densities were observed to be comparable (Figure 1-15).

The movements of dislocations (both screw and edge) are found to be slow and planar. Detailed mechanisms of dislocation dynamics for cube slip are still unclear and are not the focus of the current research. Therefore, we simply include six $\{001\} < 110 >$ cube slip-systems modeled with standard power-law form to capture the 'normal' part of temperature dependence of yield strength. The cube-slip resistance is assumed to decrease linearly with increasing temperature. Thus, with increasing temperature and stress, the cube slips will gradually but increasingly contribute to the total plastic deformation, until they are fully dominant.

For uniaxial stress in the [001] orientation, since the Schmid factor is zero for the cube planes, octahedral slips always dominate. Stress-drops after initial yielding have been experimentally observed in uniaxial compression tests, at very high temperatures and with relatively low applied strain-rate. The offset yield strength measured after the stress-drop shows a 'normal' temperature-dependence. In order to capture the mechanical properties of the [001] deformation at high temperatures, a proposed diffusion mechanism is implemented.

The model framework is schematically illustrated in Figure 3-1, and Tables 3-1 and 3-2 list all the 18 potential slip-systems used in the proposed model and simulations.

3.2 Octahedral-slip

3.2.1 Revised superkink unlocking model

We have reviewed superkink-unlocking models in Chapter 2. Generally, these models share the following common assumptions:

1. Locked screw dislocations are unlocked by the bypassing of predominantly edge-orientated superkinks;
2. Longer superkinks are supposed to have higher mobility, and the yield strength is inversely related to superkink height;
3. An initial distribution of superkinks or a characteristic length of superkinks

(for example, $\bar{l}$) , from which the yield strength is derived, is presumed fully-established as a precursor to explaining the subsequent plastic deformation.

4. The yield anomaly is due to an assumed systematic shortening of superkink height with increasing temperature.

In the proposed superkink model, we adopt the basic ideas about superkink mechanisms. Additionally, two major modifications have been made. Firstly, an explicit temperature-dependence of the initial dislocation superkink distribution is derived, adding quantitative structure to the proposed model. Secondly, an evolution mechanism for the dislocation distribution has been proposed, in order to capture the hardening properties.

"Initial" superkink distribution

We assume that most of the screw dislocations are locked by thermally-activated cross-slip during the early (microstrain) expansion of dislocation loops. Superkinks with different height are generated by the same procedure. This superkink distribution is then considered as an "initial" condition in the proposed superkink-unlocking model. In Chapter 2, we reviewed the computer simulation carried out by Mills and Chrzan, and discussed the relation between the superkink distribution and the thermally activated locking procedure of screw dislocations. Here, we derive the "initial" superkink distribution in a similar way.

As illustrated by Figure 3-2 (a), when a screw segment (with some characteristic length) moves within an octahedral plane, it can be locked by cross-slipping onto the nearest cube plane, with the probability of $P(l = a) = p$, or, if it does not cross-slip, it can continue to move on and cross-slip on the next-nearest cube plane, with the probability of $P(l = 2a) = p(1 - p)$, and so on. Here, l is the distance the screw segment has advanced on the octahedral plane before it cross-slips onto the cube plane, which is also the height of the superkink generated in the procedure. The parameter $a = \sqrt{3}b$ is the distance between the two adjacent cube planes (cube I and II in Figure 3-2 (b)) on the octahedral plane, with b the magnitude of the

Burgers vector of the superpartials. The general form for the probability of forming a superkink with a height of $l = na$ is then given as:

$$P(l = na) = p(1-p)^{(n-1)} = \frac{p}{1-p}(1-p)^{(l/a)}. \tag{3.1}$$

The above expression assumes that at each step, the cross-slip probability is the same. However, the bowing screw segment should become less and less screw-orientated as it moves forwards. Thus, Eqn. 3.1 is modified by a factor q ($q < 1$), as:

$$P(l = na) = \frac{p}{q(1-p)}[q(1-p)]^{(l/a)}. \tag{3.2}$$

Eqn. 3.2 can be rearranged into the logarithm-form:

$$ln[P(l = na)] = ln\left(\frac{p}{q(1-p)}\right) - \frac{l}{(-a/ln[q(1-p)])}. \tag{3.3}$$

The distribution function, $P(l)$, is schematically illustrated in Figure 3-3, with both the normal-form (Eqn. 3.2) and the logarithm-form (Eqn. 3.3).

The basic cross-slip probability p, in Eqns. 3.1-3.3, is taken to be:

$$p^{\alpha} = \exp(-\frac{H_0}{kT})\exp(c_{pe}S^{\alpha}_{pe}), \tag{3.4}$$

where the superscript α represents a particular slip-system. The first factor on the right hand side of Eqn. 3.4 shows that cross-slip is a thermally activated process, and the locking enthalpy H_0 is set as a constant of $0.3 \times 10^{-19} J$ in the simulations. The second term is introduced because we assume that cross-slip process is initiated by the constriction of the leading Shockley partials on the octahedral plane. The dimensionless parameter c_{pe}, which was taken as 1 in the simulation, represents the intensity of this effect. S^{α}_{pe} in the second term is the non-Schimid factor for each slip-system. In the case of uniaxial loading in the x_3-direction,

$$S^{\alpha}_{pe} = \frac{\tau^{\alpha}_{pe}}{|\sigma_{33}|}. \tag{3.5}$$

According to the PPV model, the non-Schmid stress component τ_{pe} either constricts or expands the leading Schockley partials, which in turn assists or inhibits the cross-slip of screw dislocations. The absolute operator in Eqn. 3.5 accounts for the fact that τ_{pe} changes sign when going from tension to compression. Under conditions of uniaxial-stress (tension/compression), if the loading axis (here taken as parallel to Cartesian basis vector $\mathbf{e}_3$) corresponds to a more constrictive τ_{pe}, screws of that system find it easier to cross-slip and generate shorter superkinks, and vice versa. If we derive the initial distribution strictly by simulating the movement and the cross-slip of screws, a locking enthalpy having the form $H_l = H_{l0} - V_{pe}\tau_{pe}$ should be applied. In the simulation, we instead assume that an initial distribution can be fully established "at the beginning" of plastic deformation, and the non-Schmid factor S^{α}_{pe} rather than the real value of τ^{α}_{pe} is used, in order to capture the basic idea of the assumed constriction-initialized locking process.

Eqn. 3.3 has a form similar to the number distribution of superkinks reported in the experimental work of Couret, *et al.* [11]:

$$N(l) = N_0 \, \exp(\frac{l}{l_0}) \quad \Rightarrow \quad ln(N(l)) = ln(N_0) - \frac{l}{l_0}; \tag{3.6}$$

thus we can rewrite Eqn 3.3 as

$$P^{\alpha}(l) = P_0 \, \exp(-\frac{l}{l^{\alpha}_0}), \tag{3.7}$$

with $l^{\alpha}_0 = -a/ln[q(1-p^{\alpha})]$, and $P_0 = p^{\alpha}/q(1-p^{\alpha})$. As p^{α} is defined by Eqn. 3.4, the magnitude of both the intersection term of Eqn. 3.3 (the first term in the right hand side) and the slope term $(-\frac{1}{(-a/ln[q(1-p)])})$ increase with increasing temperature, consistent with the observations in experiments [11].

In the simulations, values of l are chosen discretely from $l_{min} = b$ to the maximum value, l_{max}, with an increment of b (Actually, this is not the most computationally optimized approach, since very short superkinks can hardly be activated, and thus have no contribution to the plastic deformation). By assuming that the normalized probability of $P(l_{max})$ equals to a critical value P_{min}, l_{max} for each temperature is given as:

$$l^{\alpha}_{max} = l^{\alpha}_{0}\ ln(1 + b/l^{\alpha}_{0}P_{min}), \qquad \text{where } l^{\alpha}_{0} = -a/ln[q(1-p^{\alpha})]. \tag{3.8}$$

As shown in Figure 3-4 (a) ([123] orientation), l_{max} determined by Eqn. 3.8 monotonically decreases with increasing temperature, and is dependent on the value of P_{min}, which is taken as 10^{-4} in the simulations. Figure 3-4 (b) presents the orientation-dependence of l_{max} due to different S_{pe} values. For the compression condition, S_{pe} corresponding to the active slip-system for [001], [123], and [$\bar{1}$11] orientations are -0.2357, 0.1347 and 0.1574, respectively.

In the simulations, screw dislocations are the strain carriers, and their mobility is assumed to be directly related to the longest superkinks on them. Thus, it is necessary to know the distribution of screws as a function of the height of the longest superkink they possess. This statistical analysis was carried out by Chrzan, *et al.* [50] in three steps: Firstly, the number of superkinks on each screw, n, is assigned as a Gaussian distribution over the population of screws:

$$S_1(n) = \frac{1}{\sqrt{2\pi\sigma_n^2}} \exp(\frac{-(n-\bar{n})^2}{2\sigma_n^2}), \tag{3.9}$$

where σ_n is the standard deviation and $\bar{n}$ is the mean value. In Chrzan's work, the superkink spacing and the length of screws were not specified. In our model, screws are simplified to have the same length, so that once they get unlocked, they are assumed to be equal strain carriers. According to the TEM observations (Figure 1-12), this is not a bad assumption.

Secondly, given that the number of superkinks on one screw is n, we need to derive the probability $S_2(l, n)$ that the longest superkink on this screw has the height of l. In order to do this, we first assume the probability of an individual superkink with height of l, chosen at random from all screws, is given by Eqn. 3.7. Then, the chance that a superkink drawn at random from this distribution, has a length shorter than l, is derived as:

$$W(l) = \sum_{l'=b}^{l'=l} P(l'). \tag{3.10}$$

Therefore, in considering a screw having n superkinks on it, the probability that the longest superkink on this screw has the height of l is a binomial distribution given as:

$$S_2(l,n) = C_n^1 P(l) W(l)^{n-1}, \tag{3.11}$$

where $C_n^1 = n$ is the binomial coefficient.

The probability $S_2(l,n)$ given in Eqn. 3.11 is for the case of exactly n superkinks on the screw dislocation. In the final step, we need to sum up $S_2(l,n) \times S_1(n)$ for all possible values of n, and the desired screw distribution with longest superkink of height of l is derived as:

$$\begin{aligned} P_{screw}(l) &= \int_0^\infty S_1(n) S_2(l,n) dn & (3.12) \\ &= \int_0^\infty \frac{1}{\sqrt{2\pi\sigma_n^2}} \exp\left(\frac{-(n-\bar{n})^2}{2\sigma_n^2}\right) C_n^1 P(l) W(l)^{n-1} dn. & (3.13) \end{aligned}$$

Integrating the above equation with Maple and simplifying the result by assuming that $\sigma_n \ll \bar{n}$, we get:

$$\begin{aligned} P_{screw}(l) &= \frac{1}{2} P(l) W(l)^{(\bar{n}-1)} \exp\left(\frac{1}{2}\sigma_n^2 ln^2 W(l)\right) \\ &\times \left(erf[\frac{\sqrt{2}\sigma_n^2 lnW(l) + \bar{n}}{2\sigma_n}] + 1\right) \left(\sigma_n^2 lnW(l) + \bar{n}\right). \end{aligned}$$

With the assumption of $\sigma_n \ll \bar{n}$, the value of the error function in the above equation is close to 1. Thus, $P_{screw}(l)$ can be finally simplified as the following form (Eqn. 6 in Chrzan's paper):

$$P_{screw}(l) = \exp\left(\frac{1}{2}[\ln W(l)\sigma_n]^2\right) [lnW(l)\sigma_n^2 + \bar{n}] P(l) W(l)^{(\bar{n}-1)}. \tag{3.14}$$

If l is very small, it is very unlikely that such a short superkink can be the longest on a screw dislocation. On the other hand, if l is very large, then the population of such long superkinks is so small as to make it unlikely that the longest superkink on a randomly chosen screw is this large. Thus, $P_{screw}(l)$ is a bell-shaped function. Figures 3-5 and 3-6 illustrate that the distribution of $P_{screw}(l)$ differs significantly with different values of $\bar{n}$, but it is insensitive to the change of σ_n. The assumption $\sigma_n \ll \bar{n}$ is made to derive a simplified form for Eqn. 3-12, and this needs further experimental support. However, this assumption does not affect the general bell-shape of the distribution $P_{screw}(l)$ and should not affect the following simulation too much. It also needs to be mentioned that, in Louchet's ELU model, a similar bell-shaped distribution of screw dislocations has been derived ($P_{scr}(l)$ as drawn in Figure 2- 4); it is a special case of P_{screw} with the assumption that there are only two superkinks on each screw dislocation.

Evolution of superkink distribution with plastic deformation

Most previous superkink models are steady-state models, keeping the characteristic superkink height (or distribution) unchanged with deformation. Therefore the stress-strain curves predicted based on these models are flat after the yield point, showing no hardening. In the proposed model, an evolution relation for the superkink distribution has been derived. As we will illustrate later, under a given stress level, only the screws possessing very long superkinks (close to the current value of l_{max}), can be unlocked. When these screws are locked again, new superkinks will be generated during the re-locking procedure, which is assumed to be the same as in the original locking process when the initial superkink distribution was formed. Thus, the newly-generated superkinks are taken to follow the same distribution $P(l)$ defined by Eqn. 3.7. Similarly, the re-locked screws should also follow the distribution of $P_{screw}(l)$, as defined by 3.13. Because $P_{screw}(l)$ is a bell-shaped function, it is very likely that longest superkinks on the re-locked screws are much shorter than their original height. Thus, with increasing plastic deformation, there are fewer and fewer screws with very long superkinks on them, and the applied stress is expected to increase, in order to activate screws with shorter superkinks and sustain continued deformation.

According to Orowan's relation, the plastic strain-rate for each slip system is given as:

$$\dot{\gamma}^{\alpha} = \rho_m^{\alpha} b v^{\alpha}, \tag{3.15}$$

where ρ_m^{α} is the mobile dislocation density for each slip system, b is the magnitude of Burgers vector, and v^{α} is the average velocity of the mobile dislocations. We assume that the unlocking process is thermally activated, as described by Hirsch, so that Orowan's relation can then be rewritten as:

$$\dot{\gamma}_1^{\alpha} = \rho_{total}^{\alpha} b \sum_{b}^{l_{max}^{\alpha}} P_{screw}^{\alpha}(l) v^{\alpha}(l, \tau^{\alpha}), \tag{3.16}$$

where ρ_{total}^{α} is the total dislocation density for each slip-system, and the velocity is given as:

$$v^{\alpha}(l, \tau^{\alpha}) = v_0^{SK} \exp\left(-\frac{H_u(l, \tau^{\alpha})}{kT}\right), \tag{3.17}$$

where v_0^{SK} is a reference velocity, and the unlocking enthalpy H_u is derived by Hirsch and is given in Eqn. 2.10 as $H_u = H_{u0}^{*} - V(l)\tau^{\alpha}$. Numerically, since the magnitude of activation volume, $V(l)$, is large and the term $V\tau^{\alpha}$ is inside an exponential operator, the yield strength is very sensitive to value of V. Therefore, since V is proportional to the superkink height l, under a given stress level, only those screws possessing long superkinks very close to the current value of l_{max} can be unlocked.

At each time step, a fraction of the screws are activated and redistributed, as schematically illustrated in Figure 3-7. Thus, P_{screw} is updated as:

$$P_{screw}(l_i; t + \Delta t) = (1 - P_{act}(l_i, \Delta t)) + P_{screw}(l_i; t) \sum_{j} P_{screw}(l_j; t) P_{act}(l_j, \Delta t), \tag{3.18}$$

where $P_{screw}(l_i; t)$ is the ith term in the discrete P_{screw}-distribution at time t, and $P_{act}(l_i, \Delta t)$ is the portion of activation (unlocking) corresponding to the ith lengthscaling bin for P_{screw}. The first term on the right hand side of Eqn. 3.18 corresponds to the unlocking-caused decrease of population for screws with longest superkink height l_i, and the second term represents the compensation from the redistribution of all the unlocked screw dislocations. Since unlocking is thermally activated, the probability of screws with the longest superkink height l_i that can be unlocked is proportional to $\exp(-H_u(l_i, \tau^\alpha)/kT)$, and is given as $P_{act}(l_i, \Delta t) = f_{atp}\exp(-H_u(l_i, \tau^\alpha)/kT)$. Here f_{apt} is an attempting frequency with a fit value of $5s^{-1}$, Δt is the time increment, and l_i is the ith term of the height distribution.

3.2.2 Revised self-unlocking model

The self-unlocking model was proposed by Caillard [42, 51] based on his *in situ* observation [12, 52] of the jerky movement of screw dislocations. Figure 3-8 shows the 2-D configuration of an incomplete K-W lock, in projection along the screw direction. θ is the inclination angle between the line connecting the two superpartials and the trace of the cube plane. w is the width of APB cross-slipped onto the cube plane. The stress components on both the leading and trailing superpartials have been indicated, but the details of the Shockley partials are neglected. In Figure 3-8, γ_c is the APB energy on the cube plane, γ_o is the APB energy on the octahedral plane, and τ_{cb} and τ are the resolved shear stress components on the cube plane and the octahedral plane, respectively. The interaction between the two superpartials is represented by the radial repulsion component τ_i, and the torque due to the tangential stress component τ_θ. According to Yoo [53], $\tau_\theta = f(\theta)\tau_i$, where

$$f(\theta) = \frac{(A-1)\sin 2\theta}{2(A\cos^2\theta + \sin^2\theta)}. \tag{3.19}$$

In Eqn 3.19, A is the Zener elastic anisotropy factor, $A \equiv 2C_{44}/(C_{11} - C_{12})$. For the leading superpartial, the projections of the force components in the octahedral plane balance each other:

$$\tau b - \gamma_o + \tau_i b\cos\alpha - \tau_\theta b\cos\beta = 0, \tag{3.20}$$

where $\alpha = 55° - \theta$ and $\beta = 35° + \theta$. The total driving force for the leading superpartials in the cube plane is:

$$b\tau_c^l = b\tau_{cb} - \gamma_c + b\tau_i \cos\theta + b\tau_\theta \sin\theta. \tag{3.21}$$

Similarly, the total driving force for the trailing superpartials in the cube plane is given as:

$$b\tau_c^t = b\tau_{cb} + \gamma_c - b\tau_i \cos\theta - b\tau_\theta \sin\theta. \tag{3.22}$$

Rearranging Eqn. 3.20, τ_i can be expressed as:

$$\tau_i = \frac{\gamma_o/b - \tau}{[\cos\alpha - f(\theta)\cos\beta]}. \tag{3.23}$$

Substituting τ_i into Eqns 3.21 and 3.22, τ_c^l and τ_c^t can be rewritten as:

$$\tau_c^l = \tau_{cb} - \gamma_c/b + \tau^* \tag{3.24}$$

$$\tau_c^t = \tau_{cb} + \gamma_c/b - \tau^*, \tag{3.25}$$

where τ^* is given as:

$$\tau^* = (\frac{\gamma_o}{b} - \tau)\frac{\cos\theta + f(\theta)\sin\theta}{\cos\alpha - f(\theta)\cos\beta}. \tag{3.26}$$

As we discussed in Chapter 2, continued octahedral slip of screws is assumed when the cube-direction driving force on the trailing superpartials is larger than that on the leading one ($\tau_c^t > \tau^l$). Thus, a critical stress, above which the self-unlocking mechanism will be activated is derived under the condition of $\tau_c^t = \tau^l$, and is expressed as:

$$\tau_{critical}(\theta) = \frac{\gamma_o}{b} - \frac{\gamma_c}{b}g(\theta), \tag{3.27}$$

where $g(\theta)$ is:

$$g(\theta) = \frac{\cos\alpha(\theta) - f(\theta)\cos\beta(\theta)}{\cos\theta + f(\theta)\sin\theta}. \tag{3.28}$$

Functions $f(\theta)$ and $g(\theta)$ are plotted in Figure 3-9 with the Zener factor $A = 3.3$, which is a typical value for Ni_3Al [58].

This critical unlocking stress was also derived by Caillard [42], but the interaction force between the two superpartials in his paper was derived based on the calculation of Saada and Veyssiere [54], which is expressed as a function of the APB width on the cube and octahedral planes, w and w', respectively, rather than θ. Obviously, w, w' and θ are not independent, but are related in the following way:

$$\frac{w}{\sin\alpha} = \frac{w'}{\sin\theta}, \tag{3.29}$$

as illustrated in Figure 3-10(a). In the absence of applied stress, w' can be expressed as $w' = (d_c - w)\gamma_c/\gamma_o$, where d_c is the equilibrium APB width on the cube plane under the stress-free condition. In this case, the relation between w and θ is nearly linear and is drawn in figure 3-10 (b) with the energy ratio γ_c/γ_o taken as 0.8.

In Caillard's paper [42], the unlocking strength for the weakest incomplete K-W lock (with $w = b$) and the unlocking strength corresponding to a complete K-W lock (with $w = w_{max} = w_{APB}$) were given as:

$$\begin{aligned} \tau(w = b) &= \frac{\gamma_o}{b}\left[1 - \frac{\gamma_c}{\gamma_o}\frac{1 + 2/A}{\sqrt{3}}\right] && (3.30) \\ \tau(w = w_{APB}) &= \frac{\gamma_o}{b}\left[1 - \frac{\gamma_c}{\gamma_o}\frac{1}{\sqrt{3}}\right] && (3.31) \end{aligned}$$

These expressions are exactly the same as the outcomes of Eqn 3.27, if we apply the respective θ-values of 55° (which is the intersection-angle between the cube and the octahedral plane) and 0°. In the simulation we use θ as the variable due to the convenience in deriving the general form of $\tau_{critical}$, as expressed in Eqn 3.27.

Martin, *et al.*, [47] proposed that this self-unlocking mechanism was responsible for the decrease of the hardening rate in the anomalous yield region. To support this idea, experimentally measured yield strengths at temperature $T_{p,h}$ were plotted vs. the APB energy on the octahedral plane, γ_o for each material in Figure 2-9. The critical stress to unlock the weakest K-W locks, given by Eqn. 3.30 with $\gamma_c/\gamma_o \sim 0.8$, was also drawn vs. γ_o (the straight line in Figure 2-9). Martin, *et al.*, argued the fact that all experimental data points in Figure 2-9 fell along the theoretical line strongly implied that the decrease of hardening rate was caused by activation of the self-unlocking mechanism. We accept this idea in the proposed model, and further assume that θ follows a modified Gaussian distribution over the population of KW-locked screws, with a mean value $\bar{\theta}$ and a standard deviation of $\sigma_\theta = 3°$. The temperature dependence of $\bar{\theta}$ is not quantitatively derived as in the case of l_{max}, and a linear dependence of $\bar{\theta}$ on temperature is implemented in this proposed model to describe the assumed increases in strength of IKWs with increasing temperature. Since the angle θ has limits of $[\theta_{min} = 0°, \theta_{max} = 55°]$, the Gaussian distribution needs to be normalized to this region. Thus, the final probability density function of θ is given as:

$$P_\theta(\theta) = \frac{1}{\sqrt{2\pi\sigma_\theta^2}} \frac{\exp\left(\frac{-(\theta-\bar{\theta})^2}{2\sigma_\theta^2}\right)}{(N(55°) - N(0°))}, \tag{3.32}$$

where

$$N(\theta) = 1/2\left[1 + erf\left(\frac{\theta - \bar{\theta}}{\sigma_\theta\sqrt{2}}\right)\right] \tag{3.33}$$

is the cumulative probability distribution function for a Gaussian distribution. The critical unlocking stress $\tau_{critical}$ is calculated according Eqn. 3.27, as a function of θ and APB energy. If the applied resolved shear stress on the octahedral planes exceeds this critical value, the average dislocation velocity v_2 is taken to be a power law function of τ^α; otherwise these K-W locks do not self-unlock and the velocity of these screws is zero:

$$v_2 = \begin{cases} v_0^{SU}\left(\frac{\tau^\alpha(\theta,\gamma_o,\gamma_c)}{S_2(T)}\right)^{m_1} & \text{if } \tau > \tau_{critical}; \\ 0 & \text{otherwise.} \end{cases}$$

Since the rate of the self-unlocking mechanism is actually controlled by the cube slip of trailing superpartials, the power law form for v_2 is similar to the dislocation dynamics form we will give later for cube slip, with $m_1 = 20$, and $S_2(T)$ decreasing with increasing temperature. The plastic strain-rate contribution from the self-unlocking model is given by the following integral form:

$$\dot{\gamma}_2^\alpha = \rho_{total}^\alpha b \int_0^{\theta_{max}} P_\theta(\theta) v_2(\theta, \tau^\alpha) d\theta, \tag{3.34}$$

where $\theta_{max} = 55°$.

In this simulation, we assume P_{screw} and P_θ are independent distributions over the total population of KW-locked screws. There is a chance that a given screw is locked by very weak K-W locks and also has a very long superkink on it. Therefore, at an appropriate applied stress, it could be unlocked by both mechanisms. However, this chance is very small (it is the production of the probability of having longest superkinks and the probability of very weak K-W lock, by assuming P_{screw} and P_θ are independent distributions). So in the simulation, we simply superpose plastic contributions for the two mechanisms directly for the octahedral slip, and

$$\dot{\gamma}_{octahedral}^\alpha = \dot{\gamma}_1^\alpha + \dot{\gamma}_2^\alpha. \tag{3.35}$$

3.2.3 Octahedral slip for [001] orientation at temperatures exceeding $T_{p,\sigma}$

As mentioned before, it is commonly agreed that the normal temperature-dependence of yield strength at temperatures above the peak yielding temperature, $T_{p,\sigma}$, is due to the activation of cube slips. For uniaxial stressing along the [001] orientation, however, a decrease of yield strength has also been observed at very high temperatures ($> 1000K$), even though there are no resolved shear stress components on the cube planes. Negligible modeling research has been focused on this phenomenon, and the underlying mechanisms are not well understood.

Rentenberger and Karnthaler [21] carried out studies in this area by a series of [001]-oriented compression tests on single-crystal Ni_3Al at temperatures in both the 'anomalous' and the 'normal' regions. Strain softening was observed at temperatures above $T_{p,\sigma}$, as show in Figure 3-11(a), consistent with the corresponding negative strain hardening rate reported in Staton-Bevans [8], as shown in Figure 3-11 (b). Rentenberger and Karnthaler also presented TEM observations for these different deformation temperatures. It was confirmed that for the [001] orientation, the active slip-systems were always octahedral, whether the sample was deformed above or below $T_{p,\sigma}$, but the resulting dislocation substructures are quite different. Figure 3-12 shows the dislocation structure of a sample deformed at $600°C$, which is below the peak-yield temperature for [001]. We can see the dominance of long, locked screw dislocations, which is the typical substructure for Ni_3Al in the yield anomaly regime. Figures 3-13 and 3-14 reveal the dislocation structure of samples deformed at $835°C$ and $920°C$, respectively, both above $T_{p,\sigma}$. In these images, screw and edge dislocations are present in roughly equal density, and both are locked with their APB ribbons lying entirely on the cube plane. Based on these TEM observations, Rentenberger and Karnthaler proposed that at very high temperatures, and in the absence of cube-system driving stress, the KW-locked screws/edges can still move via diffusion mechanisms. They also performed compression tests at $835°C$ under different applied strain-rates [55], and found that the stress-strain curve showed a prominent yield drop under the slow strain-rate of $1.1 \times 10^{-4}s^{-1}$, while 'normal' hardening behavior (hardening without yield drop) was evident under the fast applied strain-rate of $2.2 \times 10^{-3}s^{-1}$, as shown in Figure 3-15. The dislocation substructure observed in the sample under fast deformation is dominated by long locked screws (Figure 3-16(b)), similar to the substructure in the yield anomaly region, and is quite different from the substructure of slow deformation (Figure 3-16(a)). The strain-rate dependence was explained as follows: under the rapid applied strain-rate, $|\dot{\epsilon}_{app}|$ is too large for the diffusion mechanism to drive a sufficient dislocation flux, and thus the stress is soon raised to activate the self-unlocking mechanism, and the normal hardening stress-strain relation is presented. Conversely, a lower value of $|\dot{\epsilon}_{app}|$ makes the diffusion mechanism possible.

Rentenberger and Karnthaler carried out a very simple 1-D simulation with Johnston's model [56], in which the mobile dislocation density was assumed to increase dramatically with plastic deformation in order to capture the yield drop.

Here, we propose that the average dislocation velocity due to diffusion can be expressed as:

$$v^{\alpha} = v_0^d \left(\frac{\tau^{\alpha}}{S_d}\right)^{m_2} \exp\left(-\frac{H_d}{kT}\right), \tag{3.36}$$

where v_0^d is a reference velocity, $m_2 = 1$ is the strain-rate sensitivity exponent and S_d is the deformation resistance. Eqn 3.36 shows the velocity is positively dependent on temperature, since the diffusion process is accelerated at higher temperature. Considering that the cross-slipped APB width, w, on the cube plane will be shorter in a crystal with higher APB energy, the locked screws and edges should have higher mobility in crystals having higher APB energy. Thus, to incorporate this dependence, the activation enthalpy H_d is formally expressed as $H_d = H_{d0} - A\gamma_c$, where γ_c is the APB energy on the cube plane.

We assume that in the initial portions of the high-temperature loading process, dislocations are generated and the screws cross-slip to form long KW locks. For each slip system, the initial total screw dislocation density is assumed to be $10^{11} m^{-2}$, and the initial mobile screw dislocation density is considered very low and is taken to be $10^6 m^{-2}$. With further deformation, more and more of the locked screws can move with the diffusion mechanism. The mobile dislocation density evolves according to the following form, as long as it is smaller than the total dislocation density:

$$\dot{\rho}_m^{\alpha} = \rho_{total}^{\alpha} \left(\frac{\tau^{\alpha}}{S_d}\right)^2 f_2 \exp\left(-\frac{H_d}{kT}\right). \tag{3.37}$$

In Eqn. 3.37, the term $f_2 \exp\left(-\frac{H_d}{kT}\right)$ shows that the diffusion mechanism is thermally activated, and f_2 is the attempt frequency.

The total screw dislocation density is considered to decrease due to a dynamic annihilation mechanism, and the evolution equation is defined as:

$$\dot{\rho}_{total}^{\alpha} = -C_{\rho} \rho_m^{\alpha} \rho_{total}^{\alpha} R v^{\alpha}, \tag{3.38}$$

where C_{ρ} is a constant and R is a characteristic capture radius.

3.3 Cube-slip

Simulation of the normal region, the temperature region beyond $T_{p,\sigma}$, is not the focus of this thesis work. The cube-slip dislocation dynamics is simply assumed to follow a standard power-law form:

$$\dot{\gamma}^{\alpha}_{cube} = \dot{\gamma}_o (\frac{\tau^{\alpha}}{S_1(T)})^{m_1}, \tag{3.39}$$

where $S_1(T)$ is the cube slip resistance, which is assumed to be linearly dependent on temperature, in the simulation temperature region (300K $\sim$ 1100K):

$$S_1(T) = (1000 - 0.75T(\mathrm{K}))\, MPa, \tag{3.40}$$

and $m_1 = 20$ is the strain-rate sensitivity exponent, which is derived from the experimental data shown in Figure 3-17 (a). We assume the deformation in the normal yield range is basically contributed from the cube slip, and due to the relatively low hardening rate in this range, the plastic strain-rate from cube-slip is close to the applied strain-rate. Thus, if we plot Eqn. 3.39 in a log-log form (Figure 3-17(b)) and put in the test data from Figure 3-17 (a) for temperatures 780, 875 and 975K, m_1 is derived as the average value of the slope for these three cases, which is close to 20.

Cube-slip was first included in the model to make a more complete description of the temperature-dependence of yield strength in $L1_2$ single crystal. Later, we find that the basic understandings (rate-dependence, temperature-dependence) of the cube dynamics are also necessary and useful to fulfill the simulation for the octahedral planes, since the abnormal octahedral-slip is accompanied with cross-slips onto cube planes. That is why the velocity of self-unlocking mechanism is taken to have a power-law form similar to Eqn. 3.39. Moreover, as we will discuss in Chapter 5, for some loading orientations (e.g. $[\bar{1}11]$), the changes of temperature-dependence for yield strength and strain-hardening are both due to the activation of cube-slip.

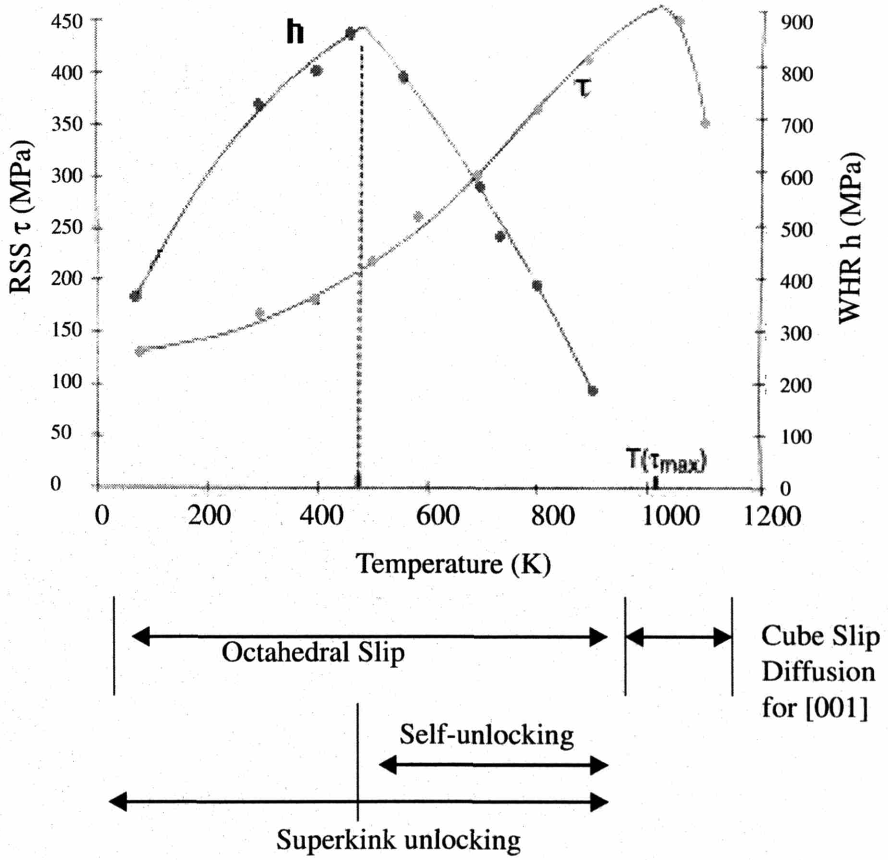

Figure 3-1: Schematic illustration of the model framework: Typical temperature-dependence curves of both the yield strength and the strain hardening rate are plotted. Octahedral slips dominate the yield anomaly region, and, for temperatures higher than $T_{p,\sigma}$, cube slips dominate (for [001] orientation, a diffusion mechanism dominates). In the yield anomaly region, the strain hardening rate monotonically increases with increasing temperature, until the activation of the self-unlocking mechanism.

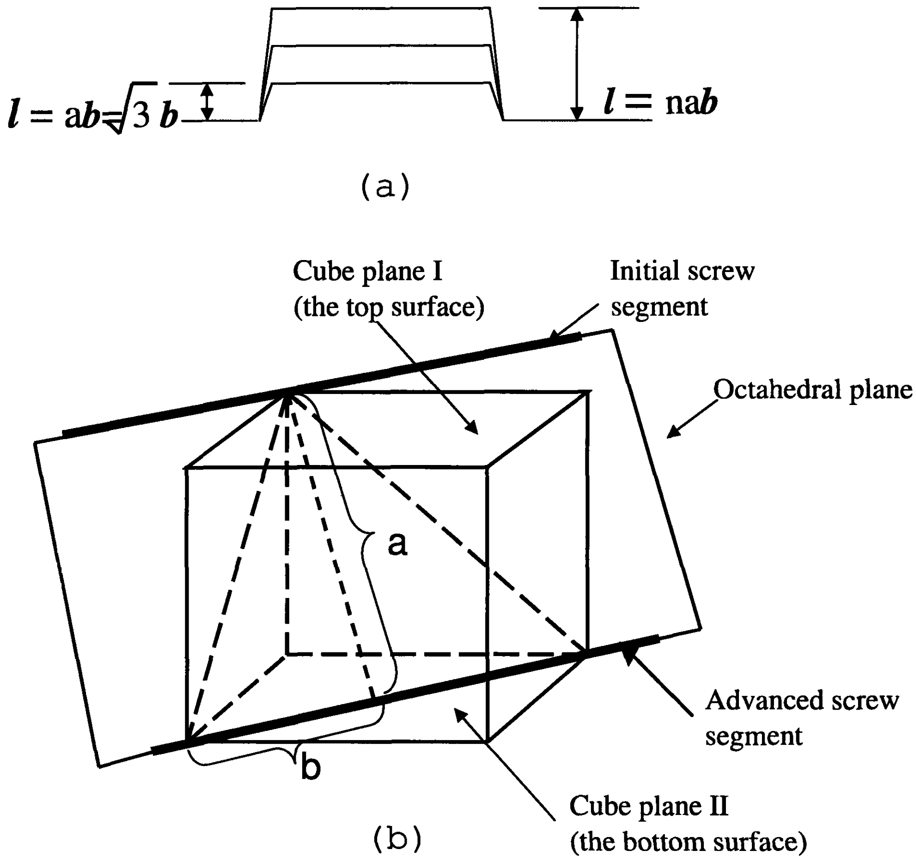

Figure 3-2: Schematics of formation of the initial superkink distribution: (a) the screw segment may advance different distances before it cross-slips and gets locked; (b) 3-D illustration of distance between two adjacent cube planes on an octahedral plane, a, and the magnitude of Burgers vector b.

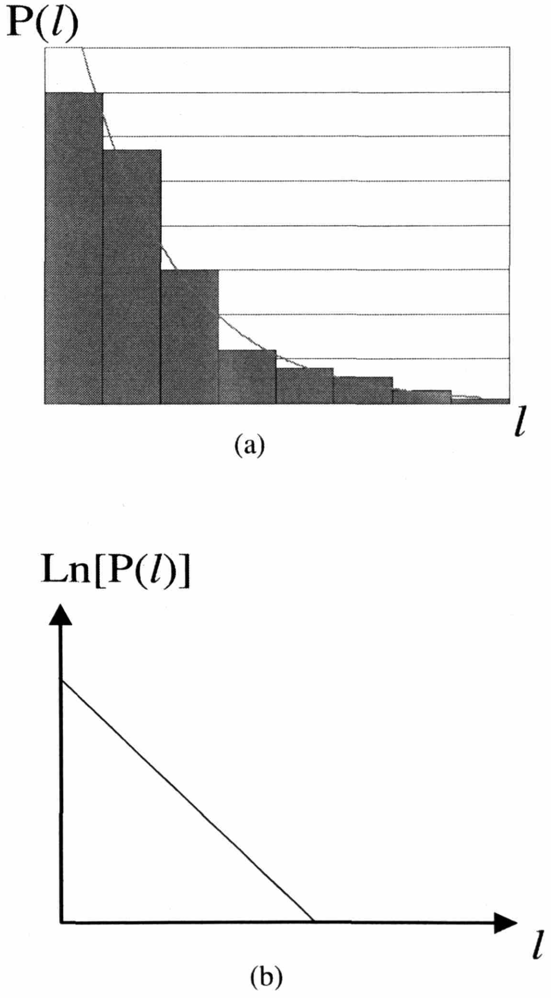

Figure 3-3: Schematic illustration of the distribution of superkinks as a function of their height: (a) normal-form (b) logarithm-form

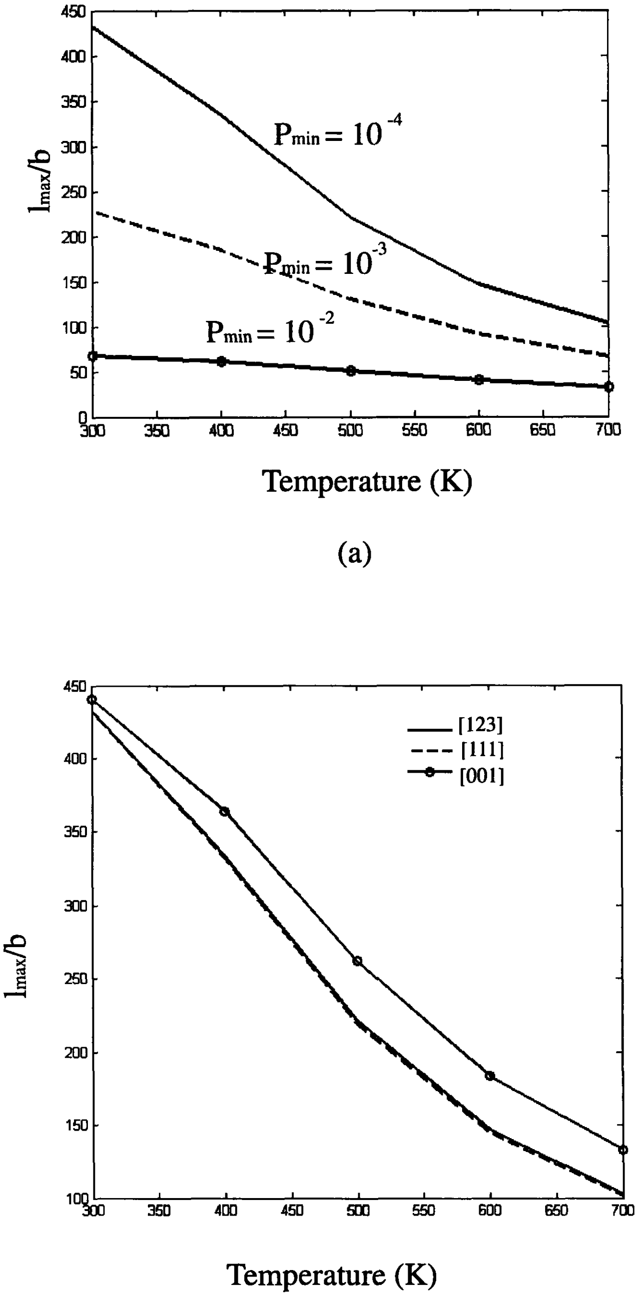

(a)

(b)

Figure 3-4: (a) l_{max}/b, given by Eqn. 3.8 (where $q = 0.99$ and p^{α} is given by Eqn. 3.4), decreases with increasing temperature, and depends on the value of P_{min} (compression in [123]). (b) Orientation-dependence of l_{max} with $P_{min} = 10^{-4}$ and $q = 0.99$: the value of S_{pe} corresponding to the active slip-system for [001], [123], and [$\bar{1}$11] orientations in compression are -0.2357, 0.1347 and 0.1574, respectively.

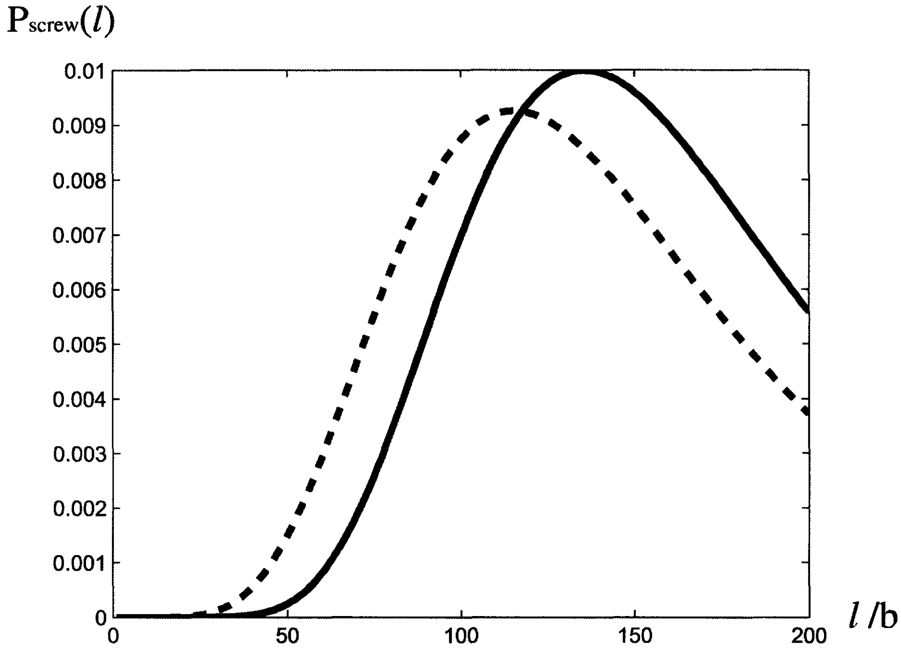

Figure 3-5: Screw distribution, P_{screw}, as a function of the height of the longest superkink on the screw: Solid line is with $\bar{n} = 15$, dotted line is with $\bar{n} = 10$. In both cases $\sigma_n = 1$ and $l_0 = 50b$.

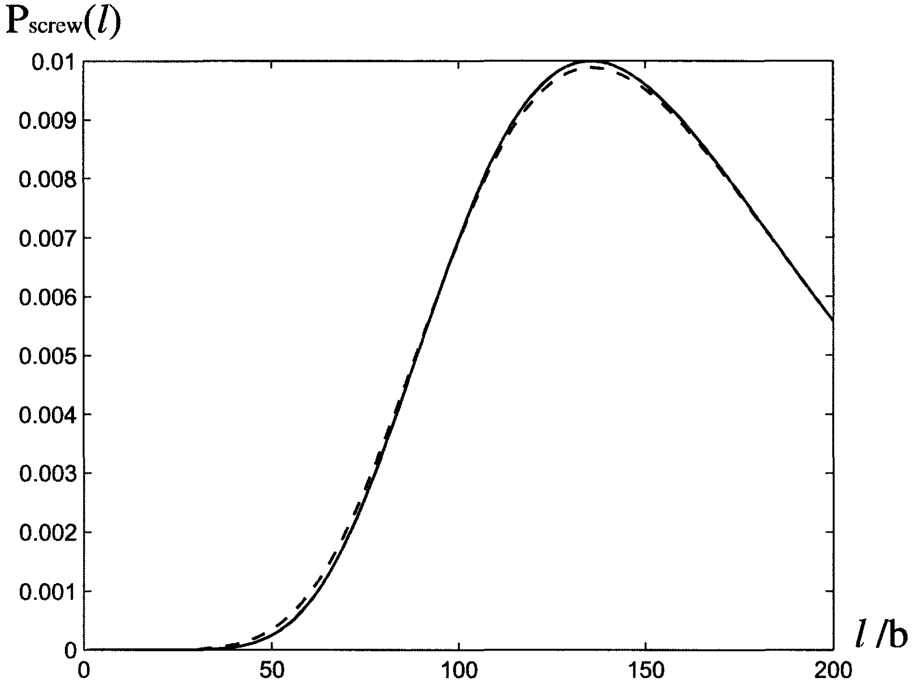

Figure 3-6: Screw distribution, P_{screw}, as a function of the height of the longest superkink on the screw: Solid line is with $\sigma = 1$, dotted line is with $\sigma_n = 2.5$, In both cases, $\bar{n} = 10$ and $l_0 = 50b$

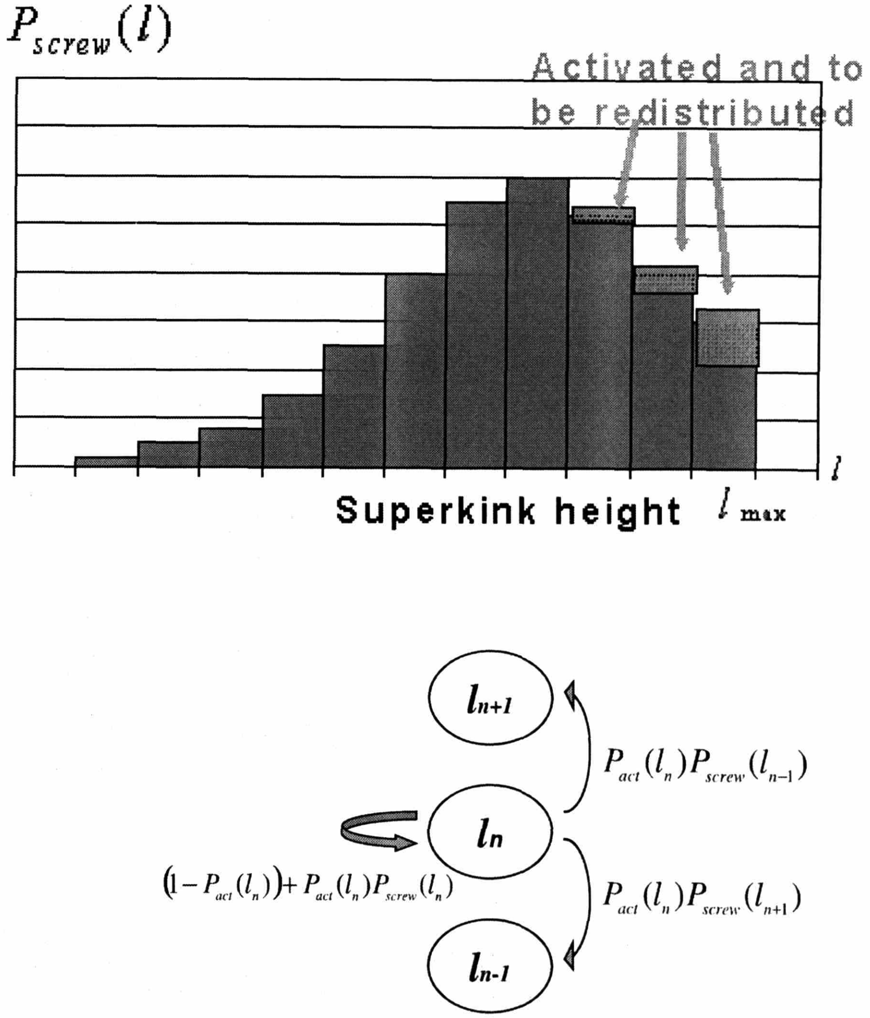

Figure 3-7: Schematic illustration of the activation and redistribution of screw dislocations.

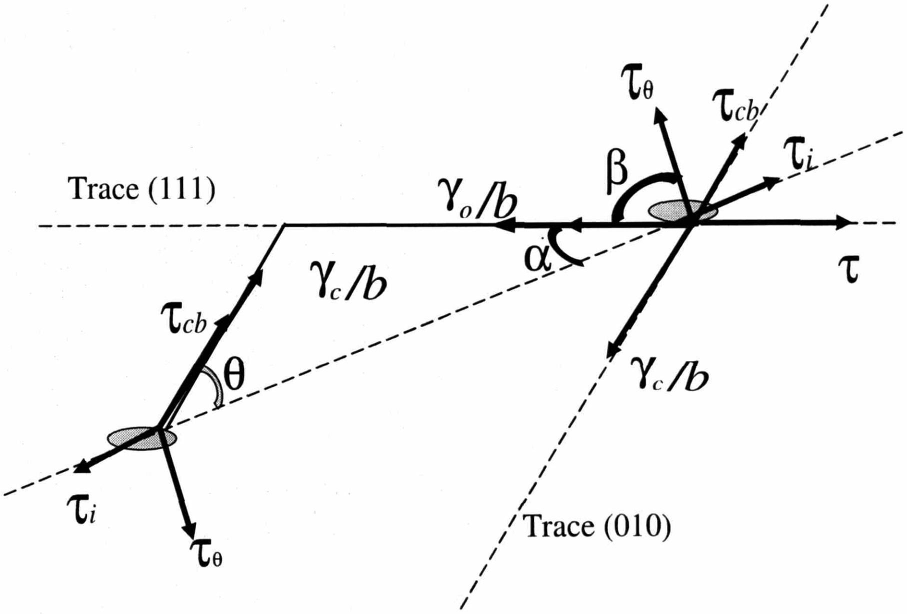

Figure 3-8: Stress analysis for an incomplete K-W lock. The core structure of both the leading and trailing superpartials is neglected.

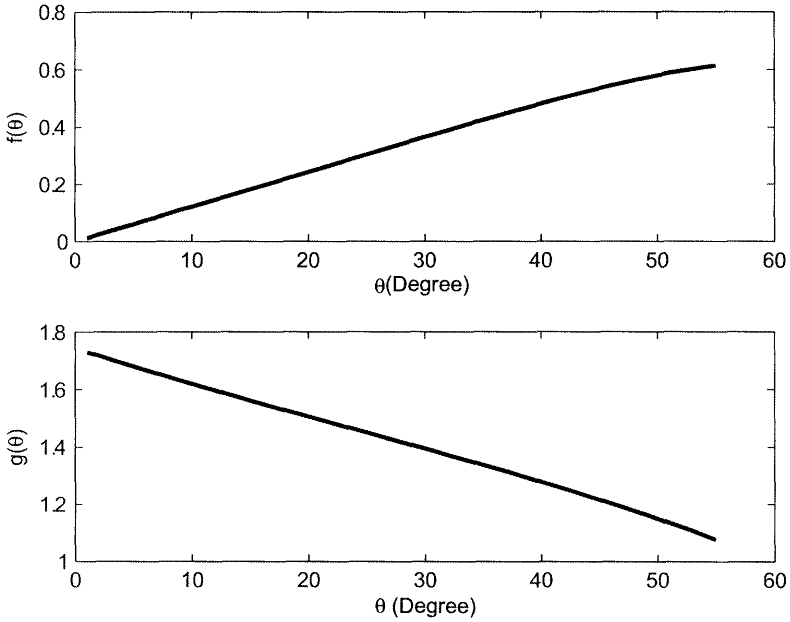

Figure 3-9: Illustration of $f(\theta)$ given by Eqn. 3.19 and $g(\theta)$ given by Eqn. 3.28.

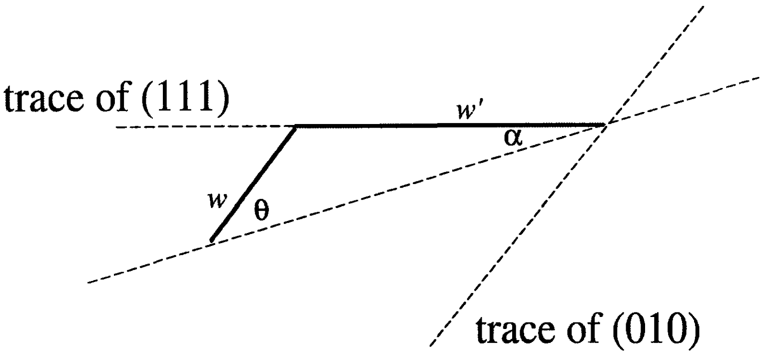

(a)

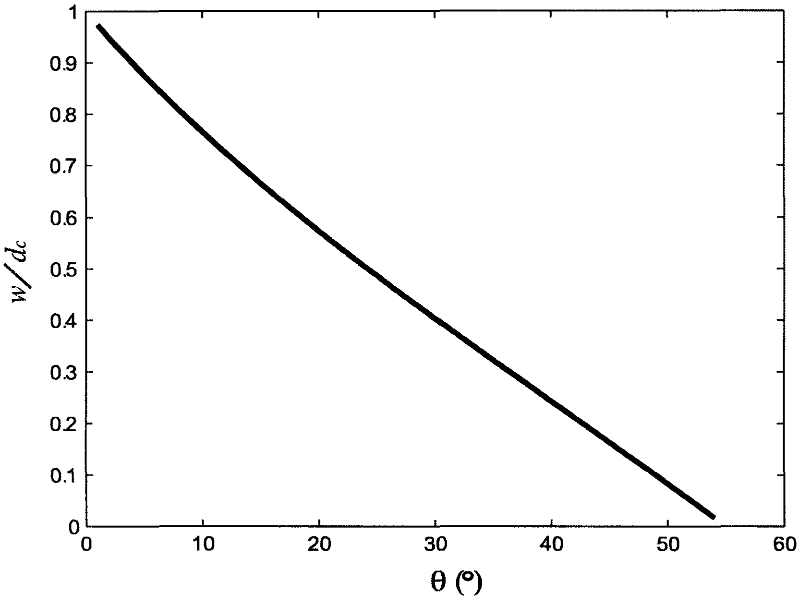

(b)

Figure 3-10: (a) Relation of w and w' vs. θ and α; (b) w/d_c as function of θ at stress free condition and with $\frac{\gamma_c}{\gamma_o} = 0.8$, and d_c is the cube plane APB width plane under zero applied stress.

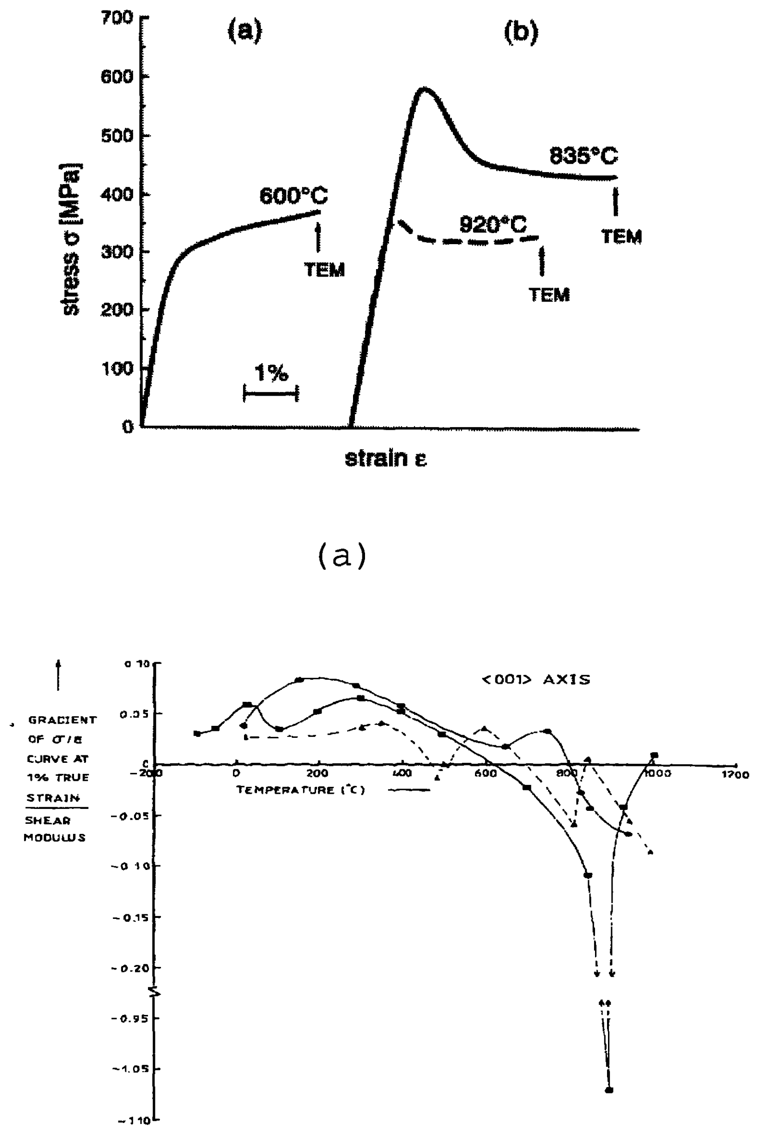

(a)

(b)

Figure 3-11: (a) Stress-strain curves for single crystal Ni_3Al in [001] compression tests [21]. At temperatures higher than $T_{p,\sigma}$, yield drop was observed. (b) Temperature-dependence of strain hardening rate of three Ni_3Al single crystal compressed in [001] orientation [8]. The strain hardening rate presents negative value at temperatures higher than $T_{p,\sigma}$.

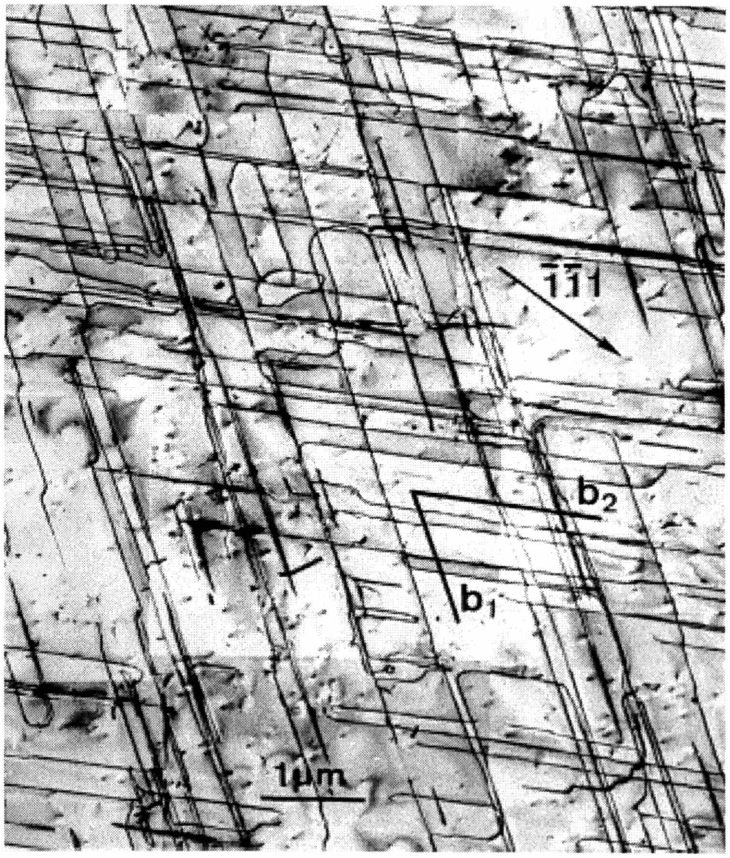

Figure 3-12: TEM observation for deformed single-crystal Ni_3Al after [001] compression at 600°C [21].

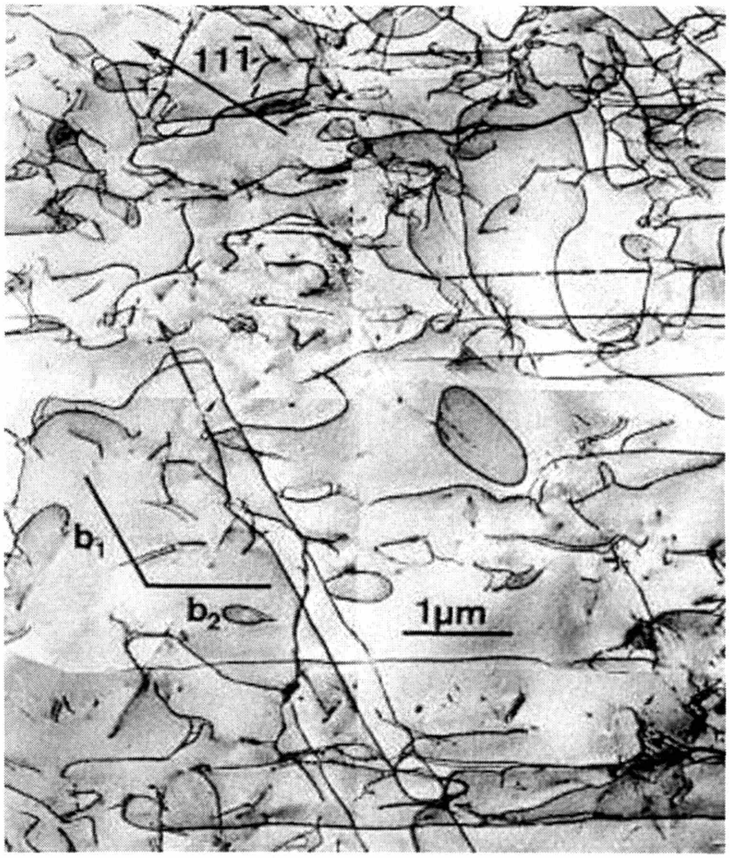

Figure 3-13: TEM observation for deformed single-crystal Ni_3Al after [001] compression at 820°C [21].

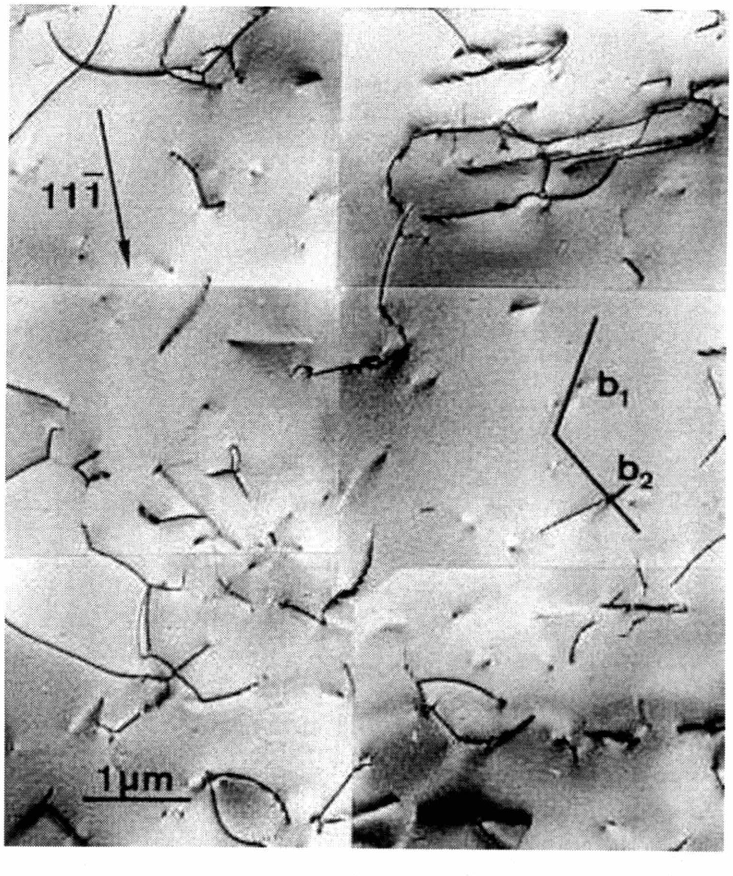

Figure 3-14: TEM observation for deformed single crystal Ni_3Al after [001] compression at 935°C [21]

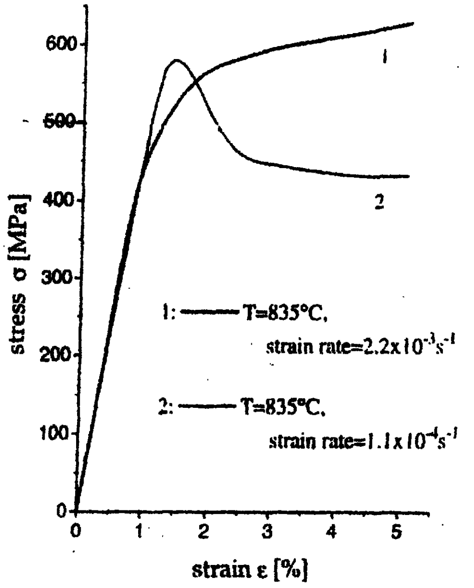

Figure 3-15: Deformation curves of two specimens in [001] compression at 835°C with different applied strain-rates [55]. Yield drop is only observed in compression test with slow applied strain-rate.

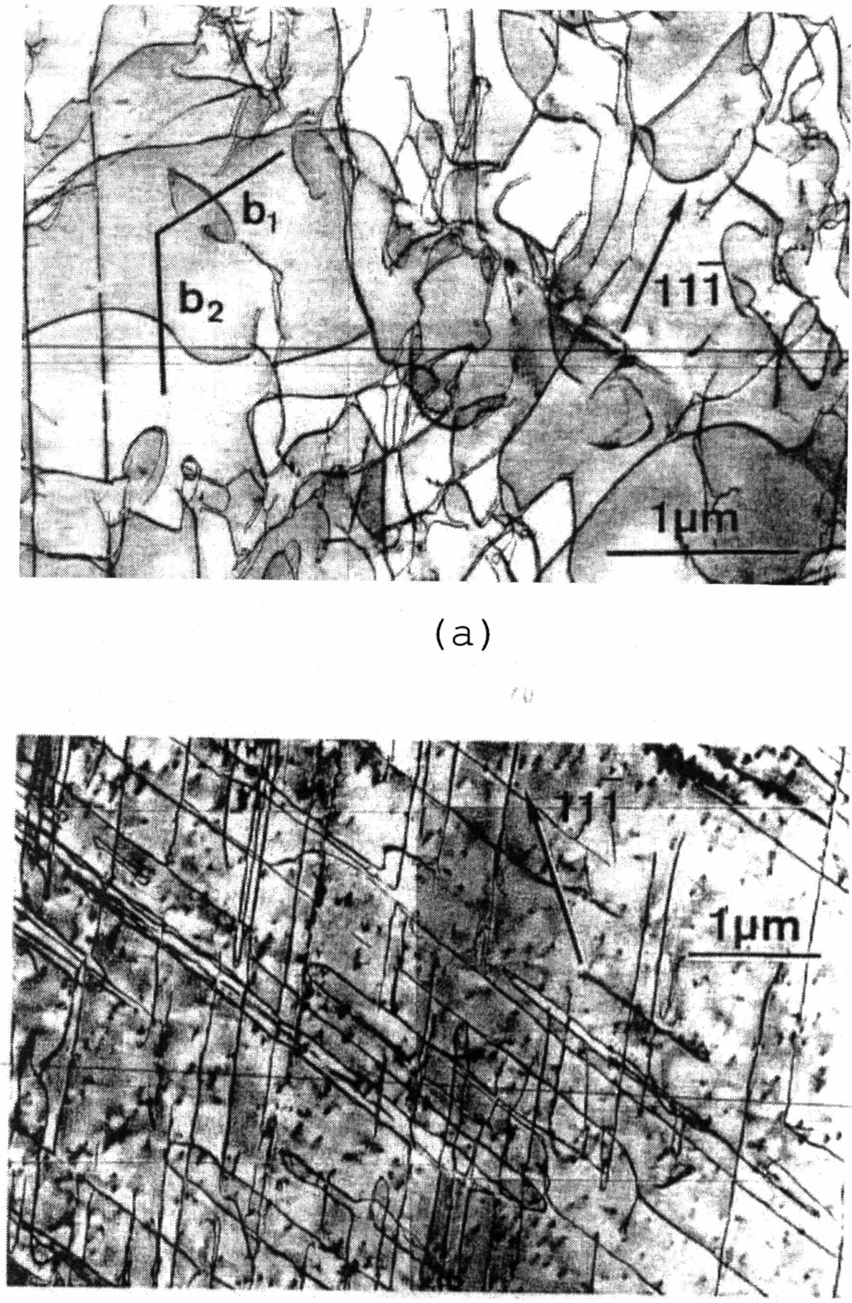

(a)

(b)

Figure 3-16: TEM observation for deformed single-crystal Ni_3Al after [001] compression at 835°C under different applied strain-rates. (a) $|\dot{\epsilon}_{app}| = 1.1 \times 10^{-4} s^{-1}$, (b) $|\dot{\epsilon}_{app}| = 2.2 \times 10^{-3} s^{-1}$ [55].

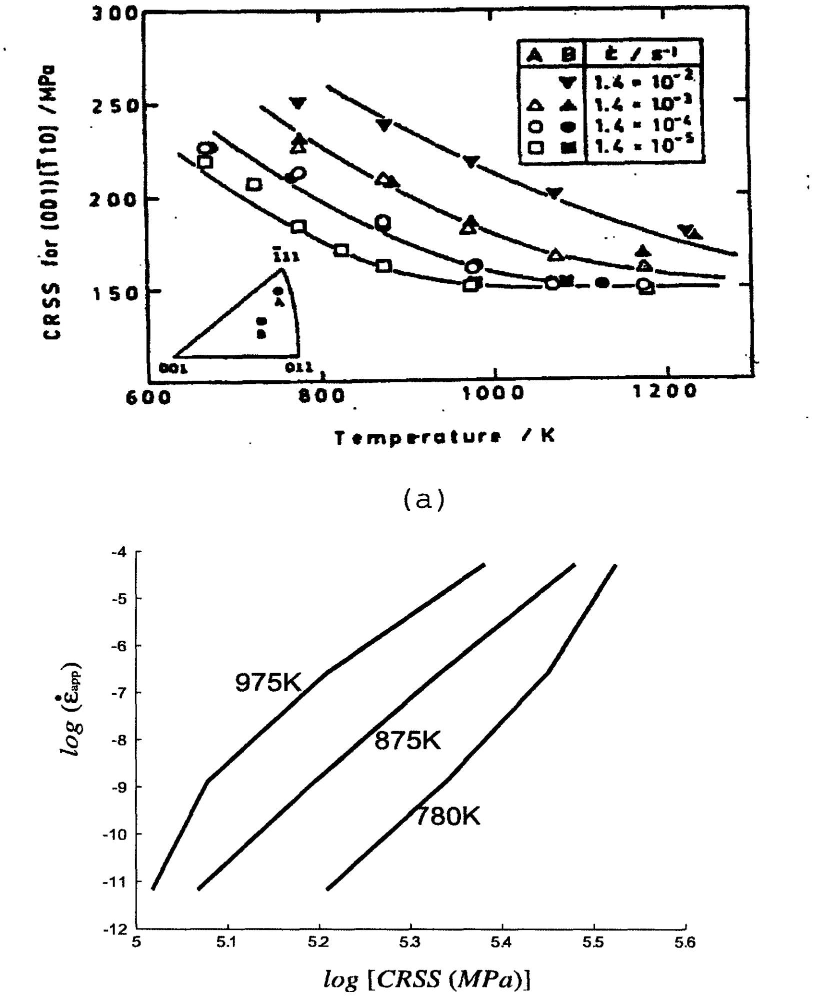

(a)

(b)

Figure 3-17: (a) Temperature and strain-rate dependence of CRSS for (001)[$\bar{1}$10] for single-crystal $Ni_3Al(24at\%Al)$ [18].

Table 3.1: The octahedral slip systems.

α	$(\mathbf{n}^\alpha)[\mathbf{m}^\alpha]$	$(\mathbf{n}^\alpha_{pe})[\mathbf{m}^\alpha_{pe}]$	$(\mathbf{n}^\alpha_{se})[\mathbf{m}^\alpha_{se}]$	$(\mathbf{n}^\alpha_{cb})[\mathbf{m}^\alpha_{cb}]$
1	$(111)[1\bar{1}0]$	$(111)[11\bar{2}]$	$(\bar{1}\bar{1}1)[\bar{1}\bar{1}\bar{2}]$	$(100)[01\bar{1}]$
2	$(111)[\bar{1}01]$	$(111)[1\bar{2}1]$	$(\bar{1}1\bar{1})[\bar{1}\bar{2}\bar{1}]$	$(010)[\bar{1}01]$
3	$(111)[01\bar{1}]$	$(111)[\bar{2}11]$	$(1\bar{1}\bar{1})[\bar{2}\bar{1}\bar{1}]$	$(001)[1\bar{1}0]$
4	$(1\bar{1}\bar{1})[110]$	$(1\bar{1}\bar{1})[1\bar{1}2]$	$(\bar{1}1\bar{1})[\bar{1}12]$	$(100)[0\bar{1}1]$
5	$(1\bar{1}\bar{1})[\bar{1}0\bar{1}]$	$(1\bar{1}\bar{1})[12\bar{1}]$	$(\bar{1}\bar{1}1)[\bar{1}21]$	$(0\bar{1}0)[\bar{1}0\bar{1}]$
6	$(1\bar{1}\bar{1})[0\bar{1}1]$	$(1\bar{1}\bar{1})[\bar{2}\bar{1}\bar{1}]$	$(111)[\bar{2}11]$	$(00\bar{1})[110]$
7	$(\bar{1}1\bar{1})[\bar{1}\bar{1}0]$	$(\bar{1}1\bar{1})[\bar{1}12]$	$(1\bar{1}\bar{1})[1\bar{1}2]$	$(\bar{1}00)[011]$
8	$(\bar{1}1\bar{1})[10\bar{1}]$	$(\bar{1}1\bar{1})[\bar{1}\bar{2}\bar{1}]$	$(111)[1\bar{2}1]$	$(010)[10\bar{1}]$
9	$(\bar{1}1\bar{1})[011]$	$(\bar{1}1\bar{1})[21\bar{1}]$	$(\bar{1}\bar{1}1)[2\bar{1}1]$	$(00\bar{1})[\bar{1}\bar{1}0]$
10	$(\bar{1}\bar{1}1)[\bar{1}10]$	$(\bar{1}\bar{1}1)[\bar{1}\bar{1}\bar{2}]$	$(111)[11\bar{2}]$	$(\bar{1}00)[0\bar{1}\bar{1}]$
11	$(\bar{1}\bar{1}1)[101]$	$(\bar{1}\bar{1}1)[\bar{1}21]$	$(1\bar{1}\bar{1})[12\bar{1}]$	$(0\bar{1}0)[101]$
12	$(\bar{1}\bar{1}1)[0\bar{1}\bar{1}]$	$(\bar{1}\bar{1}1)[2\bar{1}1]$	$(\bar{1}1\bar{1})[21\bar{1}]$	$(001)[\bar{1}10]$

Table 3.2: The cube slip systems.

α	$(\mathbf{n}^\alpha)[\mathbf{m}^\alpha]$
1	$(100)[011]$
2	$(100)[01\bar{1}]$
3	$(010)[101]$
4	$(010)[10\bar{1}]$
5	$(001)[110]$
6	$(001)[1\bar{1}0]$

Chapter 4

Finite Element Implementation of the Proposed Single-Crystal Plasticity Model

4.1 General Continuum Framework of Crystal Plasticity

The basic equations of the single-crystal constitutive framework have been described by Anand [57]. The total deformation gradient, $\mathbf{F}$, mapping a reference configuration of the material to the final configuration, may be decomposed by the following form (Figure 4-1):

$$\mathbf{F} = \mathbf{F}^e\mathbf{F}^p, \tag{4.1}$$

where $\mathbf{F}^p$, the plastic deformation gradient, locally maps the original configuration to an intermediate configuration which describes the effects of plastic deformation on an unrotated and undeformed crystal lattice, and *det* $\mathbf{F}^p = 1$. The elastic deformation gradient, $\mathbf{F}^e$, maps the local intermediate configuration to the final deformed configuration, and is associated with small elastic stretches and arbitrary rigid-body rotations. The evolution equation for the plastic deformation gradient is given by the flow rule:

$$\dot{\mathbf{F}}^p = \mathbf{L}^p\mathbf{F}^p, \tag{4.2}$$

where $\mathbf{L}^p$ is the plastic flow rate. In crystals, $\mathbf{L}^p$ is comprised of the superposition of the resolved crystallographic plastic shear rates, $\dot{\gamma}^\alpha$, such that:

$$\mathbf{L}^p = \sum_\alpha \dot{\gamma}^\alpha \mathbf{m}_0^\alpha \otimes \mathbf{n}_0^\alpha, \tag{4.3}$$

where $\mathbf{m_0}^\alpha$ and $\mathbf{n}_0^\alpha$ are unit lattice vectors, defining the slip direction and the slip plane normal of the slip system α respectively, in a fixed reference configuration. The plastic shearing strain rate on each system, $\dot{\gamma}^\alpha$, is given by Orowan's equation:

$$\dot{\gamma^\alpha} = \rho_m^\alpha b \bar{v}^\alpha, \tag{4.4}$$

where ρ_m^α is the density of the mobile dislocations for slip system α, b is the magnitude of the Burgers vector, and $\bar{v}^\alpha$ is the average velocity of the mobile dislocations for slip system α.

During plastic deformation, the crystal lattice may elastically stretch and rotate. In the deformed configuration, the slip direction and slip plane normal, $\mathbf{m}_*^\alpha$ and $\mathbf{n}_*^\alpha$, are related to the initial lattice directions by the elastic deformation gradient:

$$\mathbf{m}_*^\alpha = \mathbf{F}^e\mathbf{m}_0^\alpha; \qquad \mathbf{n}_*^\alpha = \mathbf{F}^e\mathbf{n}_0^\alpha. \tag{4.5}$$

At given temperature, the constitutive equation for stress is given in terms of a linear elastic relation:

$$\bar{\mathbf{T}} = \mathcal{L}[\mathbf{E}^e], \tag{4.6}$$

where the elastic strain measure, $\mathbf{E}^e$, corresponding to the Cauchy-Green strain with respect to the intermediate configuration, is defined as:

$$\mathbf{E}^e \equiv \frac{1}{2}\left\{\mathbf{F}^{eT}\mathbf{F}^e - \mathbf{I}_2\right\}, \tag{4.7}$$

in which, $\mathbf{I}_2$ is the second-order identity tensor.

The work-conjugate stress measure in Eqn. 4.6, $\bar{\mathbf{T}}$, corresponding to the second Piola-Kirchhoff stress with respect to the intermediate configuration, is related to Cauchy stress, $\mathbf{T}$, through the following transformation:

$$\bar{\mathbf{T}} = \det(\mathbf{F}^e)\mathbf{F}^{e-1}\mathbf{T}\mathbf{F}^{e-\mathbf{T}}, \tag{4.8}$$

and $\mathcal{L}$ in Eqn. 4.6 is the temperature-dependent fourth-order anisotropic elasticity tensor.

4.2 Finite Element Implementation of the Proposed Constitutive Model

The proposed mechanism-based constitutive model was implemented as a user-defined material (UMAT) in the FEM package ABAQUS/Standard, and was used with first-order reduced integration brick (C3D8R) elements to simulate the behavior of single-crystal Ni_3Al subject to uniaxial tension and compression at different temperatures.

As in typical implicit finite element calculations using nonlinear constitutive models, ABAQUS/Standard applies the discretized principle of virtual work (PVW) to enforce weak-form equilibrium and traction boundary conditions. An estimated incremental displacement field $\Delta\mathbf{u}$ was derived at the beginning of each time step, and the stress field is calculated based on $\Delta\mathbf{u}$. If the calculated stress field does not satisfy the PVW equilibrium, the estimated $\Delta\mathbf{u}$ will be modified, and the stress field will be recalculated. This interactive procedure continues until the PVW is satisfied to within acceptable tolerances. The inputs to the UMAT interface are the total deformation gradient at time t, $\mathbf{F}(t)$; the Cauchy stress at time t, $\mathbf{T}(t)$; an estimate of the total deformation gradient at time $t^* = t + \Delta t$, $\mathbf{F}(t^*)$; and a set of state-dependent variables at time t.

Given the input variables to the UMAT interface, the subroutine is responsible for calculating the Cauchy stress at time t^*, $\mathbf{T}(t^*)$; the plastic deformation gradient at time t^*, $\mathbf{F}^p(t^*)$; the material jacobian at time t^*, $\mathcal{C}(t^*)$; and update the state-dependent variables.

Time Integration Procedure

The determination of the state at time t^* from the inputs to the UMAT subroutine employs a backward Newton solving algorithm.

For crystalline materials the elastic stretch is usually infinitesimal, thus the second P-K stress measure corresponding to the intermediate configuration is considered to be linearly related to the elastic Green strain measure as given in Eqn 4.6,

$$\bar{\mathbf{T}} = \mathcal{L}[\mathbf{E}^e],$$

with Eqn. 4.7, $\mathbf{E}^e \equiv \frac{1}{2}\left\{\mathbf{F}^{eT}\mathbf{F}^e - \mathbf{I}_2\right\}$, and Eqn. 4.1, $\mathbf{F} = \mathbf{F}^e\mathbf{F}^p$, we can rewrite the constitutive equation into the following form:

$$\bar{\mathbf{T}}(t^*) = \frac{1}{2}\mathcal{L}\left\{\mathbf{F}^{p-T}(t^*)\mathbf{F}^T(t^*)\mathbf{F}(t^*)\mathbf{F}^{p-1}(t^*) - \mathbf{I}_2\right\}. \tag{4.9}$$

Assuming that $\mathbf{L^p}$ is constant over the time increment, time integration of the plastic flow rule in Eqn. 4.2 leads to:

$$\mathbf{F}^p(t^*) = \exp[\Delta t\mathbf{L}^p(t^*)]\mathbf{F}^p(t). \tag{4.10}$$

The inelastic deformation increments taken during the course of the deformation are typically small, allowing for the exponential in Eq. 4.10 to be approximated by a Taylor series to give:

$$\mathbf{F}^p(t^*) \doteq [\mathbf{I}_2 + \Delta t\mathbf{L}^p(t^*)]\mathbf{F}^p(t). \tag{4.11}$$

Inversion of Eqn. 4.11 to the same level of accuracy with the substitution of the crystallographic slip rates for the plastic velocity gradient from Eqn. 4.3 leads to:

$$\mathbf{F}^{p-1}(t^*) \doteq \mathbf{F}^{p-1}(t)[\mathbf{I}_2 - \Delta t \sum_\alpha \dot{\gamma}^\alpha(t^*)\mathbf{S}^\alpha], \tag{4.12}$$

where

$$\mathbf{S}^\alpha = \mathbf{m}_0^\alpha \otimes \mathbf{n}_0^\alpha. \tag{4.13}$$

The determinant of $\mathbf{F}^{p-1}(t^*)$ calculated by Eqn. 4.12 is not precisely equal to 1, as it must. Therefore, $\mathbf{F}^{p-1}(t^*)$ is normalized at each time step to make $det\mathbf{F}^{p-1}(t^*) = 1$.

The plastic shearing strain rate on each system is defined, at fixed temperature, as a function of the resolved shear stress on each slip system:

$$\dot{\gamma}^\alpha(t^*) = \dot{\gamma}^\alpha(\tau^\alpha(t^*)). \tag{4.14}$$

where

$$\tau^\alpha = \mathbf{m}_0^\alpha \bar{\mathbf{T}}(t^*)\mathbf{n}_0^\alpha$$

Substitution of Eqn. 4.12 into Eqn. 4.9 leads to the following relationship:

$$\bar{\mathbf{T}}(t^*) \doteq \bar{\mathbf{T}}^{tr} - \Delta t \sum_\alpha \dot{\gamma}^\alpha(\bar{\mathbf{T}}(t^*))\mathbf{C}^\alpha, \tag{4.15}$$

where

$$\bar{\mathbf{T}}^{tr} = \frac{1}{2}\mathcal{L}[\mathbf{B} - \mathbf{I}_2], \tag{4.16}$$

$$\mathbf{B} = \mathbf{F}^{p-T}(t)\mathbf{F}^T(t^*)\mathbf{F}(t^*)\mathbf{F}^{p-1}(t), \tag{4.17}$$

$$\mathbf{C}^\alpha = \frac{1}{2}\mathcal{L}[\mathbf{K}^\alpha], \tag{4.18}$$

and

$$\mathbf{K}^\alpha = \mathbf{B}\mathbf{S}^\alpha + \mathbf{S}^{\alpha T}\mathbf{B}. \tag{4.19}$$

All of the quantities in Eqns. 4.16 – 4.19 are known, and Eqn 4.15 can be rewritten as the following:

$$\mathbf{W}\left(\bar{\mathbf{T}}(t^*)\right) = \bar{\mathbf{T}}(t^*) - \bar{\mathbf{T}}^{tr} + \Delta t \sum_{\alpha} \dot{\gamma}^{\alpha}(\bar{\mathbf{T}}(t^*))\mathbf{C}^{\alpha} = 0, \tag{4.20}$$

$\bar{\mathbf{T}}(t^*)$ is the solution to the above nonlinear function. The typical Newton method is applied, and $\bar{\mathbf{T}}(t^*)$ is iteratively solved. A column vector, $\mathbf{Z}$, is created by containing the second Piola-Kirchhoff stress tensor as a six-dimensional vector in the following manner:

$$\mathbf{Z} = \begin{bmatrix} \bar{\mathbf{T}}_{11}(t^*) \\ \bar{\mathbf{T}}_{22}(t^*) \\ \bar{\mathbf{T}}_{33}(t^*) \\ \bar{\mathbf{T}}_{12}(t^*) \\ \bar{\mathbf{T}}_{23}(t^*) \\ \bar{\mathbf{T}}_{31}(t^*) \end{bmatrix} = \begin{bmatrix} \bar{\mathbf{T}}_{1}(t^*) \\ \bar{\mathbf{T}}_{2}(t^*) \\ \bar{\mathbf{T}}_{3}(t^*) \\ \bar{\mathbf{T}}_{4}(t^*) \\ \bar{\mathbf{T}}_{5}(t^*) \\ \bar{\mathbf{T}}_{6}(t^*) \end{bmatrix} \tag{4.21}$$

According to the Newton method, the solution of the stress after the nth iteration is given by:

$$\mathbf{Z}_{n+1} = \mathbf{Z}_n - \mathcal{F}^{-1}[\mathbf{W}_n], \tag{4.22}$$

where $\mathbf{W}_n$ is the value of Eqn. 4.20 at the nth iteration,

$$\mathbf{W}_n = \left[\bar{\mathbf{T}}_n(t^*) - \bar{\mathbf{T}}^{tr} + \Delta t \sum_{\alpha} \dot{\gamma}^{\alpha}(\bar{\mathbf{T}}_n(t^*))\mathbf{C}^{\alpha}\right], \tag{4.23}$$

and $\mathcal{F}$ is the derivative of $\mathbf{W}_n$, with respect to $\bar{\mathbf{T}}_n(t^*)$:

$$\mathcal{F} = \mathcal{I} + \Delta t \left[\sum_{\alpha} \mathbf{C}^{\alpha} \otimes \frac{\partial \dot{\gamma}^{\alpha}}{\partial \bar{\mathbf{T}}_n(t^*)}\right]. \tag{4.24}$$

Here $\mathcal{I}$ is 6 by 6 identity matrix. In Eqn. 4.23 the $\mathbf{W}_n$ column vector has the same format as the $\mathbf{Z}$ vector, and in Eqn. 4.24 the tensors $\bar{\mathbf{T}}_n$ and $\mathbf{C}^{\alpha}$ are written as column vectors also.

In the proposed model, the plastic deformation on the octahedral planes is composed by the superkink part and the self-unlocking part, $\dot{\gamma}^{\alpha} = \dot{\gamma}_1^{\alpha} + \dot{\gamma}_2^{\alpha}$ for $\alpha = 1 \sim 12$.

For the superkink-unlocking part $\dot{\gamma}_1^\alpha$, due to the complicated underlying mechanisms, the partial derivative term, $\frac{\partial \dot{\gamma}_1{}^\alpha(\bar{\mathbf{T}}_n(t^*))}{\partial \bar{\mathbf{T}}_n(t^*)}$, can not be explicitly expressed. Thus, a numerical difference,

$$\frac{\Delta \dot{\gamma}_1{}^\alpha}{\Delta \bar{\mathbf{T}}_n} = \frac{\Delta \dot{\gamma}_1{}^\alpha}{\Delta \tau^\alpha} \mathbf{S}^\alpha,$$

is calculated instead, based on a stress difference of $\Delta \bar{\mathbf{T}}_n = 0.1\% \bar{\mathbf{T}}_n$. For the case of $\Delta \tau^\alpha = 0$, the corresponding numerical difference component is taken to be zero.

For the self-unlocking part, according to Eqn. 3.34 and the definition for the dislocation velocity, the plastic strain rate can be rewritten as:

$$\dot{\gamma}_2^\alpha = \rho_{total}^\alpha b \int_{\theta_{critical}}^{\theta_{max}} P_\theta(\theta) v_0^{SU} \left(\frac{\tau^\alpha}{S_2(T)} \right)^{m_1} d\theta, \tag{4.25}$$

where $\theta_{critical}(\tau^\alpha)$ corresponds to the strongest IKW that can be unlocked under the current applied stress. The derivative of the above equation corresponding to the stress is:

$$\begin{aligned} \frac{\partial \dot{\gamma}_2^\alpha}{\partial \tau^\alpha} &= \rho_{total}^\alpha b \int_{\theta_{critical}}^{\theta_{max}} P_\theta(\theta) \frac{m_1}{S_2(T)} v_0^{SU} \left(\frac{\tau^\alpha(\theta, \gamma_o, \gamma_c)}{S_2(T)} \right)^{m_1 - 1} d\theta \\ &- P_\theta(\theta_{critical}) \left[\frac{\tau^\alpha}{S_2(T)} \right]_{\theta_{critical}}^{m_1} \frac{\partial \theta_{critical}}{\partial \tau^\alpha}, \end{aligned}$$

and

$$\frac{\partial \dot{\gamma}_2^\alpha}{\partial \bar{\mathbf{T}}} = \frac{\partial \dot{\gamma}_2^\alpha}{\partial \tau^\alpha} \mathbf{S}^\alpha$$

In Figure 4-2, a one-dimensional form of Eqn. 4.20 is schematically illustrated. Function $W(\bar{\mathbf{T}}(t^*))$ is composed with two parts, a linear one $\left[\bar{\mathbf{T}}(t^*) - \bar{\mathbf{T}}^{tr} \right]$ and a nonlinear one $\sum_\alpha \dot{\gamma}^\alpha(\bar{\mathbf{T}}_n(t^*)) \mathbf{C}^\alpha$. Since this material is very strain-rate independent, the value of the nonlinear part is nearly zero until $\bar{\mathbf{T}}(t^*)$ is very close to the solution, and then quickly jumps up. Besides, the non-linear part, which actually represents the nonlinear relation of plastic strain and the applied stress, is only physically valid for a certain stress range. The applied stress can not make the unlocking activation enthalpy in Eqn 3.17 negative, and it can not make the resolved shear stress components in the cube planes larger than the slip-resistance $S_1(T)$ in Eqn. 3.39. When the current guess ($\bar{\mathbf{T}}_n(t^*)$) is smaller than the solution, since the nonlinear components does not contribute too much until very close to the solution, the slope at the current guess should be nearly the slope of the linear part, which is 1 in the one-dimensional case. Therefore, strict application of a Newton update $\bar{\mathbf{T}}_{n+1}(t^*)$ is very likely to be larger than the critical value of stress which makes Eqns 3.17 and 3.39 physically invalid. Moreover, in that case, the exponential term in Eqn. 3.17 will generate extremely large values which will make the iteration fail numerically.

In order to make a stable numerical solution and increase the convergence speed, the damped Newton method is applied. At the end of each iteration step, the value of stress for the next iteration $\bar{\mathbf{T}}_{n+1}(t^*) = \bar{\mathbf{T}}_n(t^*) + \Delta\bar{\mathbf{T}}_n(t^*)$ will be checked to see whether the stress is in the physically valid range. If not, the increment $\Delta\bar{\mathbf{T}}_n(t^*)$ will be modified to be half to its current value, and then a new $\bar{\mathbf{T}}_{n+1}(t^*)$ is calculated. This damping loop will continue until $\bar{\mathbf{T}}_{n+1}(t^*)$ makes each equation physically valid, and the next Newton iteration loop will begin.

The above analysis is based on simplified one-dimensional model. Since $\bar{\mathbf{T}}$ is a 6-vector, when using the proportional damping Newton method illustrated above, it is possible that part of the components in $\bar{\mathbf{T}}$ are getting smaller but others are actually getting larger. In that case, it is possible that the modulus of the $\bar{\mathbf{T}}$-vector gets smaller, but the resolved stress components always exceed the critical value, making Eqns. 3.17 and 3.39 invalid. The damping method fails in this situation. Thus, the number of damping loops is limited by a maximum number $n_{max} = 10$. If, after n_{max} loops, the estimated $\bar{\mathbf{T}}_{n+1}(t^*)$ still causes breakdown in Eqns 3.17 or 3.39, the current Newton iteration will be terminated, and the time increment will be justified.

As we analyzed above, due to the special shape of function $\mathbf{W}$ and the damping method, the Newton iteration does not depend too much on the initial value of $\bar{\mathbf{T}}_0$, unless it is very close to the solution. In the simulation, the initial guess of the stress at time t^* is given as:

$$\bar{\mathbf{T}}_{n=0}(t^*) = \bar{\mathbf{T}}(t). \tag{4.26}$$

After the iterative solution is found to converge to within a small tolerance $(0.01Pa)$ for the set of non-linear equations, the state is updated. The plastic deformation gradient at time t^* is updated using Eq. 4.11, and the elastic deformation gradient is calculated by using Eq. 4.1 and inverting the plastic deformation gradient. Once the elastic deformation gradient at time t^* is obtained, the Cauchy stress at time t^* is calculated through Eq. 4.8, and the crystallographic orientations are updated through Eq. 4.5.

4.3 Calculation of the Material Jacobian

After integration of the material state is completed, the material Jacobian matrix must be calculated for an implicit time-integration procedure. The Jacobian is needed to achieve an accurate correction to the incremental kinematics In the formulation of the element, the material Jacobian matrix $\mathcal{C}$ represents the change in the (increment of) Cauchy Stress $\mathbf{T}(t^*)$ with respect to a virtual change in relative strain tensor $\mathbf{E}^t(t^*)$,

$$\mathcal{C} \equiv \frac{\partial \mathbf{T}(t^*)}{\partial \mathbf{E}^t(t^*)}, \tag{4.27}$$

and

$$\mathbf{E}^t(t^*) \equiv ln(\mathbf{U}^t(t^*)), \tag{4.28}$$

where $\mathbf{U}^t(t^*)$ is the relative stretch tensor. The relative stretch tensor is evaluated from the polar decomposition of the relative deformation gradient, $\mathbf{F}^t(t^*)$, such that:

$$\mathbf{F}^t(t^*) = \mathbf{R}^t(t^*)\mathbf{U}^t(t^*). \tag{4.29}$$

The relative deformation gradient is determined by the following expression:

$$\mathbf{F}^t(t^*) = \mathbf{F}(t^*)\mathbf{F}^{-1}(t). \tag{4.30}$$

For small changes in the deformation gradient over the time increment, the relationship between $\mathbf{E}^t(t^*)$ and $\mathbf{U}^t(t^*)$ can be approximated by:

$$\mathbf{E}^t(t^*) \doteq \mathbf{U}^t(t^*) - \mathbf{I}_2. \tag{4.31}$$

Differentiating this equation, the following result is obtained:

$$d\mathbf{E}^t(t^*) \doteq d\mathbf{U}^t(t^*). \tag{4.32}$$

Therefore, the material jacobian can be approximated by:

$$\mathcal{C} \doteq \frac{\partial \mathbf{T}(t^*)}{\partial \mathbf{U}^t(t^*)}. \tag{4.33}$$

For simplicity, indicial notation will be used to develop the equations associated with the derivation of the material jacobian. Inversion of Eqn. 4.8 takes the form:

$$T_{ij} = [det(\mathbf{F}^e)]^{-1}(F^e_{im}\bar{T}_{mn}F^e_{jn}). \tag{4.34}$$

Taking the partial derivative of the Cauchy stress with respect to the relative stretch tensor leads to

$$\begin{aligned}\frac{\partial T_{ij}}{\partial U^t_{kl}} \; = \; & [det(\mathbf{F}^e)]^{-1}[\mathcal{S}_{imkl}\bar{T}_{mn}F^e_{jn} + F^e_{im}\mathcal{Q}_{mnkl}F^e_{jn} + \\ & F^e_{im}\bar{T}_{mn}\mathcal{S}_{jnkl} - F^e_{im}\bar{T}_{mn}F^e_{jn}(F^{e-1}_{qp}\mathcal{S}_{pqkl})],\end{aligned} \tag{4.35}$$

where

$$\mathcal{S}_{ijkl} \equiv \frac{\partial F^e_{ij}}{\partial U^t_{kl}}, \tag{4.36}$$

and

$$\mathcal{Q}_{ijkl} \equiv \frac{\partial \bar{T}_{ij}}{\partial U^t_{kl}}. \tag{4.37}$$

From a combination of Eqs. 4.1, 4.28, 4.29 and 4.12, the elastic deformation is approximated by the following expression:

$$F^e_{ij}(t^*) \doteq R^t_{ik}(t^*)U^t_{kl}(t^*)F^e_{lm}(t)[\delta_{mj} - \sum_{\alpha} \dot{\gamma}^\alpha(t^*)\Delta t S^\alpha_{mj}]. \tag{4.38}$$

Differentiation of Eq. 4.38 with respect to the relative stretch tensor yields

$$\begin{aligned} \mathcal{S}_{ijkl} \doteq\ & R^t_{ik}(t^*)F^e_{lj}(t) - R^t_{ik}(t^*)F^e_{lm}(t)\sum_{\alpha} \dot{\gamma}^\alpha(t^*)\Delta t S^\alpha_{mj} - \\ & R^t_{in}(t^*)U^t_{np}(t^*)F^e_{pm}(t)\sum_{\alpha} J^\alpha_{kl}\Delta t S^\alpha_{mj}, \end{aligned} \tag{4.39}$$

where

$$\mathbf{J}^\alpha \equiv \frac{\partial \dot{\gamma}^\alpha(t^*)}{\partial \mathbf{U}^t(t^*)}. \tag{4.40}$$

The partial derivative of the second Piola-Kirchhoff stress with respect to the relative stretch tensor can be found by differentiating Eqn. 4.15. The result of that operation is:

$$\mathcal{Q}_{ijkl} = \mathcal{D}_{ijkl} - \Delta t \sum_{\alpha} C^\alpha_{ij} J^\alpha_{kl} - \Delta t \sum_{\alpha} \dot{\gamma}^\alpha \mathcal{J}^\alpha_{ijkl}, \tag{4.41}$$

where

$$\mathcal{D}_{ijkl} = \frac{1}{2}\mathcal{L}_{ijmn}\varepsilon_{mnkl}, \tag{4.42}$$

$$\mathcal{J}_{ijkl} = \frac{1}{2}\mathcal{L}_{ijmn}[\varepsilon_{mpkl}S^\alpha_{pn} + \varepsilon_{pnkl}S^\alpha_{pm}], \tag{4.43}$$

and

$$\varepsilon_{ijkl} = F^e_{ki}(t)U^t_{lm}F^e_{mj}(t) + F^e_{mi}(t)U^t_{mk}F^e_{lj}(t). \tag{4.44}$$

To complete the set of equations necessary to determine the material jacobian, an analytical form for $\mathbf{J}^\alpha$ must be found. The crystallographically-resolved plastic strain rate is a function of the second Piola-Kirchhoff stress and the crystallographic dislocation density state; therefore, $\mathbf{J}^\alpha$ can be written as

$$J^\alpha_{ij} = \frac{\partial \dot{\gamma}^\alpha}{\partial \bar{T}_{kl}} \frac{\partial \bar{T}_{kl}}{\partial U^t_{ij}}. \tag{4.45}$$

Letting

$$M^\alpha_{kl} \equiv \frac{\partial \dot{\gamma}^\alpha}{\partial \bar{T}_{kl}}, \tag{4.46}$$

Eqn. 4.45 yields:

$$J^\alpha_{ij} = M^\alpha_{kl} \mathcal{Q}_{klij}. \tag{4.47}$$

Substitution of this result into Eqn. 4.41 and solving for $\mathcal{Q}_{ijkl}$ leads to the final expression:

$$\mathcal{Q}_{ijkl} = \left[\delta_{im}\delta_{jn} + \Delta t \sum_\alpha M^\alpha_{mn} C^\alpha_{ij} \right]^{-1} \left[\mathcal{D}_{mnkl} - \Delta t \sum_\alpha N^\alpha_{mn} C^\alpha_{kl} - \Delta t \sum_\alpha \dot{\gamma}^\alpha \mathcal{J}^\alpha_{mnkl} \right]. \tag{4.48}$$

The analytical expression for the material jacobian is an approximate solution, but the level of error is the same as the level of error in calculating the Cauchy stress and the dislocation density state at time t^* as a result of the Taylor expansions that were used to simplify the calculation.

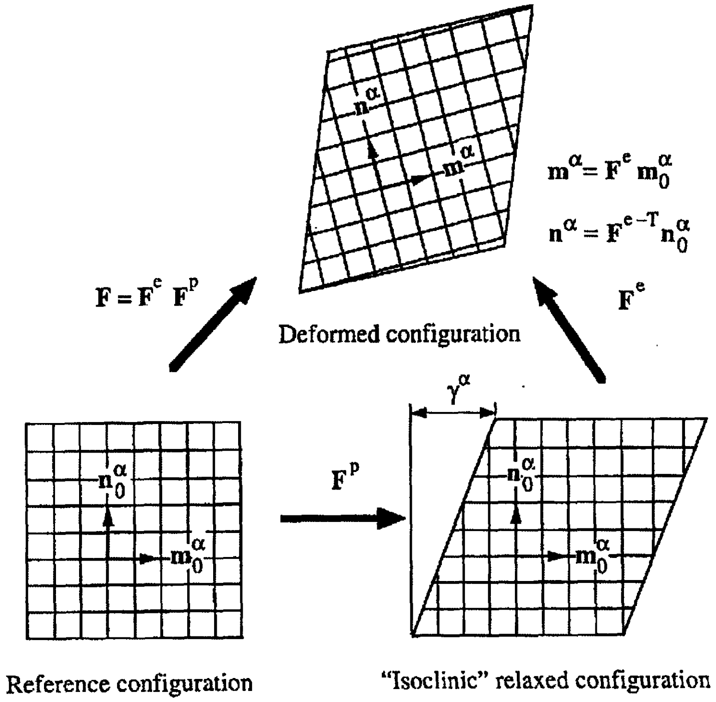

Figure 4-1: Schematic diagram showing the multiplicative decomposition of $\mathbf{F} = \mathbf{F}^e\mathbf{F}^p$.

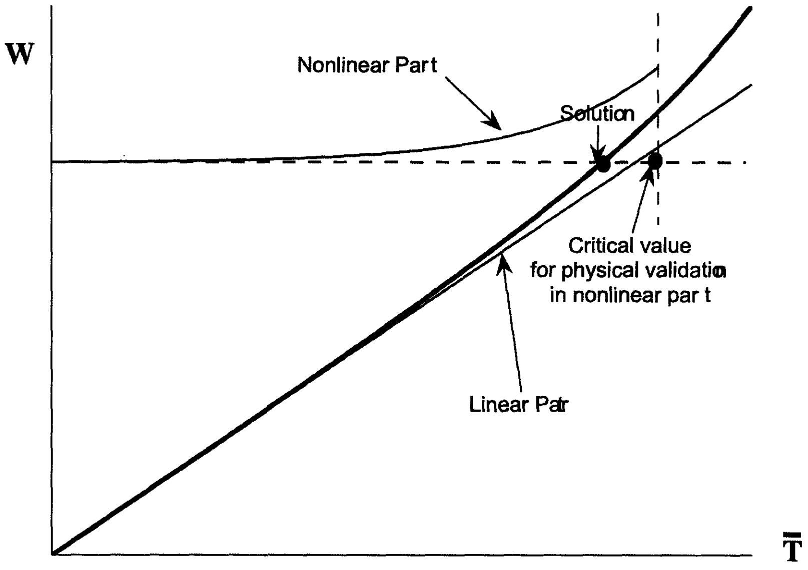

Figure 4-2: Illustration of the one dimensional-form of Eqn. 4.20

Chapter 5

Simulation Results and Discussions

The constitutive model developed in Chapter 3 has been implemented into the finite element solver described in Chapter 4. Major equations of the model have been summarized in Appendix A. The simulation geometry used was a unit cube cell, which is assigned to be a brick (C3D8R) element (Figure 5-1). General periodic boundary conditions [59] are imposed on the unit cell, and the cell is deformed under uni-axial (in the 3-direction) loading conditions.

5.1 Selection of Material Constants

The elastic moduli for Ni_3Al used in the simulations are adapted from experimental data. In Tanaka 's paper [58], the temperature-dependence of C_{44} was measured and specified, and the Zener elastic anisotropy factor $A \equiv 2C_{44}/(C_{11} - C_{12})$ was found to be nearly temperature-independent. He did not present test data for C_{11} and C_{12}, but C_{12} was found to be less temperature-dependent than C_{11}. Here, we choose C_{12} as a constant ($148GPa$ [46]) and derive C_{11} by applying the test data for C_{44} and assuming A as a constant with the value equal to 3.3 [34]. The elastic moduli are then defined by the following equations:

$$\begin{aligned} C_{11} &= (230 - 0.0194 \times T)GPa; \\ C_{12} &= 148GPa; \end{aligned}$$

$$\begin{aligned} C_{44} &= (135 - 0.032 \times T)GPa; \\ \mu &\equiv \sqrt{\frac{C_{44}(C_{11} - C_{12})}{2}}. \end{aligned}$$

Other material parameters are listed in Table 5-1:

Table 5.1: Material parameters for Ni_3Al

Parameter	Value	Reference
b (m)	2.5×10^{-10}	[34]
$\gamma_c(Jm^{-2})$	0.144	[66]
$\gamma_o(Jm^{-2})$	0.180	[66]
$\rho^{\alpha}_{total}(m^{-2})$	10^{12}	[48]
A	3.3	[34]

The value of Burgers vector is for the $1/2[\bar{1}01]$ superpartials. The value of ρ^{α}_{total} given by Viguier, *et al.* is an estimation of the total screw dislocation density for one active octahedral-slip-system, at the beginning of plastic deformation. This value is derived from the test data of dislocation density for different plastic strain offsets in a [123]-loading (a single-slip uniaxial stressing orientation) compression tests.

The fitting material parameters are listed in the Table 5-2. Since a formal parameter optimization has not been performed, these parameters may not be the "best" choice, and a parameter sensitivity study will be presented in section 5.3.

5.2 Simulation Results and Discussions

5.2.1 Summary of Simulation Results of the Macro-mechanical Properties

Simulations of uni-axial compression tests for Ni_3Al single crystal with a constant applied strain-rate of $10^{-4}s^{-1}$ were carried out for a temperature range from 300K to 1100K, in three crystal orientations. Temperature-dependence of the simulated

Table 5.2: Fitting material parameters for Ni_3Al

Parameter	Value	Equation
$\dot{\gamma}_0$ (s^{-1})	10^{-2}	Eqn. A.6 (b)
$\bar{n}$	10	Eqn. A.9
σ_n	1	Eqn. A.9
σ_θ (degree)	3	Eqn. A.13
H_{u0}(e.v.)	0.3	Eqn. A.11
v_0^{SK}(m/s)	10^{-2}	Eqn. A.10
v_0^{SU}(m/s)	10^{-3}	Eqn. A.16
m_1	20	Eqn.s A.6 (b), A.16
m_2	3	Eqn. A.19
S_d(MPa)	800	Eqn. A.19
C_ρ	0.02	Eqn. A.21
$R(m)$	$2.5 \times 10^{-9}(10b)$	Eqn. A.21

yield strength (measured at 0.2% offset strain) and hardening rate is presented in Figures 5-2 and 5-3, together with the experimental data given by Bontemps-Neveu [1] [17]. The simulation results successfully capture the temperature-dependence of yield strength and the hardening rate. They both increase with increasing temperature until a peak temperature is reached, and then drop off. For a given orientation, the peak temperature for hardening rate, $T_{p,h}$, is always lower than the peak temperature for the yield strength, $T_{p,\sigma}$. The simulated uni-axial stress-strain curves for the $[\bar{1}11]$ and the [001] orientations are also presented in Figures 5-4 and 5-5.

Simulation results of compression tests in the [001] orientation at 500K with two different applied uniaxial strain-rates ($10^{-3}s^{-1}$ and $10^{-4}s^{-1}$, respectively) are plotted in Figure 5-6. The yield strength shows a very weak positive dependence on the applied strain-rate. An increase of $2.5MPa$, which is approximately 1.3% of $|\sigma_y|$ is observed for a 10-times increase in applied strain-rate, and the simulated hardening rate is nearly strain-rate independent, similar to the experimental results.

---

[1] It needs to make clear that, in Bontemps-Neveu's thesis, the hardening rate was marked as $d\tau/d\gamma$, but according to his experimental stress-strain curves, the hardening rate he measured was actually the average slope of the uniaxial true-stress/true-strain curves ($\Delta\sigma/\Delta\epsilon$).

The non-Schmid effects of yield strength were also studied. Figure 5-7 illustrates that for the [001] orientation, tension strength is higher than the compression strength. For the other two orientations ([$\bar{1}$11] and [123]), compression strength is higher than that of tension.

We presented above the simulation results of the major macro-mechanical features of plastic deformation in Ni_3Al single crystals. However, the objective of the study in mechanism-based modeling and simulation is far beyond matching and predicting macro-mechanical properties. Other information achieved from the numerical simulations, including the evolution of different internal variables and the parameter sensitivity study, is also necessary in order to understand and evaluate the underlying mechanisms, and needs full discussion.

5.2.2 Mechanical Properties of Yield Strength

In the simulations, the anomalous temperature-dependence of yield strength is essentially governed by the superkink-unlocking mechanism. The self-unlocking mechanism mainly acts to reduce the hardening rate in the temperature range from $T_{p,h}$ to $T_{p,\sigma}$. The major consideration corresponding to the above statement is the small strain-rate sensitivity. In the self-unlocking mechanism, as proposed by Caillard, the rate of dislocation dynamics is controlled by the slow gliding on the cube planes. That is why Eqns. A.6(b) and A.16 have similar power-law forms, both of which are modeled as strain-rate dependent.

Similar to all other superkink models, the yield strength anomaly is achieved through the systematic decrease of superkink height with increasing temperature. Since the activation volume in Eqn. A.11 is very large ($\sim 10^2 b^3$), for each time step, only those longest superkinks can be activated and move. This is clearly illustrated in Figure 5-8, in which the screw distribution and the plastic contribution, $\rho^{\alpha}_{screw}(l) b P^{\alpha}_{screw} v^{\alpha}(l, \tau^{\alpha})$, of one of the active slip-systems are plotted vs. l. The data were extracted from the simulation of [001]-axial compression at 500K, at a plastic strain offset of $\epsilon_p = 0.3\%$. Since only the screws possessing the longest superkinks can move, the yield strength is then roughly inversely related to l_{max}, which monotonically decreases with rising temperatures, as shown in Figure 3-3.

A large value of activation volume V is also necessary for the property of small strain-rate sensitivity. Since the plastic contribution comes from screws with the longest superkink height very close to l_{max}, Eqn. A.8 can be rewritten as:

$$\dot{\gamma}_1^{\alpha} = C_{int}\rho_{total}^{\alpha} b P_{screw}(l_{max}) v_0^{SK} \exp\left(-\frac{H_u(l_{max}, \tau^{\alpha})}{kT}\right), \tag{5.1}$$

where C_{int} is a dimensionless factor replacing the integration operator, which takes into account the fact that screws with superkink heights slightly shorter than l_{max} also contribute to the plastic deformation. The above equation can be rewritten in the simplified form:

$$\dot{\gamma}_1^{\alpha} = C \exp\left(A + B\tau^{\alpha}\right), \tag{5.2}$$

where

$$C = C_{int}\rho_{total}^{\alpha} b P_{screw}(l_{max}) v_0^{SK}, \quad \text{and} \quad B = \frac{V}{kT} = \frac{3.5(l_{max}/b)b^3}{kT}. \tag{5.3}$$

A typical $L1_2$ crystal is nearly strain-rate independent, and the change of yield strength is less than 1% for a factor of 10 change in applied strain rate. Numerically, if τ^{α} does not change too much, according to Eqn. 5.3, the factor C should not vary much either. Thus, in order to account for a nearly strain-rate independent property, the value of the exponential term, $\exp(A + B\tau^{\alpha})$, must be very sensitive to a small change in τ^{α}. Let $\dot{\gamma}_{app[1]}$ and $\dot{\gamma}_{app[2]}$ two different applied strain-rates, with $\dot{\gamma}_{app[1]} = 10\dot{\gamma}_{app[2]}$. Since hardening is also nearly strain-rate independent, we can reasonably assume that the ratio of the plastic strain-rate under these two conditions is roughly 10:

$$\frac{\dot{\gamma}_{1[1]}^{\alpha}}{\dot{\gamma}_{1[2]}^{\alpha}} = \frac{C \exp\left(A + B\tau_{[1]}^{\alpha}\right)}{C \exp\left(A + B\tau_{[2]}^{\alpha}\right)} = 10 \Rightarrow \exp\left(B(\tau_{[1]}^{\alpha} - \tau_{[2]}^{\alpha})\right) = 10. \tag{5.4}$$

Generally, the critical resolved shear stress is of the order of $10^2 MPa$. Thus, to make a stress change, $(\tau_{[1]}^{\alpha} - \tau_{[2]}^{\alpha})$, less than 1% ($\sim 1MPa$), the value of l_{max}/b defining B in Eq. 5.3. has to be of the order of 10^2.

In this simulation, we did not account for possible temperature-dependence of the resistance forces for the superkinks. The Hirsch-version of unlocking enthalpy implemented in the simulation was derived based on a very weak IKW configuration, with the cross-slipped APB width $w \sim b$. Hirsch assumed that the jogs on the cube plane can move freely, and thus did not consider the effects of jog resistance at the ends of superkinks, nor did he consider the effects of the temperature-dependence of w, which is certainly under question. If we do consider the jog resistances, and assume the height of the cross-slipped jogs on the cube plane increases with increasing temperature, as we did while implementing the self-unlocking mechanism, there should be a term in the superknink unlocking enthalpy in Eqn. A.11 reflecting the strength of the IKWs, defined by the distribution of cube APB extent w (or of θ). The plastic strain-rate corresponding to the superkink unlocking mechanism could then be revised into a double integration form over both l and θ:

$$\dot{\gamma}_{1R}^{\alpha} = \rho_{total}^{\alpha} b \int_0^{l_{max}^{\alpha}} \int_0^{\theta_{max}} P_\theta(\theta) P_{screw}^{\alpha}(l) v^{\alpha}(l, \tau^{\alpha}, \theta) d\theta dl, \tag{5.5}$$

where

$$v^{\alpha}(l, \tau^{\alpha}, \theta) = v_0^{SK} \exp\left(-\frac{H_{u0}(\theta) - V(l)\tau^{\alpha}}{kT}\right). \tag{5.6}$$

Eqn. 5.5 is integrated and the strain-rate vs. stress relation is plotted in Figure 5-9. Due to the two independent distributions we applied for l and θ, this $\dot{\gamma}_1$-τ^{α} relation is obviously strain-rate dependent. This is the reason that we did not include the θ-dependence of the resistance forces into the superkink unlocking mechanism. A more complex model perhaps could be derived through systematic, mechanistic coupling of l and θ distribution.

The total dislocation density ρ_{total}^{α} is assumed constant in the simulation. Dislocation density was measured for the single slip plane with loading in [123] orientation at 373K, and ρ_{total} was reported to increase from $2.5 \times 10^{12} m^{-2}$ after 1% resolved plastic strain to $17 \times 10^{12} m^{-2}$ after 6% resolved plastic strain [60]. Since the material is nearly strain-rate independent, governed by the exponential part in Eqn. A.10, the changes of total dislocation density should not affect the simulation results significantly, and for this reason any such changes have been neglected in the simulations.

The simulation results successfully captured the temperature-dependence of yield strength, and the predicted peak temperatures for maximum yield strength are the same as in the experimental results ($T_{p,\sigma}$ is equal to 700K, 900K and 1000K, respectively, for the corresponding orientations: $[\bar{1}11]$, [123], and [001]). The temperature-dependence of yield strength and strain-hardening rate have been plotted, together with the plastic contribution from different mechanisms for these three simulated orientations, as shown in Figures 5-10, 5-11, and 5-12. It is clearly illustrated that for the $[\bar{1}11]$ (Figure 5-10) and [123] (Figure 5-11) orientations, the temperature of peak yield strength, $T_{p,\sigma}$, is the same temperature that the cube slip starts to dominate the plastic deformation. $T_{p,\sigma}$ has been observed to be the lowest for the $[\bar{1}11]$ orientation in many experimental works [8, 17]. It has usually been explained by noting that the maximum Schmid factor on a cube plane (S_{cb}) was the highest in the $[\bar{1}11]$ orientation. However, the values of S_{cb} for the $[\bar{1}11]$ and [123] orientations are very close (0.4722 and 0.4546, respectively), but the peak temperature $T_{p,\sigma}$ differs significantly for these two orientations (700K and 900K, respectively). In fact, the main reason for the big difference in $T_{p,\sigma}$, is the different ratio of the maximum Schmid factor on the cube plane to that on the octahedral plane S_{cb}/S_{pb}, which is 1.7489 for the $[\bar{1}11]$ orientation and 1.026 for the [123] orientation. Since S_{pb} for $[\bar{1}11]$ is much smaller than that for [123], at the same temperature, the uni-axial stress level is much larger in the former orientation than in the latter one. Thus the cube resolved shear stress is much larger for $[\bar{1}11]$ than for [123], even though they have similar Schmid factors on the cube plane. Another less important reason for the difference in $T_{p,\sigma}$ is that the $[\bar{1}11]$-axial loading has three active cube slip systems out of the six cube slip-systems considered, but the [123] orientation only has two.

Since the Schmid factor on the cube planes for [001]-axial loading is zero, cube slip is never activated for this orientation. The decrease of yield strength in this orientation at $1100K$ is due to the activation of the diffusion mechanism. Simulations with two different applied strain-rates were carried out for [001] compression at $1100K$, and the results are plotted together with the experimental data in Figure 5-5(b). Similar to the test data, at the low applied strain-rate of $1.1 \times 10^{-4}s^{-1}$, a yield drop is obtained, due to the rapid increase of mobile dislocation density. The plastic strain-rates of the diffusion mechanism and the evolution of the mobile dislocation density are plotted in Figure 5-13. At the high applied strain-rate of $2.2 \times 10^{-3}s^{-1}$, the simulation results shows a normal hardening. This is because the strain-rate is too rapid for the diffusion mechanism to provide a sufficient dislocation flux, and the stress level must be increased to continue to active the self-unlocking mechanism in order to sustain the dislocation flux. The plastic strain-rate of the diffusion mechanism and self-unlocking mechanism are plotted in Figure 5-14 for the high strain-rate simulation. The predicted yield strength at a strain offset larger than 2% for the "fast" loading condition is very close to the test data. However, the simulated high strain-rate curve shows an abrupt yield point, inconsistent with the gradual yielding behavior from a much lower stress level observed in the test (Figure 5-5(b)). A possible explanation is: in the superkink unlocking mechanism, we assume that locked screw segments are formed "at the very beginning of deformation" without detailed analysis. Considering that locking of screw dislocations is a temperature-dependent process, we implement a temperature-dependent θ-distribution as an initial condition, and the critical unlocking stress is calculated based on this θ-distribution. However, the process of forming an IKW with cross-slip distance w on the cube plane needs some time. At the very beginning of the deformation, there should be some just-cross-slipped K-W locks with very short w values (or high values in θ). These IKWs could be unlocked by a relatively low resolved shear stress. With further deformation, the configurations of existing K-W locks are getting closer to the initially-assumed θ distribution, and the critical unlocking stress is closer to the predicted value; thus a rounded yield point is to be expected.

The orientation-dependence and tension-compression asymmetry of yield strength are addressed by introduction of the factor of $\exp\left(S_{pe}^{\alpha}\right)$ defined in Eqn.3.4 for the initial value of l_{max}, as previously discussed in Chapter 3. Unlike the PPV-type lock configuration (shown in Figure 2.2 (b)), where the core of the leading superpartials extends on a cross-slipping octahedral plane, in our model, we consider a K-W lock configuration illustrated by Figure 1-4 (b), with the cores of the leading and trailing superpartials on parallel octahedral planes. Due to the different assumption of the locked configuration, we don't consider the effects of τ_{se}, which is the non-Schmid (edge) component on the cross-slipping octahedral planes, as the PPV model did. However, the proposed model nonetheless gives a prediction of tension-compression asymmetry similar to the PPV model. That is, for orientations in the unit crystal triangle close to the corner of [001], tensile strength is higher than compressive strength; for orientations at the other side of the triangle, the situation is reversed. This is because, the two terms that govern the non-Schmid effects, τ_{pe} (in the proposed model) and $\tau_{pe} - \kappa\tau_{se}$ (in PPV model, Eqn. 2.4) have similar orientation-dependence (for reasonable values of κ suggested in PPV model), as shown in Figure 5-15.

The $(\bar{1}11)[\bar{1}01]$ CRSS (at 0.2% offset strain) of the three simulated orientations is plotted in Figure 5-16. From the experimental data, we find that CRSS for $[\bar{1}11]$ axial loading is the highest, next is the CRSS for [123] loading, and the CRSS for [011] loading is the lowest. The simulation results roughly capture this trend, especially for the [123] and [001] orientations. For the [123] orientation over the temperature range of $500K - 700K$, the simulated CRSS is a little higher than experimental data. This error mainly comes from the mis-prediction in the hardening rate in this temperature range, because the yield strength is measured at $\epsilon^p = 0.2\%$, as it is for the experimental data. The predicted CRSS for the $[\bar{1}11]$ orientation is a little low, and very close to the prediction of [123]. This is because S_{pe} for these two orientations are very close, -0.1574 for $[\bar{1}11]$ and -0.1347 for [123]. Thus the initial value of l_{max} is very close for these two orientations, and similar values for initial CRSS follow.

As discussed above, following the idea of the PPV model, we tried to capture the non-Schmid effects of Ni_3Al basically by considering the effects of the non-Schmid stress components on the constriction-initiated cross-slip process. We have discussed some flaws of the PPV model in Chapter 2. Here, another point needs to be mentioned. If cross-slip is initiated by the constriction of the Shockley partials, it is not clear, when the non-Schmid component τ_{pe} is negative and expands the partials, what causes the constriction. It may be possible that the constriction starts from some local defects, but in that case, τ_{pe} should not affect the cross-slip as much as pointed by the PPV model. Recently, Martin, *et al.* [47] reported a large influence of the stacking fault energy γ_{CSF} on the yield strength. As shown in Figure 2-12, crystals with higher γ_{CSF} present higher strength. The explanation is, for higher values of γ_{CSF} , the core of Shockley partials is narrower, and is thus easier to cross-slip. This is a supportive observation for the constriction-initialed cross-slip process, while no details of what causes the constriction were specified.

5.2.3 Mechanisms and Mechanics of Hardening Rate

In the superkink-unlocking-mechanism-dominant regime, hardening is due to the continuing decrease of the longest superkink height with ongoing deformation. P_{screw} is plotted in Figure 5-17 (b) for different values of plastic strain ($|\epsilon_p| = 0 \Rightarrow |\epsilon_p| = 0.006$, with an increment of $\Delta\epsilon_p = 0.001$), for the [123]-axial compression at 400K and 500K, respectively. It is clear to see the decrease of l_{max} with plastic deformation, because the longest superkinks have been activated and redistributed.

We assume in this model, that as temperature increases, the initial value of l_{max} diminishes. Thus a similar absolute decrease in l_{max} will be a larger fraction of its initial value for the high-temperature condition than it is for the lower temperature. This is clearly illustrated by Figure 5-17 (b). Because l_{max} is much larger at 400K ($\sim$ 300b) than it is at 500K ($\sim$ 200b), for a plastic strain of $|\epsilon_p| = 0.006$, even the absolute change in l_{max} for 400K is larger than for 500K due to the "fatter" bell-shape of P_{screw} in 400K, l_{max} decreases by around 18% in 500K but only 15% at $400K$. Since the resolved shear strength is nearly inversely related to l_{max}, for the same plastic strain, we expect a larger increase in the yield strength at 500K than at 400K. Therefore the predicted hardening rate monotonically increases with increasing temperature, based on the proposed superkink unlocking mechanism alone.

The effect of the initial value of l_{max} is also one of the reasons why the simulated hardening rate is the lowest for the [001] orientation. For the same temperature, the initial value of l_{max} for [001] is the largest compared to the other two orientations. Based on the previous discussion, the percentage change in l_{max} is the smallest in [001] orientation, if the absolute change in l_{max} is similar for the three orientations. Moreover, for the same plastic deformation, the absolute change in l_{max} for [001]-compression should also be the smallest. The reason is that [001] is a highly symmetric orientation, and there are totally 8 active octahedral systems. In [001]-axial loading, the P_{screw} "tail" corresponding to the longest superkinks is "eaten up" less quickly than it is for the other two orientations. In Figure 5-18, the evolution of P_{screw} for simulations of compression at 400K in both [123] and [001] orientations has been plotted. The absolute change in l_{max} is clearly smaller in [001] than in [123] orientation. Experimental results show that the strain hardening rate is the highest for the $[\bar{1}11]$ orientation. However, the predicted hardening rate for the [123] orientation is higher than the other two orientations in the low-temperature regime, inconsistent with the test data. As we just discussed, this is because for a single slip orientation as [123], the P_{screw} "tail" is "eaten up" more quickly than in the multi-slip orientations.

As we have analyzed numerically, the superkink unlocking mechanism implemented in the simulation, which dominates the temperature range below $T_{p,h}$, can capture the anomalous temperature-dependence, and roughly capture the orientation-dependence of the hardening rate in this temperature range. The validity of the proposed superkink-based hardening mechanism needs further experimental verification. Currently, we assume slip-systems to be independent of each other. However, the interaction of slip-systems for some highly-symmetric orientations (e.g. [001]) might not be neglectable. Further consideration of multi-slip effects might improve the prediction in the orientation-dependence of the strain hardening rate.

The temperature corresponding to the peak hardening rate, $T_{p,h}$ is found to be smaller than the temperature of peak yield strength, $T_{p,\sigma}$ for all three orientations, with values of 600, 600 and 700K for the $[\bar{1}11]$, [123] and [001] orientations, respectively. The simulated results for $T_{p,h}$ differ somewhat from the test data, which have corresponding values of 500, 700 and 800K. The drop of the hardening rate with temperature for [123] and [001] orientations is due to the participation of the self-unlocking mechanism, as shown in Figures 5-11 and 5-12. For the $[\bar{1}11]$ orientation, the Schmid factor is only 0.27. Thus, even at the peak yield strength condition at 700K, the resolved shear stress in the octahedral plane is still not high enough to activate the self-unlocking mechanism. For this orientation, the drop of hardening rate is due to the participation of cube slip, as shown in Figure 5-10, and after the cube slip dominates, the yield strength starts to drop.

5.2.4 Flow Strength Reversibility

Many research groups [61, 62, and 63] have carried out so-called Cottrell-Stokes experiments and investigated the yield strength reversibility in $L1_2$ single crystals, but no reasonable explanation of this phenomena has yet been established. Among all of the experimental works, in the author's view, Dimiduk's work is the most impressive. Different from other groups, he did the experiments in the [001] orientation to minimize the effects of cube slip. And since [001]-loading is highly symmetric, the explanation that the yield reversibility is due to the activation of the secondary slip-system [64] is obviously incorrect. He also presented several TEM pictures to describe dislocation substructures in the deformed pre-strained sample, as shown in Figure 5-19. It is pointed out that both the high-T and low-T characteristic dislocation structures exist in the same sample (pre-strained at high-T followed by RT deformation). He then proposed that "some part of the substructure recovers extremely rapidly".

In the current study, we did not propose a way to explain the "extremely rapid recovery" of the dislocation substructure. But, at least, the proposed model is not in conflict with the observation. Since we assume that CRSS is basically determined by the longest superkink height, the yield strength is then governed by the low-T type substructure, which counts for the yield strength reversibility. Besides, since the density of low-T type dislocations is smaller in a high-T-pre-strained sample than that in a virgin sample, σ_y measured with a high-T-pre-strained sample is expected to be a little higher than that for a virgin sample, as experimentally observed.

5.3 Study of Parameter Sensitivity

As we have analyzed, the superkink unlocking mechanism dominates the temperature range below $T_{p,h}$, and due to the large activation volume assumed for the unlocking process, the yield strength is closely dependent on the height of longest superkinks. Therefore, the simulation results for this temperature range is very sensitive to the value of l_{max}.

We have modeled the initial value of l_{max} as depending on the assumed probability for longest superkinks, P_{min}, as shown in Figure 3-4. The larger P_{min} is, the smaller the initial value of l_{max}, and the yield strength is therefore higher. Simulations of the [123]-compression are carried out for both 400 and 500K, with different values of P_{min} of 10^{-3} and 10^{-4}, respectively. The simulations results are presented in Figure 5-20, and the yield strength is found to be very sensitive to the choice of P_{min}/l_{max}. The difference in the yield strength caused by different values of the P_{screw} distribution can be decreased by adjusting other parameters (e.g., H_{u0} in Eqn. A.11). However, if we assume Hirsch's version of unlocking enthalpy, even taking $H_{u0} = 0$, the yield strength predicted by applying $P_{min} = 10^{-3}$ is still much higher than the test data.

Similarly, the parameter q [2] in Eqn. 3.2 also affects the initial value of l_{max} (especially in the low-T region), as illustrated in Figure 5-21. At low temperature part, l_{max} responses greatly as q changes from 1 to 0.99, and is less sensitive as q getting smaller. In the simulation, we assumed $q = 0.99$.

We have shown in Chapter 3 that the screw distribution (P_{screw}) depends on the assumed average number of superkinks each screw ($\bar{n}$), but is insensitive to the assume standard deviation σ_n. Since the value of $\bar{n}$ changes the shape of P_{screw}, but does not affect the estimation of l_{max}, the yield strength should not be as sensitive to $\bar{n}$ as is the strain hardening rate. This has been illustrated in Figure 5-22, in which the simulated stress-strain curves of [123]-compression at 500K with different values of $\bar{n}$ are presented, together with the respective distributions of P_{screw}. If the value

---

[2] The parameter q in Eqn. 3.2 accounts for the fact that as the free screw segment gets less screw-orientated as it advances on the octahedral plane, the probability of locking gets smaller.

of $\bar{n}$ is increased, the bell-shape of P_{screw} will drift to the right (larger l). With the l_{max} unchanged, this causes a " fatter tail ". Thus, the hardening rate simulated with larger $\bar{n}$ is smaller, as more deformation is required to reduce l_{max}, and increase yield strength.

In the self-unlocking mechanism, θ_{mean} and the standard deviation, σ_θ, which govern the distribution of θ (Eqn. 3.32), are fitting parameters and are defined with the following considerations: The parameter θ describes the configuration of K-W locks. For the weakest IKWs with their APB ribbons cross-slipped on the cube plane only a very short distance ($\sim b/2$), θ is close to 55°. For the CKWs, $\theta = 0°$. It has been proposed (Chapter 2, Figure 2-11) that the weakest IKWs begin to be self-unlocked at the temperature of peak strain hardening rate, $T_{p,h}$. Therefore, weakest IKWs are considered to exist at temperatures around $T_{p,h}$. If we assume that θ follows the Gaussian distribution, based on the above statement, we consider the following two ways to model θ_{mean} and σ_θ: θ_{mean} decreases with temperature quickly and the value of σ_θ is large; or θ_{mean} barely decreases in the low-temperature region, and the value of σ_θ is small. For the first case, since σ_θ is relatively large, there are always some weak IKWs in the high-temperature part of the yield anomaly region. For the [001] orientation, the existence of these relatively weak IKWs means that they can get self-unlocked at a stress much lower than the experimental results, as shown in Figure 5-23. Therefore, in the simulation, we define θ_{mean} and σ_θ in the second way. (It is also possible that θ_{mean} decreases rapidly with temperature, as does σ_θ, which we did not consider in the research).

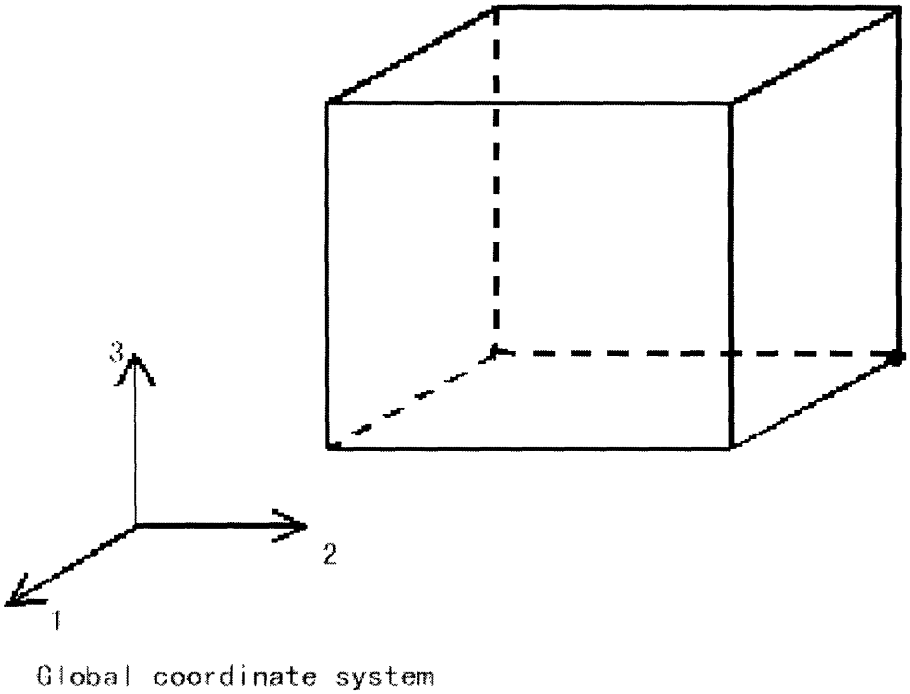

Figure 5-1: Simulation geometry

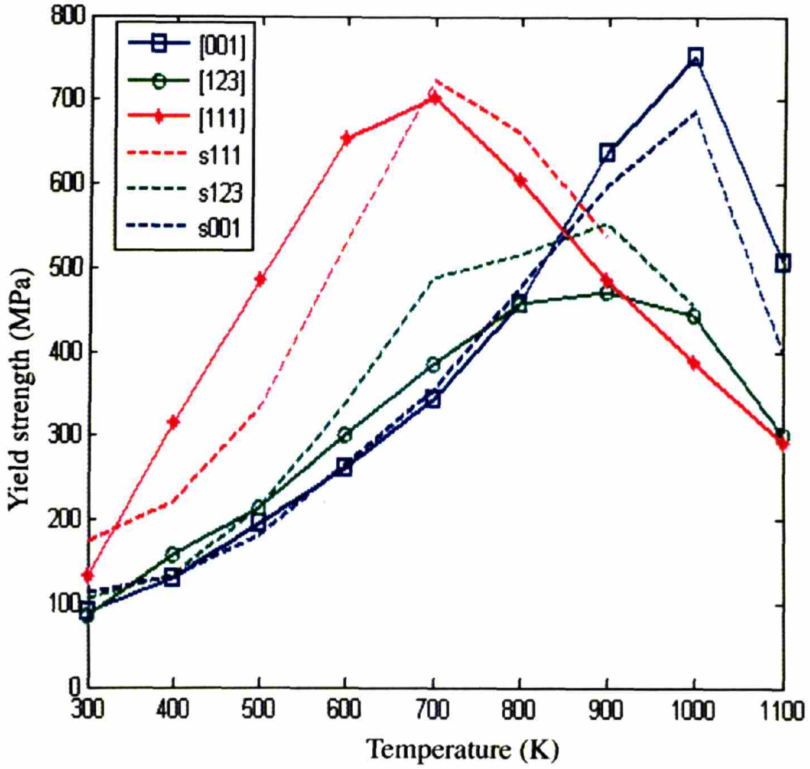

Figure 5-2: Temperature-dependence of yield strength for three orientations (red curves are for the $[\bar{1}11]$ orientation, green curves are for the [123] orientation and the blue curves are for the [001] orientation). The solid curves are test data from Bontemps-Neveu [17] (for $Ni_3(Al, 0.25at.\%Hf)$), and the dotted curves are from simulation.

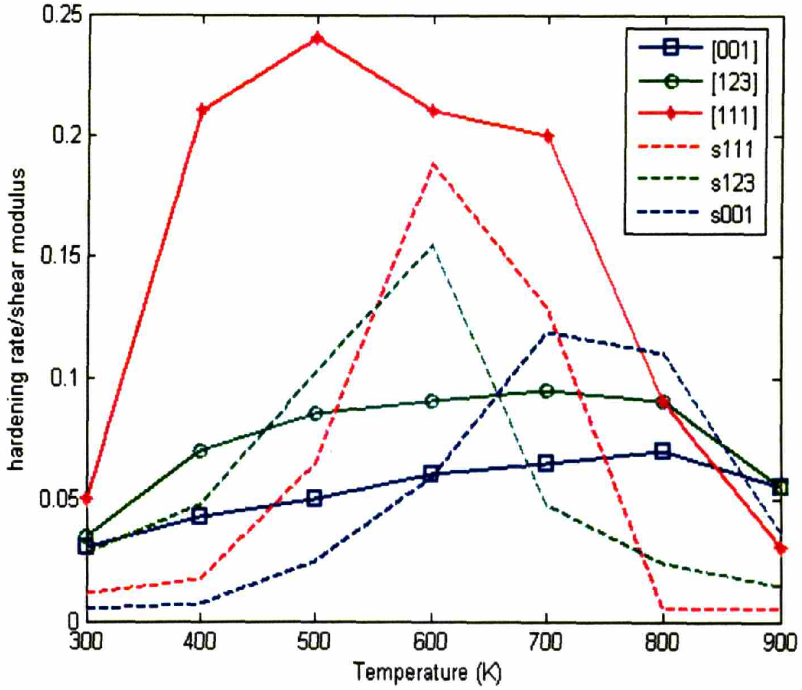

Figure 5-3: Temperature-dependence of hardening rate for three orientations (red curves are for the $[\bar{1}11]$ orientation, green curves are for the [123] orientation and the blue curves are for the [001] orientation). The solid curves are test data from Bontemps-Neveu [17] (for $Ni_3(Al, 0.25at.\%Hf)$), and the dotted curves are from simulation.

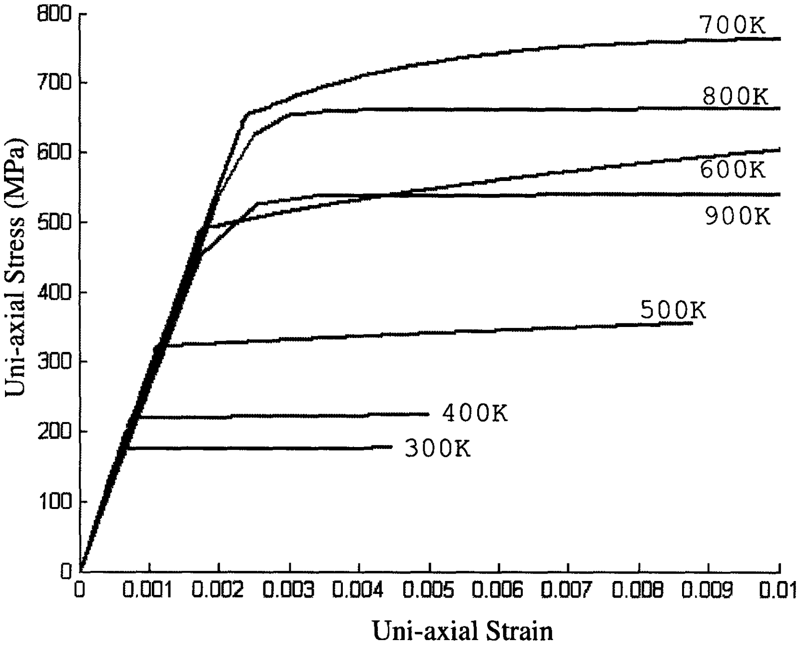

Figure 5-4: Simulated uni-axial stress-strain curves of $[\bar{1}11]$-compression with an applied strain-rate of $10^{-4}s^{-1}$ for different temperatures (300K ~ 1000K).

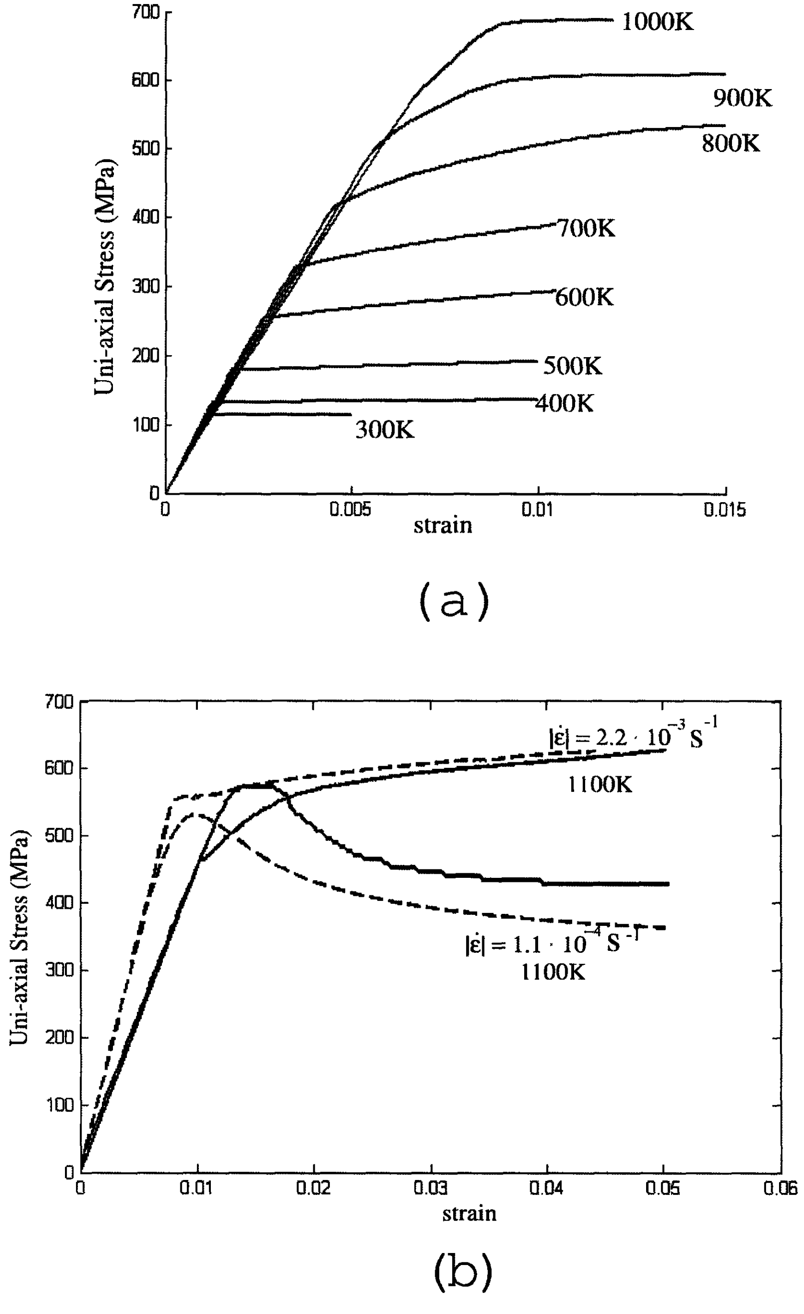

Figure 5-5: (a) Simulated uni-axial stress-strain curves of [001]-compression with an applied strain-rate of $10^{-4}s^{-1}$ for different temperatures (300K ~ 1000K). (b) Simulated (dotted) and test data [55] (solid) of uni-axial stress-strain curves of [001]-compression for $1100K$ with different applied strain-rates, $1.1 \times 10^{-4}s^{-1}$ and $2.2 \times 10^{-3}s^{-1}$, respectively.

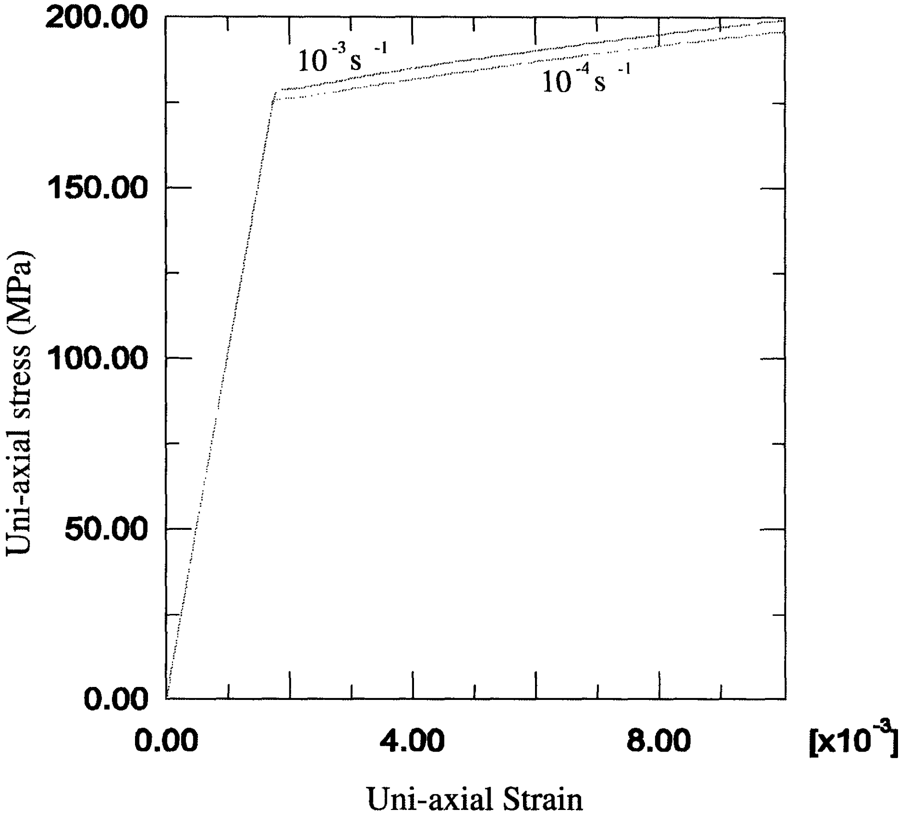

Figure 5-6: Strain-rate dependence test: simulation results of [001]-compression tests at 500K with two different applied strain-rates, $1.0 \times 10^{-4}s^{-1}$ and $1.0 \times 10^{-3}s^{-1}$, respectively. Both the yield strength and the hardening rate are nearly strain-rate independent.

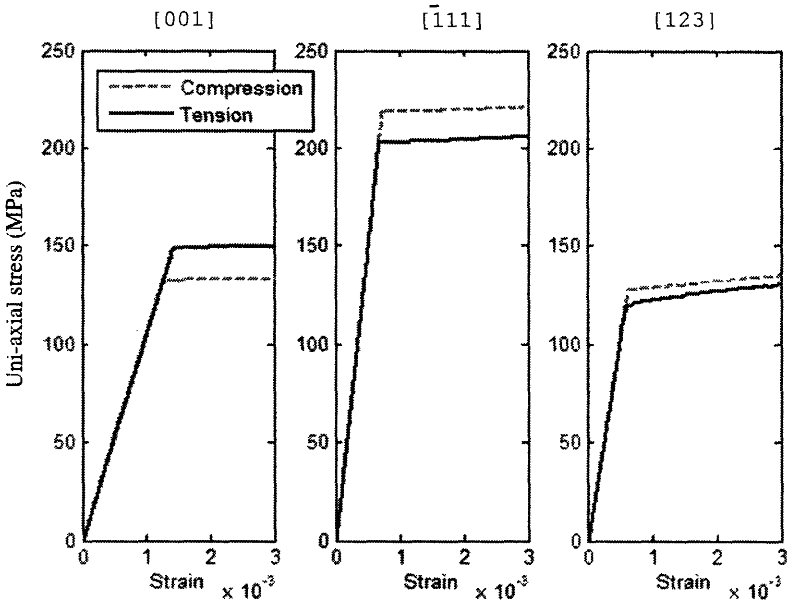

Figure 5-7: Orientation-dependence of yield strength: stress-strain curves of both tension and compression tests for the three orientations at 400K.

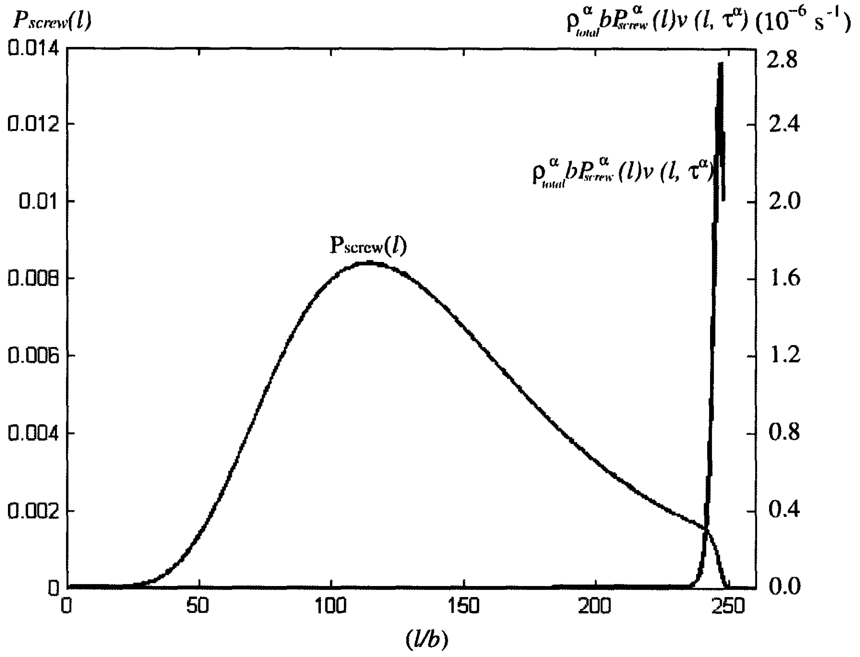

Figure 5-8: Illustration of the screw distribution ($P_{screw}(l)$) of one active slip system, and the plastic contribution of these screws, after compression in [001] to a plastic strain of $|\epsilon_p| = 0.3\%$ at 500K. The plastic contribution essentially comes from the movement of screws possessing very long superkinks (close to l_{max}).

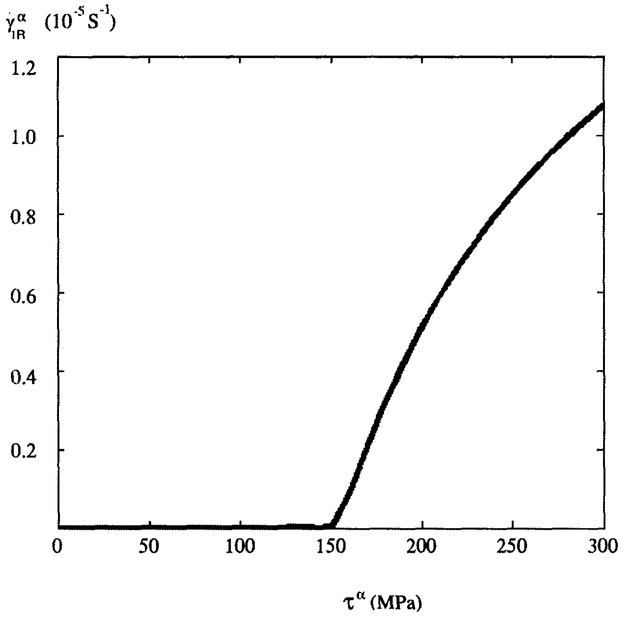

Figure 5-9: Illustration of the relation between the plastic strain rate (as defined by Eqn. 5.5) and the applied stress. The distributions in l and θ were assumed to be independent.

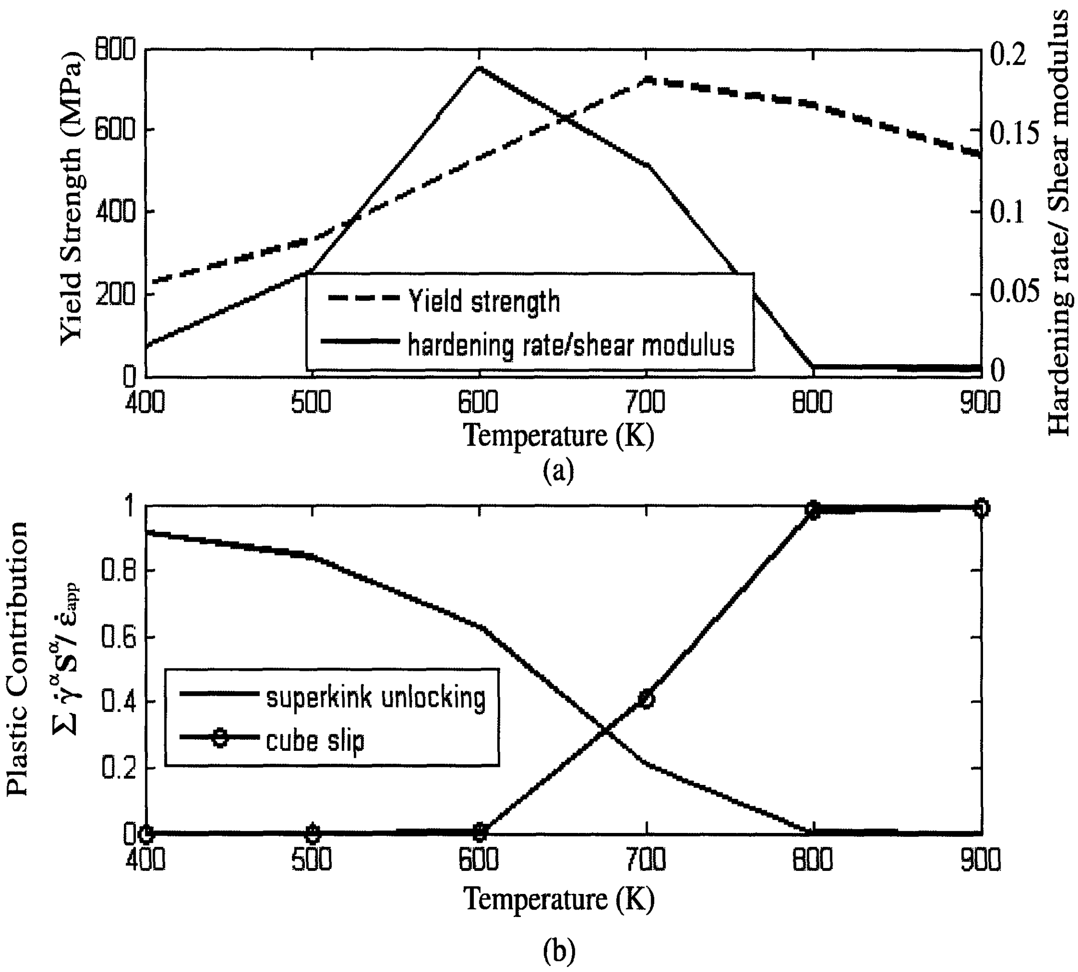

(a)

(b)

Figure 5-10: (a) Temperature-dependence of yield strength and the hardening rate for $[\bar{1}11]$ orientation; (b) Temperature-dependence of plastic strain-rate from different mechanisms for $[\bar{1}11]$ orientation, at $|\epsilon_p| = 0.2\%$;

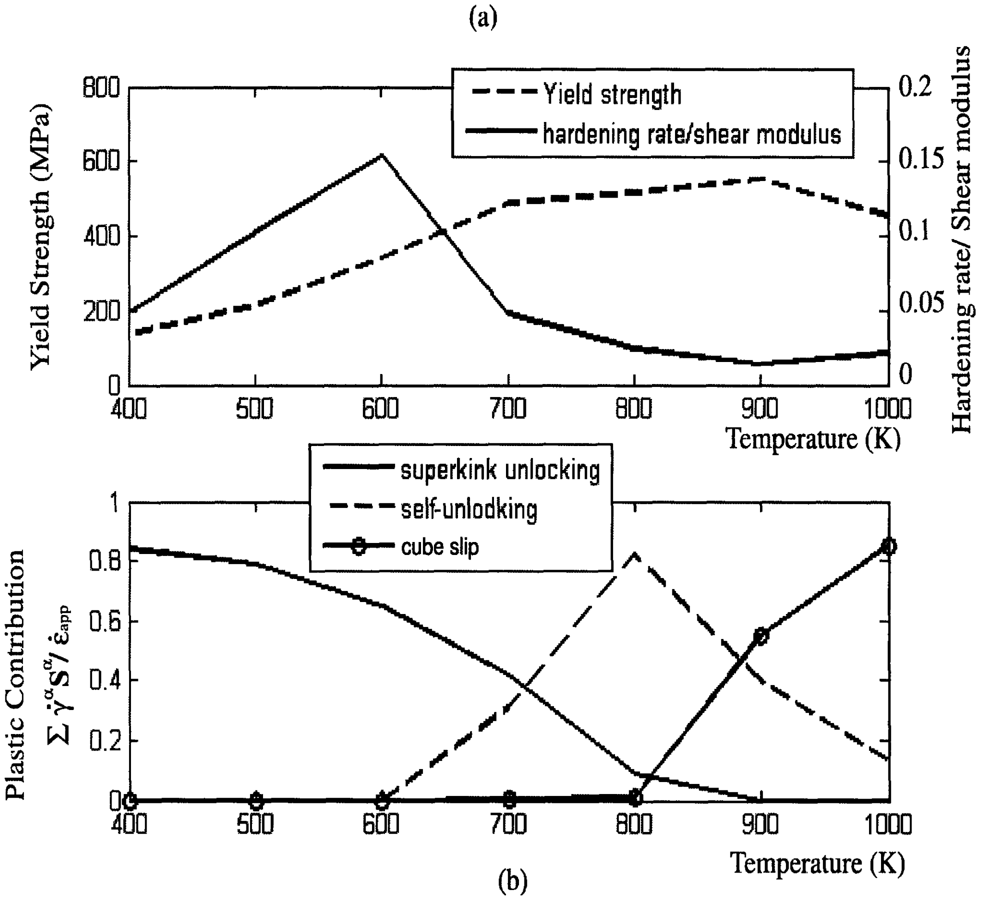

Figure 5-11: (a) Temperature-dependence of yield strength and the hardening rate for [123] orientation; (b) Temperature-dependence of plastic strain-rate from different mechanisms for [123] orientation, at $|\epsilon_p| = 0.2\%$;

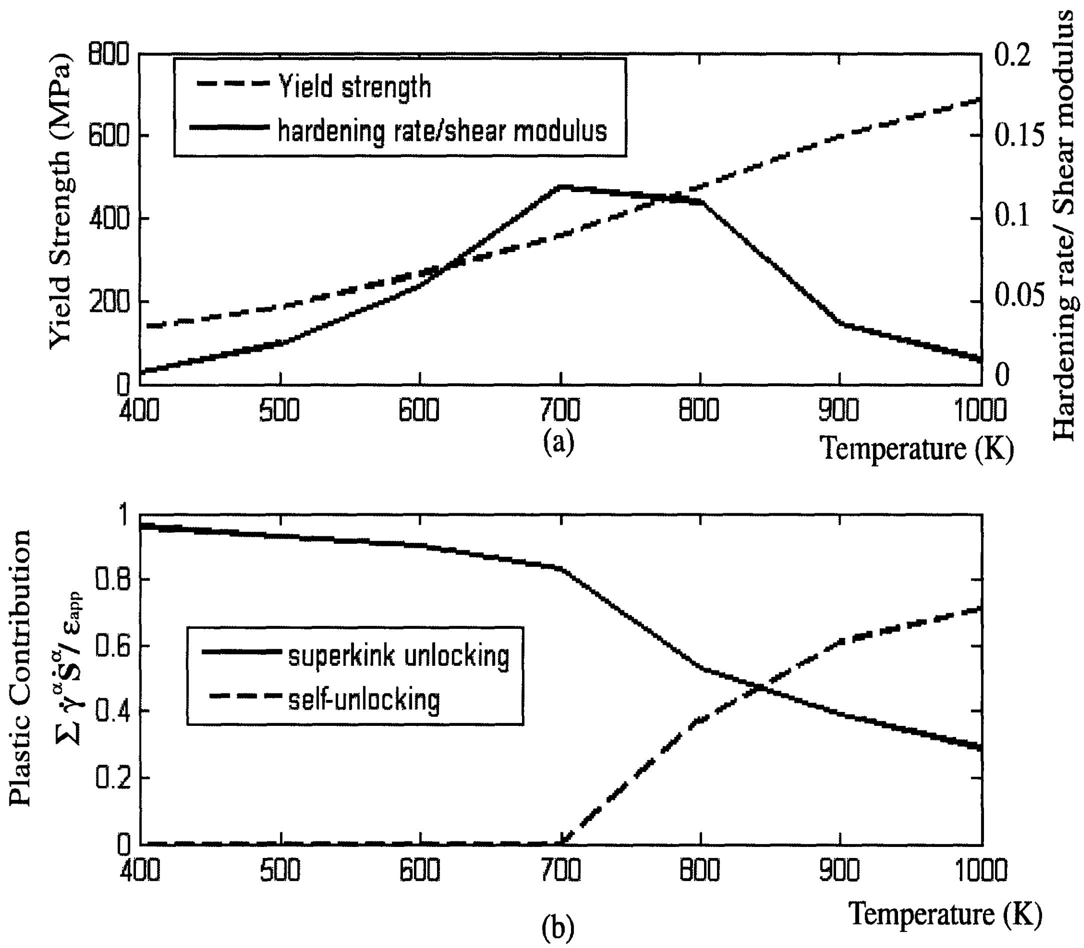

Figure 5-12: (a) Temperature-dependence of yield strength and the hardening rate for [001] orientation; (b) Temperature-dependence of plastic strain-rate from different mechanisms for [001] orientation, at $|\epsilon_p| = 0.2\%$;

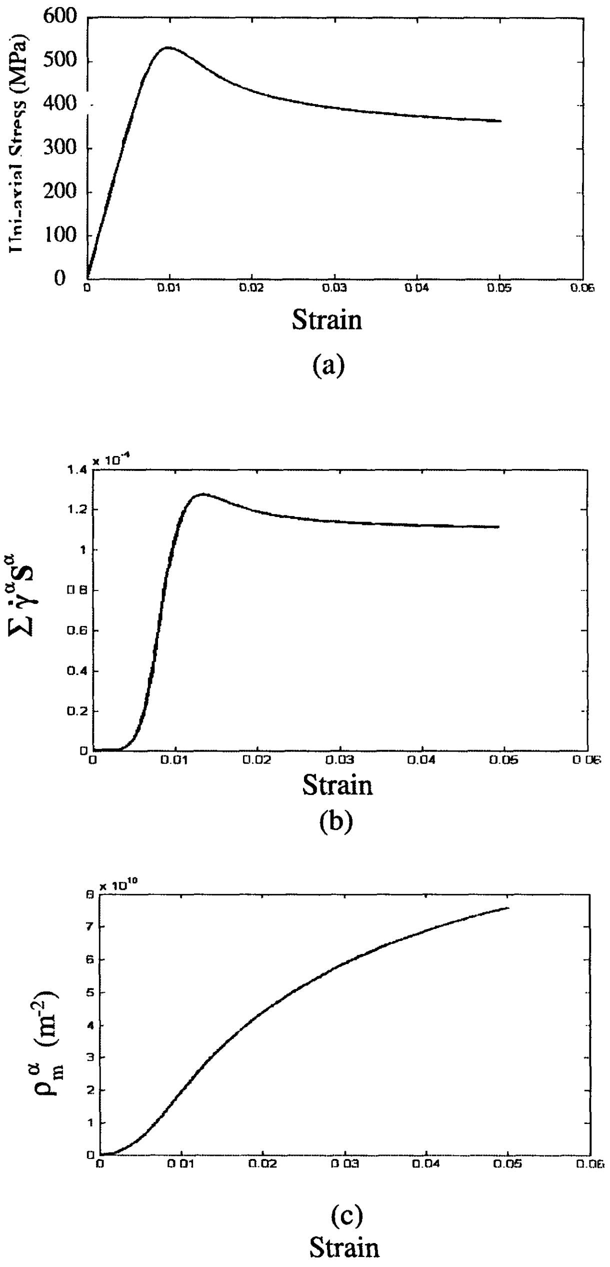

Figure 5-13: Simulation data from [001]-axial compression at 1100 K with an applied strain-rate of $1.1 \times 10^{-4} s^{-1}$. (a) Stress-strain curve; (b) Plastic strain-rate vs. strain; (c) Mobile dislocation density vs. strain.

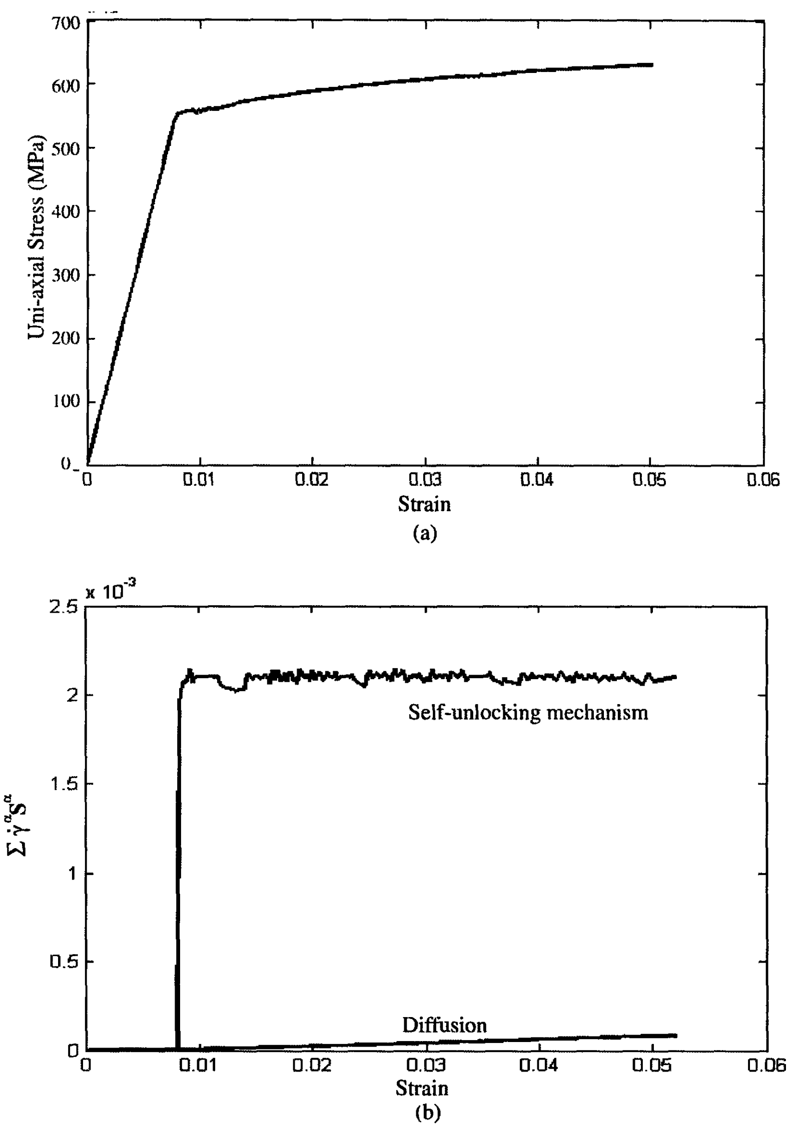

Figure 5-14: Simulation data of [001]-axial compression at 1100K with an applied strain-rate of $2.2 \times 10^{-3} s^{-1}$. (a) Stress-strain curve; (b) Plastic strain-rate for both self-unlocking mechanism and the diffusion mechanism vs. strain.

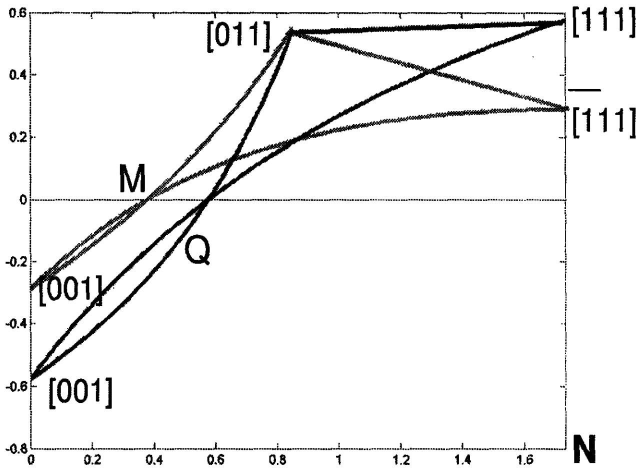

Figure 5-15: M, and Q drawn vs. N for the three boundaries of the crystal triangle to illustrate that the proposed model and the PPV model can give the similar prediction on the orientation-dependence of tension-compression asymmetry. $M = \frac{(\tau_{pe} - \kappa\tau_{se})}{\tau_{pb}}$ where $\kappa = 0.5$, $N = \frac{\tau_{cb}}{\tau_{pb}}$ and $Q = \frac{\tau_{pc}}{\tau_{pb}}$. In the PPV model, both non-Schmid stress components τ_{pe} and τ_{se} are considered in the cross-slip process , while in the proposed model, only τ_{pe} is considered. But M and Q are both negative for the [001] corner and positive for the [$\bar{1}$11]-[011] edge of the crystal triangle.

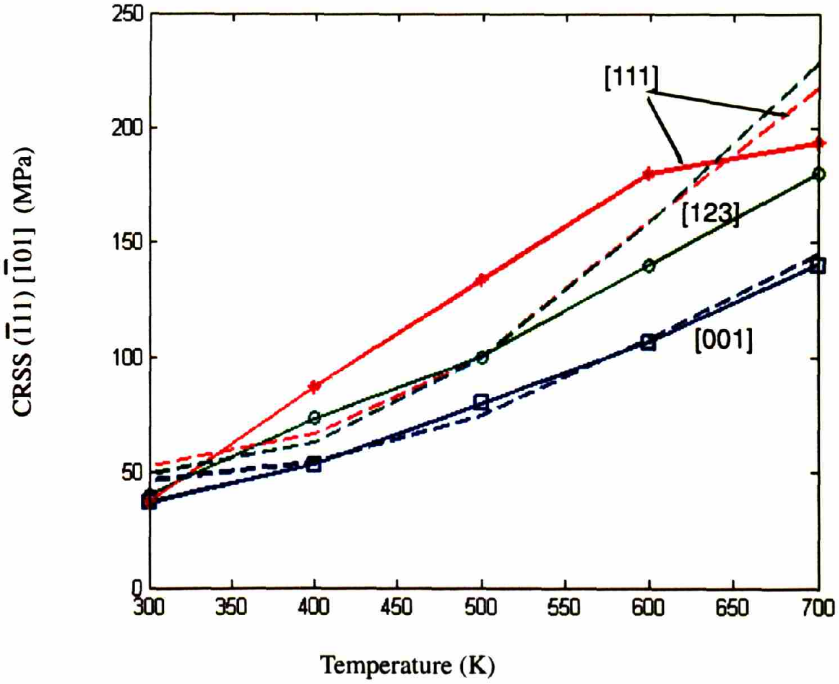

Figure 5-16: Illustration of the orientation-dependence of CRSS ($|\epsilon_p| = 0.2\%$): Simulated (dotted curves) and test data (solid curves) of CRSS for different temperatures in three orientations (red for [$\bar{1}$11], green for [123] and blue for [001]).

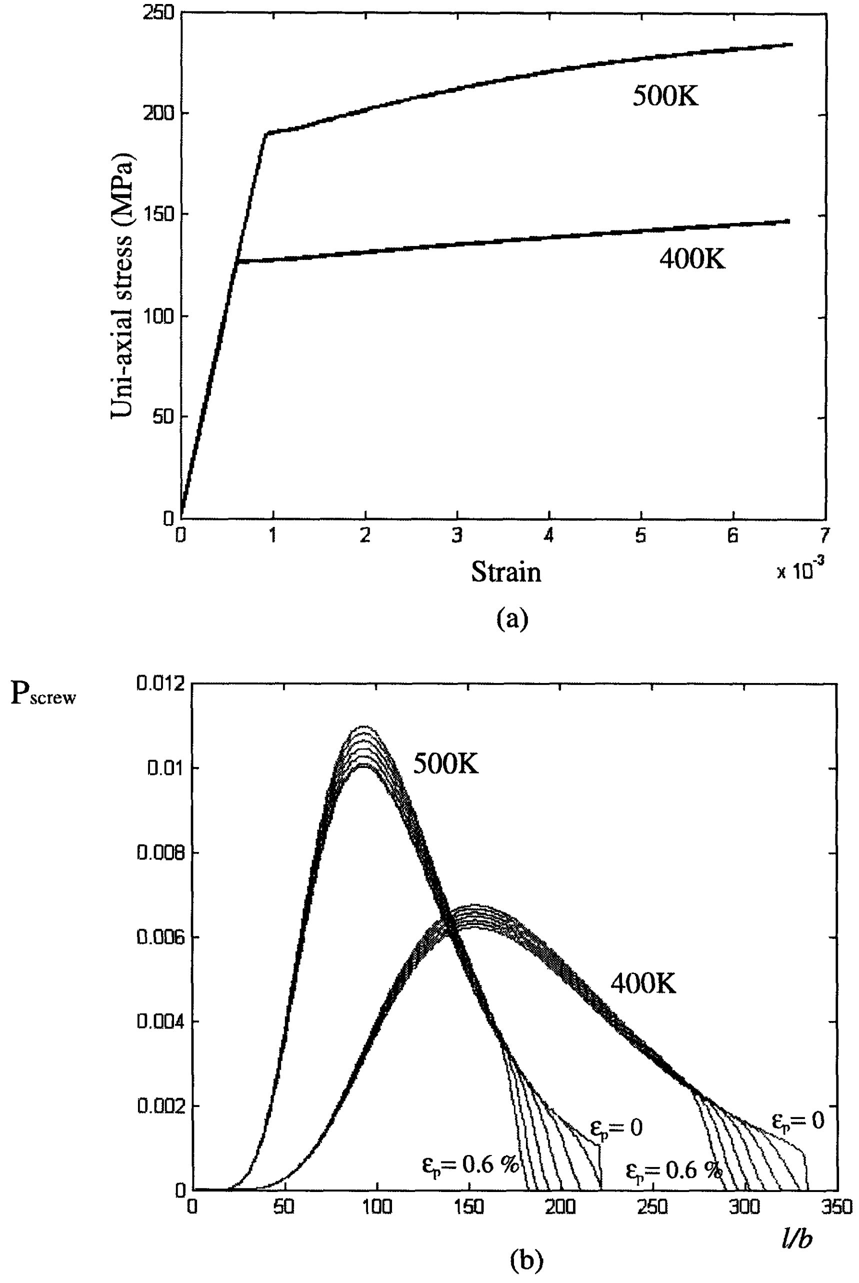

Figure 5-17: (a) Simulated stress-strain curves for [123]-axial compression at 400K and 500K; (b) evolution of the distribution of screw dislocations in the [123]-axial compression at both 400K and 500K: $P_{screw}(l)$ is plotted for different plastic strain offsets, from $|\epsilon_p| = 0$ to $|\epsilon_p| = 0.6\%$ with an increment of 0.1%.

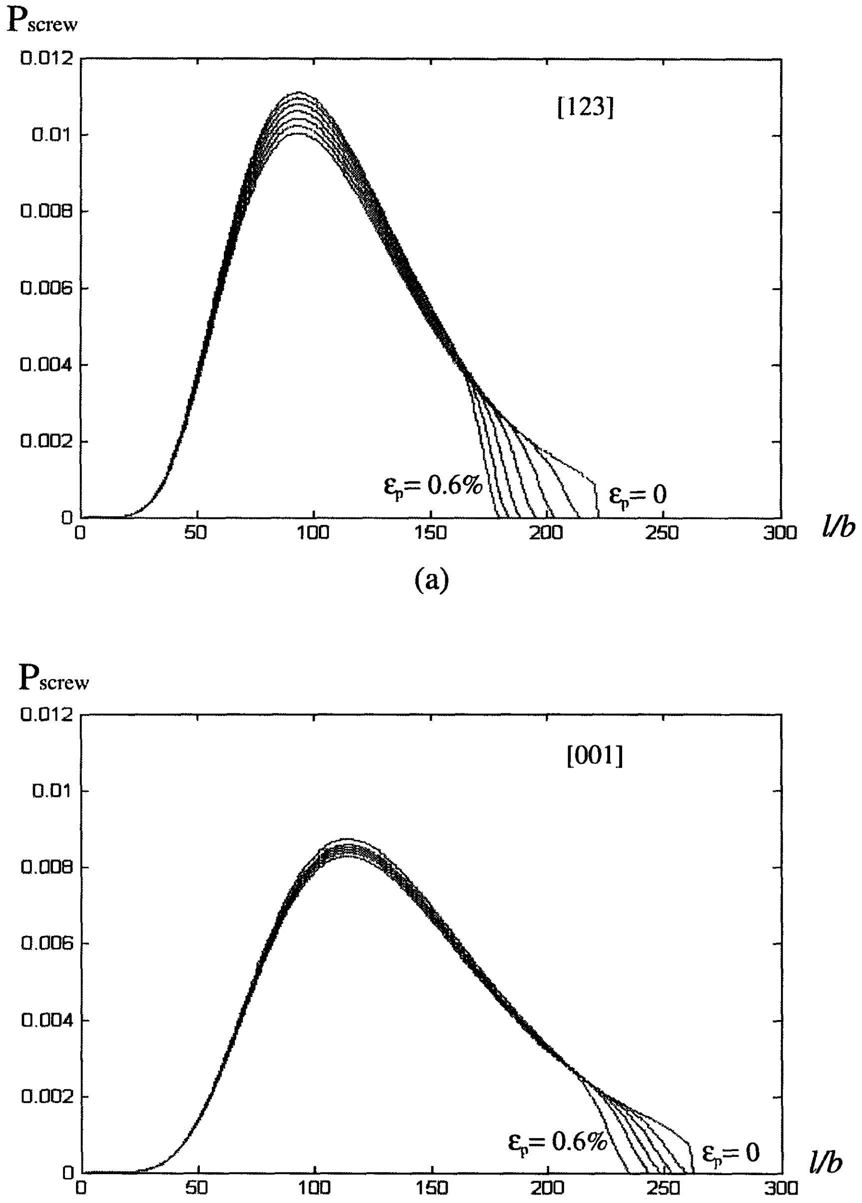

(a)

(b)

Figure 5-18: Evolution of the distribution of screw dislocations in compression at 400K. $P_{screw}(l)$ is plotted for different plastic strain offsets, from $|\epsilon_p| = 0$ to $|\epsilon_p| = 0.6\%$ with an increment of 0.1%. (a) [123]-axial compression; (b) [001]-axial compression.

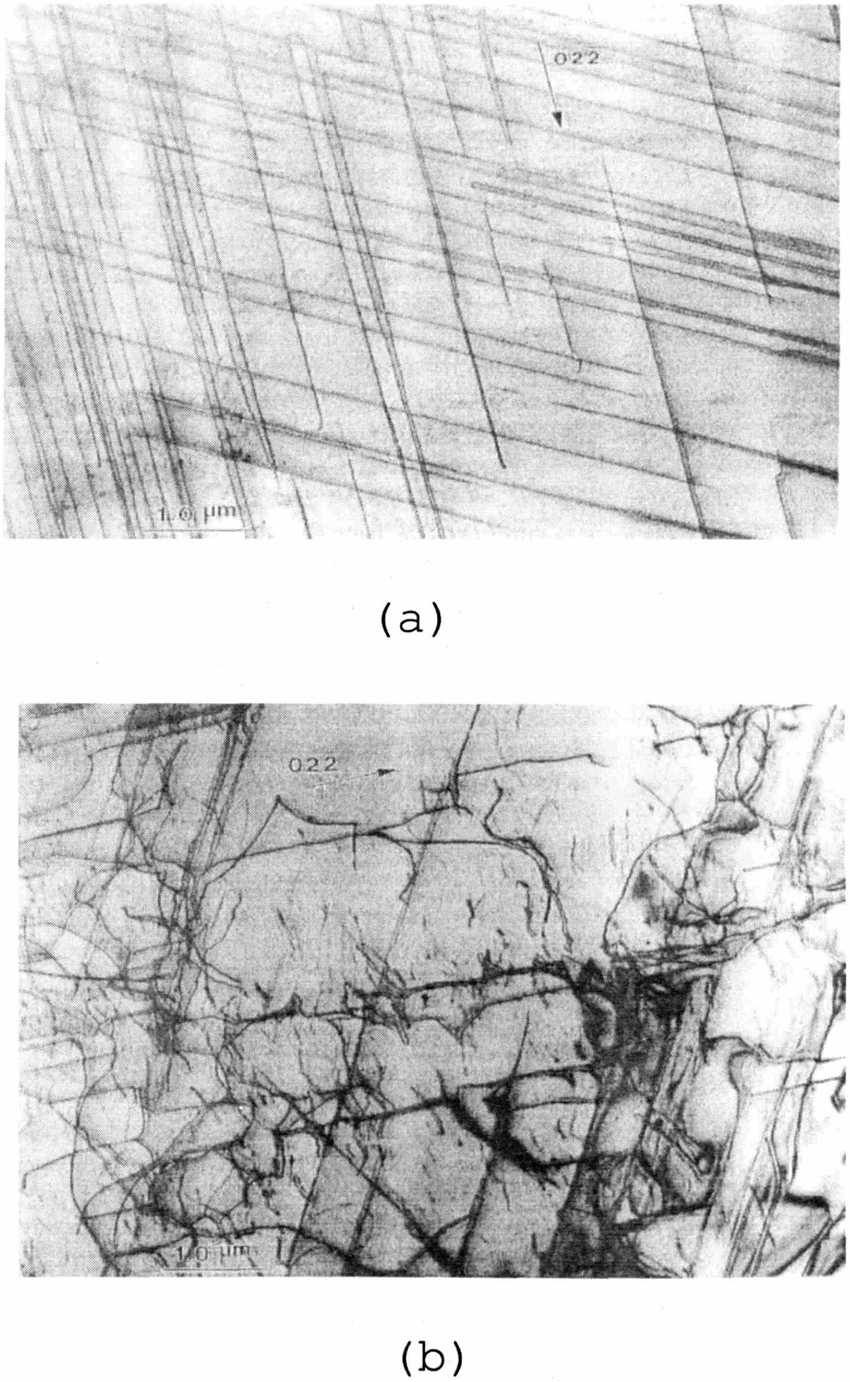

Figure 5-19: TEM observations of dislocation substructures in a high-temperature pre-strained sample after being subsequently deformed at RT. (a) typical high-temperature characteristic dislocation substructures; (b) mixture of both high-temperature and low-temperature characteristic dislocation substructures. [63]

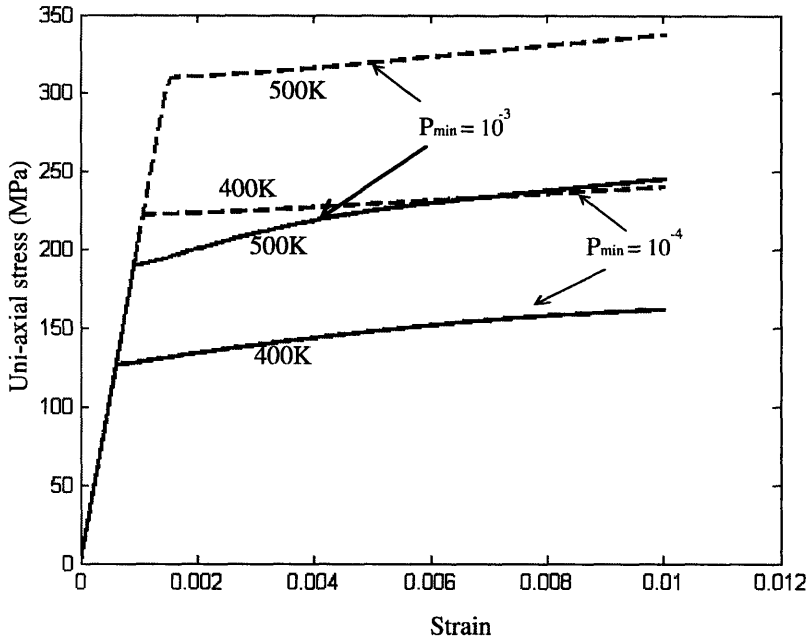

Figure 5-20: Parameter sensitivity study for different values of P_{min}: simulated stress-strain curves of [123]-compression. Dotted curves for $P_{min} = 10^{-3}$ and solid curves for $P_{min} = 10^{-4}$ and with all other parameters the same.

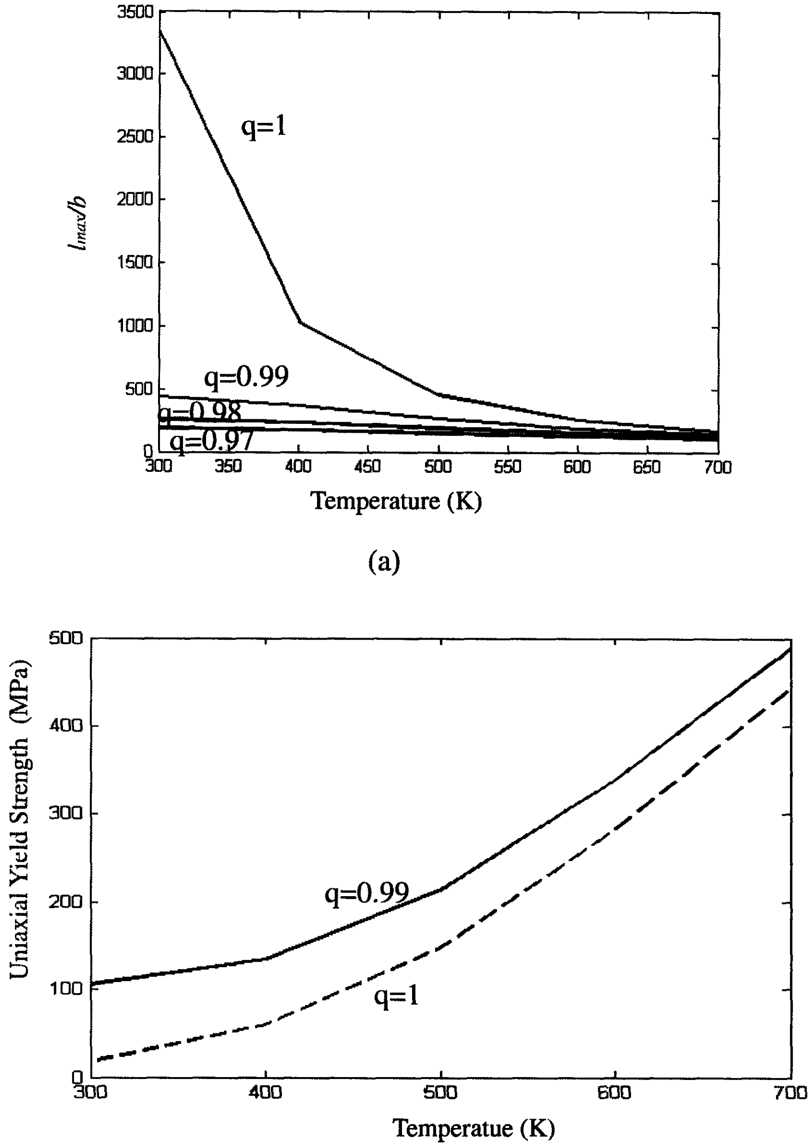

(a)

(b)

Figure 5-21: Parameter sensitivity study for different values of q (compression in [123] orientation, with S_{pe}=-0.1347): (a) l_{max} vs. temperature; (b) Uniaxial yield strength vs. temperature. Dotted curves for $q = 1$ and solid curves for $q = 0.99$ and with all other parameters the same.

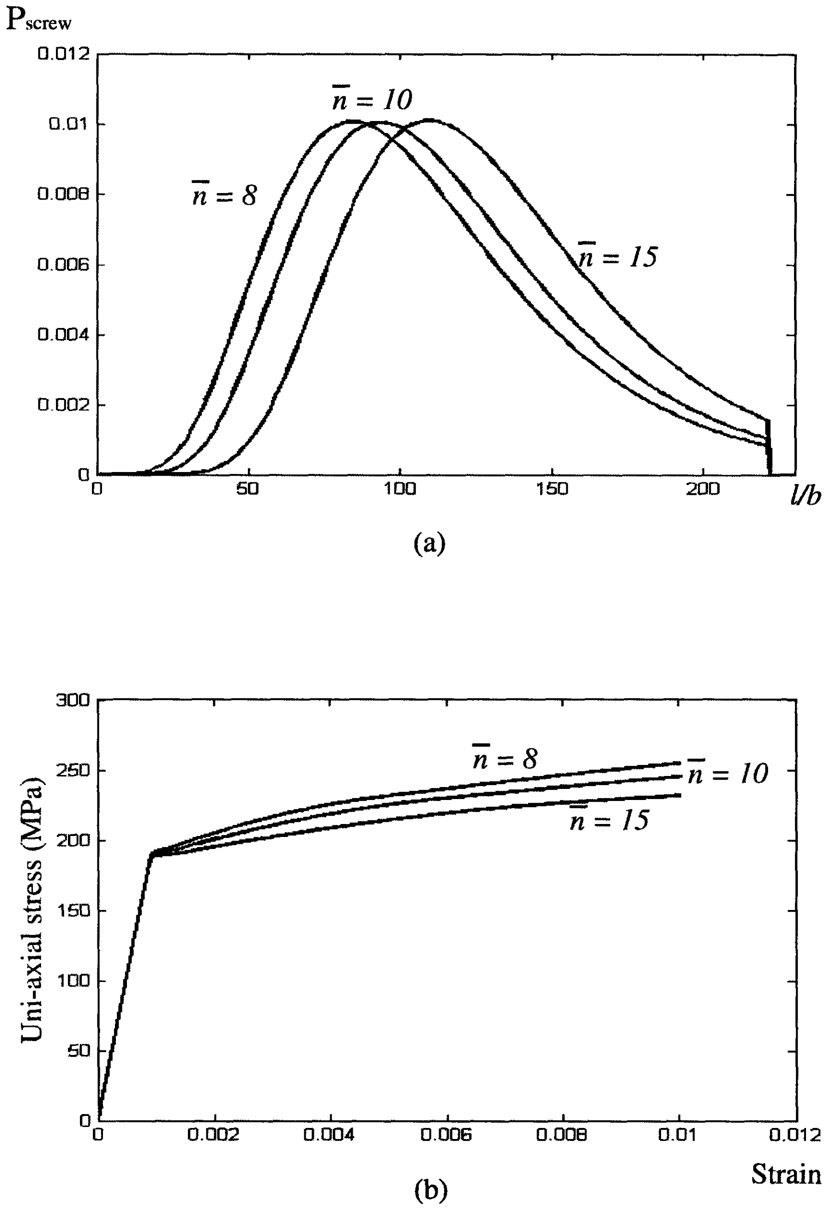

(a)

(b)

Figure 5-22: Parameter sensitivity study for different values of $\bar{n}$: (a) P_{screw} with different values of $\bar{n}$; (b) Stress-strain curves for [123]-compression at 500K with predicted with different value corresponding $\bar{n}$.

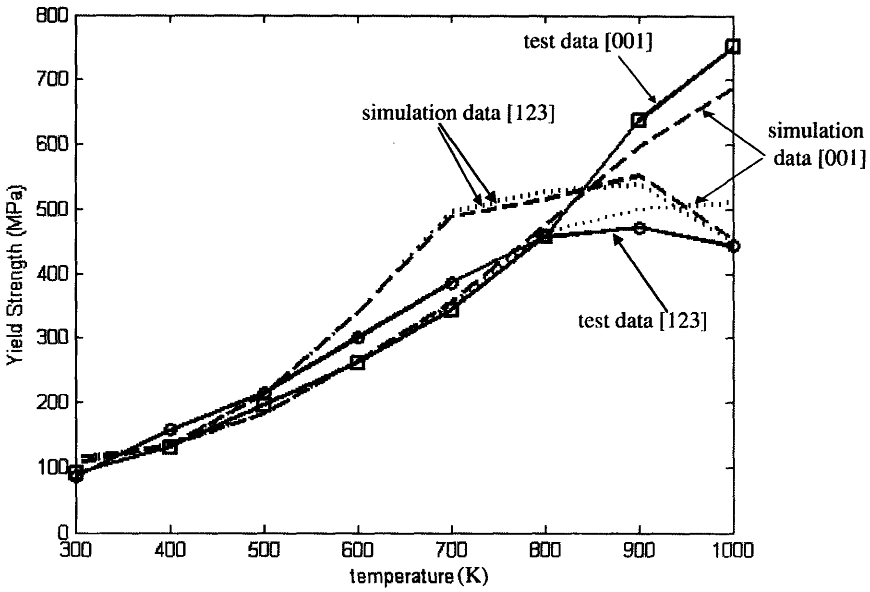

Figure 5-23: Parameter sensitivity study for different values of θ_{mean} and σ_θ: dotted lines are simulation results with $\theta_{mean} = 12° \times \exp(300/T)$ and $\sigma_\theta = 10°$; dashed lines are simulation results with $\theta_{mean} = (-0.1 \times T + 127)°$ and $\sigma_\theta = 3°$ (used in the current study); solid lines are experimental data [17].

Chapter 6

Conclusions and Future Work

A mechanism-based continuum crystal plasticity model was developed for $L1_2$ structure single crystals. Simulations were carried out, and the results were compared with the mechanical responses found in experimental observations.

The focus of this study was the yield and hardening behaviors in the anomalous yield-temperature dependence range (range I). The octahedral screws were found to be the dominant slip systems in this temperature region, and their movement was found to be non-planar with frequent cross-slips onto the cube planes. The cross-slip induced locking of screws and the subsequent unlocking procedure were generally considered as the origin of yield anomaly. Many micro-mechanisms were proposed based on certain observations and various assumptions for the dynamics (locking and unlocking) of screws, as reviewed in Chapter 2. The near rate-independence of yield strength and hardening rate has posed a dilemma to most of these existing models. Besides, the very complicated temperature-dependence and orientation dependence of the yield and hardening rates imply that it is difficult to describe this material with only a single mechanism.

In range I, development of the underlying mechanisms of the twelve $< 111 > [101]$ octahedral screw slip-systems was guided by the current understanding of the micro-mechanisms of the deformation behaviors in $L1_2$ structure single crystals. Both Hirsch's superkink-unlocking mechanism and Caillard's self-unlocking mechanism were adopted and modified. A superkink-based hardening mechanism was also developed and implemented. In range I, for the sake of small strain-rate-dependence of yield strength and hardening rate, the yield strength was mainly determined by the revised superkink model. Self-unlocking mechanism was activated in some orientations at the high-temperature part of range I, when the resolved shear stress has reached to a critical value.

The dynamics of the six $< 001 >$ [101] cube screw slipping systems were described by a standard power-law form. The cube-slip resistance linearly decreases with rising temperature, and the cube-slip gradually contributes to the plastic deformation. For most orientations, the transfer of yield-temperature dependence from abnormal (range I) to normal (range II) is due to the dominance of cube slips. For the [001] orientation with zero resolved cube shear stress, a diffusion mechanism was introduced to capture the normal temperature dependence of yield strength at very high temperatures.

The model proposed in this study has several advantages and certain limitations:

1. The current approach is a comprehensive constitutive modeling of $L1_2$ structure single crystal. Mechanical properties of both yielding and hardening were studied. The simulation results successfully captured the major mechanical properties associated with this material, including the temperature dependence of yield strength (including the [001] orientation) and hardening rate; orientation dependence of yield strength and hardening rate and the small strain-rate dependence of yield strength and hardening rate. The current approach did not give an explanation for the yield strength reversibility, but the proposed underlying mechanisms do not conflict with the observed phenomena.

2. The current approach was established based on micro-mechanisms representing current understanding of $L1_2$ structure single crystal. All of the mechanical properties captured by the simulation are based on certain physically-oriented mechanisms, rather than phenomenological adjustable parameters.

3. The formulation is relatively simple and the parameters are relatively few. The dominating parameters, such as the activation volume $V(l_{max})$ in the superkink unlocking part and the critical unlocking stress, $\tau_{critical}$. in the self-unlocking

part, were derived based on certain physical bases, and their magnitudes are consistent with experimental results.

4. Most of the current existing micro-mechanisms are not fully quantitatively established, and have not been verified by systematical simulations. The proposed quantitative approach and the numerical simulation help to understand and evaluate the existing models and mechanisms. For example, through this study, we find that due to the small value of Schmid factor on the octahedral planes, the self-unlocking mechanism is never activated for the $[\bar{1}11]$ orientation, which means the self-unlocking mechanism can not be used as a complete description.
5. The prediction of the yield strength is quite consistent with the experimental data, and the predicted hardening rate fairly captures the temperature and orientation dependence of the testing data. However, the predicted hardening rate is not very reasonable in the low-temperature part ($300K - 500K$) of range I. The hardening rate for $[\bar{1}11]$ and [011] is several times lower than the test data, due to the low consuming rate of the screws with longest superkinks for this temperature range. To maintain the same plastic strain rate, screws with longest superkinks are consumed much faster for single slip orientations, e.g. [123], than for those multi-slip orientations. This is why the prediction of hardening rate of [123] is relatively higher than the other two orientations.
6. The proposed continuum crystal plasticity model was developed within a framework of several internal state variables (e.g. P_{screw} and P_{θ}), for finite plastic deformations. The initial states and the evolutions of these internal variables are defined based on certain assumptions and adjustable parameters, which need further verification.

Obviously, there remains an abundance of work to be done in this area, on varying levels of complexity and with the further development in discovering the underlying mechanisms. For a better and broader approach, some further modifications may be considered:

1. Atomic simulations is a promising approach in the study of the structure, energetics, cross-slip, and self-unlocking of screw dislocations, providing valuable information in understanding the underlying mechanisms for the macro-mechanical properties.

2. The hardening mechanism with internal variables needs further improvement to get better predictions in strain hardening-rate (temperature and orientation dependence); critical experimental documentation of the evolution of internal state variables (superkink distribution) needs to be carried out to evaluate the proposed hardening mechanism. For multi-slip orientations, interactions of each active system should be taken into consideration.

3. Since the $L1_2$ structure compounds are usually very composition-dependent, study in the ternary alloy effects (how does the ternary alloy affect the structure, the fault energies, cross-slip and the dynamics of the screw dislocations) is necessary.

4. Mechanisms of dislocation substructure local recovery should be developed in order to capture the properties of yield strength reversibility presented in the Cottrell-Stokes experiments.

5. Study of mechanical properties of $L1_2$ poly-crystals can be carried out by implementing this single crystal plasticity model into poly-crystal geometry.

Appendix A

Summary of the Model

The constitutive model developed in this study and described in Chapter 3-4 can be summarized by the following equations:

$$\bar{\mathbf{T}} = \mathcal{L}[\mathbf{E}^e] \tag{A.1}$$

$$\mathbf{E}^e \equiv \frac{1}{2}\left\{\mathbf{F}^{eT}\mathbf{F}^e - \mathbf{I}_2\right\} \tag{A.2}$$

$$\mathbf{F}^e = \mathbf{F}\mathbf{F}^{p-1} \tag{A.3}$$

$$\dot{\mathbf{F}}^p = \mathbf{L}^p\mathbf{F}^p \tag{A.4}$$

$$\mathbf{L}^p = \sum_{\alpha} \dot{\gamma}^\alpha \mathbf{m}_0^\alpha \otimes \mathbf{n}_0^\alpha \qquad \alpha = 1 \sim 18 \tag{A.5}$$

$$\dot{\gamma}^\alpha = \begin{cases} \dot{\gamma}_1^\alpha + \dot{\gamma}_2^\alpha & \text{octahedral slip } \alpha = 1 \sim 12 \text{ ;} \quad (a) \\ \dot{\gamma}_o(\frac{\tau^\alpha}{S_1(T)})^{m_1} & \text{cube slip } \alpha = 13 \sim 18 \qquad (b) \end{cases} \tag{A.6}$$

where

$$S_1(T) = (1000 - 0.75T(\mathrm{K}))\, MPa. \tag{A.7}$$

For the octahedral slips, the contribution from the superkink unlocking mechanism ($\dot{\gamma}_1^\alpha$) is given as:

$$\dot{\gamma}_1^\alpha = \rho_{total}^\alpha b \sum_{b}^{l_{max}^\alpha} P_{screw}^\alpha(l) v^\alpha(l, \tau^\alpha), \tag{A.8}$$

where

$$P_{screw}(l) = \exp\left(\frac{1}{2}[\ln W(l)\sigma_n]^2\right)[lnW(l)\sigma_n^2 + \bar{n}]P(l)W(l)^{(\bar{n}-1)}, \tag{A.9}$$

and

$$v^\alpha(l, \tau^\alpha) = v_0^{SK} \exp\left(-\frac{H_u(l, \tau^\alpha)}{kT}\right), \tag{A.10}$$

in which the unlocking activation enthalpy is given by Hirsch [23] as:

$$H_u = H_{u0}^* - V(l)\tau^\alpha, \qquad \text{and } V(l) = 3.5\frac{l}{b}b^3, \tag{A.11}$$

where the magnitude of activation volume ($3.5\frac{l}{b}b^3$) was estimated by Hirsch according to the relation of stress and the superkink configuration shown in Figure 2-6(a).

The contribution from self-unlocking mechanism ($\dot{\gamma}_2^\alpha$) is given as:

$$\dot{\gamma}_2^\alpha = \rho_{total}^\alpha b \int_0^{\theta_{max}} P_\theta(\theta) v_2(\theta, \tau^\alpha) d\theta. \tag{A.12}$$

P_θ is the normalized Gaussian distribution:

$$P_\theta(\theta) = \frac{1}{\sqrt{2\pi\sigma_\theta^2}} \frac{\exp\left(\frac{-(\theta-\bar{\theta})^2}{2\sigma_\theta^2}\right)}{(N(55^\circ) - N(0^\circ))}, \tag{A.13}$$

where

$$N(\theta) = 1/2\left[1 + erf\left(\frac{\theta - \bar{\theta}}{\sigma_\theta\sqrt{2}}\right)\right], \tag{A.14}$$

$\sigma_\theta = 3^\circ$, and $\bar{\theta}$ is assumed to be a linear function of temperature:

$$\bar{\theta} = (-0.1 \times T(\mathrm{K}) + 127)^\circ \qquad \bar{\theta}_{max} = 55^\circ, \tag{A.15}$$

$$v_2 = \begin{cases} v_0^{SU}(\frac{\tau^\alpha(\theta,\gamma_o,\gamma_c)}{S_2(T)})^{m_1} & \text{if } \tau \geq \tau_{critical}; \\ 0 & \text{otherwise.} \end{cases} \tag{A.16}$$

Here

$$\tau_{critical}(\theta) = \frac{\gamma_o}{b} - \frac{\gamma_c}{b} g(\theta), \tag{A.17}$$

and

$$S_2(T) = (370 - 0.1T(\mathrm{K}))\,. \tag{A.18}$$

The diffusion mechanism for the [001] orientation at high temperatures is described as:

$$\dot{\gamma}_d^\alpha = \rho_m b v_0^d \left(\frac{\tau^\alpha}{S_d}\right)^{m_2} \exp\left(-\frac{H_d}{kT}\right), \tag{A.19}$$

where

$$\dot{\rho}_m^\alpha = \rho_{total}^\alpha (\frac{\tau^\alpha}{S_d})^2 f_2 \exp\left(-\frac{H_d}{kT}\right) \tag{A.20}$$

$$\dot{\rho}_{total}^\alpha = -C_\rho \rho_m^\alpha \rho_{total}^\alpha R v^\alpha. \tag{A.21}$$

Bibliography

[1] Kear B. H. and Wilsdorf G. F. (1962), *Trans. TMS-AIME* , Vol. 224, p. 382.

[2] Westbrook J.H. (1957), *Trans. AIME*, Vol. 209, p. 898.

[3] Flinn P. A. (1960), *Trans. AIME*, Vol. 218, p. 145.

[4] Umakoshi Y., Pope D. P. and Vitek V. (1984), *Acta Metall.*, Vol. 32, p. 449.

[5] Thornton P. H., Davies R.G. and Johnston T. L. (1970), *Metall. Trans. A*, Vol. 1, p. 207.

[6] Dowling W. E. and Gibala R., (1989), *MRS Symp. Proc.*, Vol. 133, p. 209.

[7] Kear B. H. and Hornbecher M. F. (1966), *Trans. ASM*, Vol. 59, p. 155.

[8] Staton-Bevan A. E. and Rawlings R. D. (1975), *Phil. Mag.*, Vol. 32, p. 787.

[9] Nemoto M., Echigoya J. and Suto H. (1977), *Japan Soc. of Electron Microscopy*, p. 467.

[10] Lours P., Coujou A. and Coulomb P. (1991), *Acta Metall.*, Vol. 39, No. 8, p. 1787.

[11] Couret A., Sun Y. Q. and Hirsch P. B. (1992), *Phil. Mag. A*, Vol. 67, No. 1, p. 29.

[12] Molenat G. and Caillard D. (1991), *Phil. Mag. A* Vol. 64, No. 6, p. 1291.

[13] Sun Y.Q. (1995), *MRS Bull.*, Vol. 20, No. 7, p. 29.

[14] Chrzan D. C. and Mills M. J. (1996), *Dislocations in Solids*, Vol.10, Eds. F. R. N. Nabarro and M. S. Duesbery, Elsevier Science B. V., Amsterdam, p. 190.

[15] Ezz S. S., Pope D. P. and Paidar V. (1982), *Acta Metall.*, Vol. 30, p. 921.

[16] Ezz S. S. and Hirsch P. B. (1995), High-Temperature Ordered Intermetallic Alloys, *MRS Symp. Proc.*, Vol. 364, p. 35.

[17] Bontemps-Neveu C. (1991), PhD. Thesis, Univ. of Paris-Sud, France, cited in [34].

[18] Seiji M, Shouichi O. and Yoshihiro O. (1989), *Mat. Soc. Symp. Proc.*, Vol. 133, p. 341.

[19] Shi X. (1995), PhD. Thesis, Univ. de. Paris-Nord, France, cited in [34].

[20] Lall C., Chin S. and Pope D. P. (1979), *Metall. Trans. A*, Vol. 10, p. 1323.

[21] Rentenberger C. and Karnthaler H. P. (2001), *Mat. Sci. Eng.*, Vol. A319-321, p. 347.

[22] Sun Y. Q., Hazzledine P. M.,Crimp M. A. and Couret A. (1991), *Phil. Mag. A.*, Vol. 64, p. 327.

[23] Hirsch P. B. (1992), *Phil. Mag. A*, Vol. 65, No. 3, p. 569.

[24] Takeuchi S. and Kuramoto E. (1973), *Acta Metall.*, Vol. 21, p. 415.

[25] Paidar B., Pope D. P. and Vitek V. (1984), *Acta Metall. Mater*, Vol. 32, No. 3, p. 435.

[26] Friedel J. (1957) , *Dislocations and Mechanical Properties of Crystals*, Wiley, New York, p. 330.

[27] Bonneville J. and Escaig B. (1979), *Acta Mater.*, Vol. 27, p. 1477.

[28] Ezz S. S., Pope D. P. and Paidar V. (1982), *Acta Metall.*, Vol. 30, p. 921.

[29] Schoeck G. (1993), *Phil. Mag. Lett.*, Vol. 67, No. 3, p. 193.

[30] Schoeck G. (1994), *Phil. Mag. Lett.*, Vol. 70, No. 4, p. 179.

[31] Parthasarathy T. and Dimiduk D. (1996), *Acta. Mater.*, Vol. 44, No. 6, p. 2237.

[32] Korner A. (1992) *Phil. Mag. Lett.*, Vol. 66, No. 3, p. 141.

[33] Masahiko D. and Toshiyuki H. (2000), *Intermetallics* Vol. 8, p. 1005.

[34] Veysiere P. and Saada G. (1996), *Dislocations in Solids*, Vol. 10, Eds. F. R. N. Nabarro and M. S. Duesbery, Elsevier Science B. V., Amsterdam, p.253.

[35] Sun Y. Q. and Hazzledine P. M. (1988), *Phil. Mag. A.*, Vol. 58, p. 603.

[36] Sun Y. Q. (1997), *Acta Metall.*, Vol. 45, No.9 , p. 3527.

[37] Louchet F. (1995), *Journal de Physique III*, Vol. 5, p. 1803.

[38] Dimiduk D. M. (1989), PhD. Thesis, Carnegie-Mellon Univ.

[39] Hirsch P. B. (1996), *Phil. Mag. A*, Vol. 74, No. 4, p. 1019.

[40] Hirsch P. B. (2003), *Phil. Mag.* , Vol. 83, No. 8, p. 1007.

[41] Chiu Y. L. and Veyssiere P. (2003), *Phil. Mag. A*, Vol. 83, p. 179.

[42] Caillard D. and Paidar V. (1996), *Acta mater.*, Vol. 44, No. 7, p. 2759.

[43] Mills M.J. and Chrzan D.C. (1992), *Acta Metall. Mater.*, Vol. 40, No. 11, p. 3051.

[44] Devincre B., Veyssiere P., Kubin L.P. and Saada G. (1997), *Phil. Mag. A*, Vol. 75, No. 5, p. 1263.

[45] Devincre B., Veyssiere P., and Saada G. (1999), *Phil. Mag. A*, Vol. 79, No. 7, p. 1609.

[46] Cuitiño A. M. and Ortiz M. (1993), *Mater. Sci. Eng.*, Vol. 170, p. 111.

[47] Kruml T., Conforto E., Lo Piccolo B., Caillard D., and Martin J. L. (2002), *Acta mater.*, Vol. 50, p. 5091.

[48] Viguier B., Martin J. L. and Bonneville J. (2002), *Dislocations in Solids*, Vol. 11, Ed. F. R. N. Nabarro, North-Holland, p. 459.

[49] Hazzkedube P.M., Yoo M.H., Sun Y. Q. (1989), *Acta Mater.*, Vol. 37, No. 12, p1477.

[50] Chrzan D. C., Uchic M. D. and Xin W. D. (1999), *Phil. Mag. A*, Vol. 79, No. 10, p. 2397.

[51] Caillard D. (1996), *Acta mater.*, Vol. 44, No. 7, p. 2773.

[52] Molenat G. and Caillard D. (1991), *Phil. Mag. A* Vol. 69, No. 5, p. 939.

[53] Yoo M. H. (1986), *Scripta Metall. Mater.*, Vol. 20, p. 915.

[54] Saada G. and Veyssiere P. (1992), *Phil. Mag. A* Vol. 66, p. 1183.

[55] Rentenberger C. and Karhthaler H.P. (1995), *Mat. Res. Soc. Symp. Proc.*, Vol. 364, p. 689.

[56] Johnston W. G. (1962), *J. app. Phys.*, vol. 33, No. 9, p. 2716.

[57] Kalidindi S. R, Bronkhorst C. A. and Anand L. (1992), *J. Mech. Phys. Solids*, Vol. 40, p. 537.

[58] Tanaka K. and Koiwa M. (1996), *Intermetallics*, Vol. 4, p 29.

[59] Danielsson M., Parks D. M., Boyce M. C. (2002), *J. Mech Phys. Solids*, Vol. 50, No. 2, p. 351.

[60] Kruml T., Paidar V. and Martin J.L. (2000), *Intermetallics*, Vol. 8, p. 729.

[61] Yoo M. H. and Liu C. T. (1988), *J. Mater. Res.*, Vol. 3, p. 845.

[62] Hemker K. J. (1991) , Ph.D thesis, Stanford Univ., cited in [34].

[63] Dimiduk D. M. (1995), *Phil. Mag. Lett.*, Vol. 71, No. 1, p. 21.

[64] Greenberg B. A. and Ivanov M. A. (1997), *Mat. Sci. Eng.*, Vol. A239-240, p. 813.

[65] Sun Y. Q. and Hazzledine P.M.(1996), *Dislocations in Solids*, Vol.10, Eds. F. R. N. Nabarro and M. S. Duesbery, Elsevier Science B. V., Amsterdam, p. 27.

[66] Caillard D. and Martin J. L. (2003), *Thermally activated mechanisms in crystal plasticity*, Elsevier Science Ltd.

[67] Qin Q. and Bassani J.L. (1994), *J. Mech. Phys. Solids.*, Vol. 40, p. 813.

[68] Yuan Y. (2003), M. Sc. thesis, Dept. of Mechanical Eng., MIT.